Master Thesis

Czech
Technical
University
in Prague

F3

Faculty of Electrical Engineering
Department of Cybernetics

# Partial Volume Effect Correction in Positron Emission Tomography Images for Hypometabolism Detection

# Korekce efektu částečného objemu v obrazech pozitronové emisní tomografie k detekci hypometabolismu

**Bc. Kateřina Macková**

Supervisor: Ing. Radek Janča, Ph.D.
Study program: Medical Electronics and Bioinformatics
Specialisation: Image Processing
May 2023

# MASTER‘S THESIS ASSIGNMENT

## I. Personal and study details

Student's name: **Macková Kateřina** Personal ID number: **476370**

Faculty / Institute: **Faculty of Electrical Engineering**

Department / Institute: **Department of Cybernetics**

Study program: **Medical Electronics and Bioinformatics**

Specialisation: **Image processing**

## II. Master’s thesis details

Master’s thesis title in English:

**Partial Volume Effect Correction in Positron Emission Tomography Images for Hypometabolism Detection**

Master’s thesis title in Czech:

**Korekce efektu částečného objemu v obrazech pozitronové emisní tomografie k detekci hypometabolismu**

Guidelines:

Positron emission tomography (PET), together with magnetic resonance imaging (MRI), are important neuroimaging methods in the diagnosis of refractory focal epilepsy. The epileptogenic tissue is characterized by decreased metabolic activity (hypometabolism). In previous work, a method for the automatic detection of hypometabolism was proposed. PET images suffer from a low effective resolution (FWHM), which can be increased by 'partial volume correction' (PVC). The true FWHM of a scanner varies for a particular scanning protocol, which is often challenging to identify retrospectively.
1) Review factors that adversely affect FWHM of PET (scanner technology, protocol, patient movements).
2) If possible, measure the referential FWHM of PET scanners, or use parameters provided by producers.
3) Create an FWHM estimator based on a presumption of FDG-radiotracer distribution in the cortex segmented from MRI. Compare FWHM estimation with a reference value.
4) Quantify patient movements during acquisition in PET dynamic sequence and effect on FWHM in the final reconstruction.
5) Asses effect of FWHM to Müller-Gärtner partial volume effect correction method (PETPVE12, PETPVC) and hypometabolism detection.

Bibliography / sources:

[1] Gonzalez-Escamilla G, et al. 'PETPVE12: an SPM toolbox for partial volume effects correction in brain PET–application to amyloid imaging with AV45-PET.' Neuroimage 147 (2017): 669-677.
[2] Thomas BA., et al. 'PETPVC: a toolbox for performing partial volume correction techniques in positron emission tomography.' Physics in Medicine & Biology 61.22 (2016): 7975.
[3] Ruttimann UE, et al. 'Head motion during positron emission tomography: Is it significant?.' Psychiatry Research: Neuroimaging 61.1 (1995): 43-51.
[4] Sari H, et al. 'Estimation of an image derived input function with MR-defined carotid arteries in FDG-PET human studies using a novel partial volume correction method.' Journal of Cerebral Blood Flow & Metabolism 37.4 (2017): 1398-1409.

Name and workplace of master’s thesis supervisor:

**Ing. Radek Janča, Ph.D. Department of Circuit Theory FEE**

Name and workplace of second master’s thesis supervisor or consultant:

Date of master’s thesis assignment: **27.01.2023** Deadline for master's thesis submission: **26.05.2023**

Assignment valid until: **22.09.2024**

| | | |
|---|---|---|
| Ing. Radek Janča, Ph.D.<br>Supervisor’s signature | prof. Ing. Tomáš Svoboda, Ph.D.<br>Head of department’s signature | prof. Mgr. Petr Páta, Ph.D.<br>Dean’s signature |

## III. Assignment receipt

The student acknowledges that the master's thesis is an individual work. The student must produce her thesis without the assistance of others, with the exception of provided consultations. Within the master's thesis, the author must state the names of consultants and include a list of references.

.

Date of assignment receipt

Student's signature

# Acknowledgements

I am grateful to Ing. Jiří Terš and doc. MUDr. Otakar Bělohlávek, CSc. for organizing and carrying out the reference measurements in the PET Center of the Na Homolce Hospital and for many valuable advises. I am also grateful to the teams from Department of Neurology and Department of Pediatric Neurology of the Motol University Hospital for providing me the data of patients with epilepsy. I would also like to thank to my supervisor, Ing. Radek Janča, Ph.D., and to Ing. Petr Ježdík, Ph.D. for their support and guidance throughout my master's thesis. I am thankful to my family and friends for their support during the whole work.

# Declaration

I declare that the presented work was developed independently and that I have listed all sources of information used within it in accordance with the methodical instructions for observing the ethical principles in the preparation of university thesis.

On 26. May 2023 in Prague

# Abstract

The quality of fluorodeoxyglucose positron emission tomography (FDG-PET) images for diagnostics and presurgical evaluation of epilepsy is limited mainly by their low effective resolution which can be further affected by patient movement during acquisition. Partial volume correction (PVC) can additionally increase the effective resolution of the image. A method for automatic detection of hypometabolism in PVC FDG-PET images was proposed in a previous work. Detection results can be influenced by the full width at half maximum (FWHM) of the scanner point spread function that was used as input for the PVC. However, the FWHM can be often unknown in clinical practice.

FDG-PET images of 63 patients who were candidates for surgical treatment of epilepsy in Motol University Hospital were analyzed. A method for automatic estimation of FWHM was proposed that is based on estimating the parameters of edge spread function. The method was validated with reference measurement on the capillary phantom. The influence of patient movement on estimated FWHM was investigated. The effect of input FWHM on the hypometabolism detection performance was evaluated.

The automatic FWHM estimation generally performed as expected and returned reasonable values of FWHM. The estimated FWHM was only slightly affected by patient movements. The detection performance was not critically dependent on the precise FWHM used for PVC.

Automatically estimated FWHM or FWHM specified by the manufacturer are a good choice for PVC and automatic hypometabolism detection in clinical practice. These results will allow to focus on the further development of the hypometabolism detection method.

**Keywords:** FDG-PET, hypometabolism, partial volume correction, epilepsy, effective resolution

# Abstrakt

Kvalita obrazů pozitronové emisní tomografie fluordeoxy-glukózy (FDG-PET) pro diagnostiku a chirurgickou léčbu epilepsie je limitována zejména jejich nízkým efektivním rozlišením, které může být dále zhoršeno pohybem pacienta při snímání obrazu. Efektivní rozlišení může být zvýšeno korekcí efektu částečného objemu (PVC). V předchozí práci byla navržena metoda automatické detekce hypometabolismu v obrazech FDG-PET zpracovaných PVC. Šířka rozptylové funkce PET skeneru v polovině jejího maxima (FWHM), která byla použita pro PVC, může ovlivnit výsledky detekce. FWHM ale může být v klinické praxi často neznámá.

Analyzovány byly obrazy FDG-PET mozku 63 pacientů, kteří byli kandidáti na chirurgickou léčbu epilepsie ve FN Motol. Navržena byla metoda automatického odhadu FWHM, která je založena na odhadu parametrů rozptylové funkce hrany. Metoda byla validována referenčním měřením FWHM na kapilárním fantomu. Byl vyhodnocen vliv pohybu pacienta na odhadnuté hodnoty FWHM. Byl posouzen vliv vstupního parametru FWHM na úspěšnost detekce.

Automatický odhad FWHM fungoval dle očekávání a odhadoval přiměřené hodnoty FWHM. Pohyb pacienta jen mírně ovlivňoval výsledky odhadu FWHM. Úspěšnost detekce hypometabolismu kriticky nezávisela na přesném FWHM, které bylo použito pro PVC.

Automatický odhad FWHM nebo FWHM uvedená výrobcem jsou v klinické praxi dobrou volbou pro provedení PVC a automatické detekce hypometabolismu. Tyto výsledky umožní soustředit se na další vývoj metody automatické detekce hypometabolismu.

**Klíčová slova:** FDG-PET, hypometabolismus, korekce efektu částečného objemu, epilepsie, efektivní rozlišení

# Contents

# Figures

# Tables

# List of Shortcuts used

| | | |
|---|---|---|
| **FCD** | Focal cortical dysplazia | Fokální kortikální dysplázie |
| **MRI** | Magnetic resonance imaging | Magnetická rezonance |
| **PET** | Positron emission tomography | Pozitronová emisní tomografie |
| **FDG** | 2-deoxy-2-[$^{18}$F]fluorglukosa | 2-deoxy-2-[$^{18}$F]fluorglukosa |
| **CT** | Computed tomography | Výpočetní tomografie |
| **FBP** | Filtered backprojection | Zpětná filtrovaná projekce |
| **IR** | Iterative reconstruction | Iterativní rekonstrukce |
| **PVE** | Partial volume efekt | Partial volume effect |
| **PVC** | Partial volume korekce | Partial volume correction |
| **pvcPET** | Partial volume corrected Positron emission tomography | Pozitronová emisní tomografie po korekci partial volume efektu |
| **GM** | Gray matter | Šedá hmota |
| **WM** | White Matter | Bílá hmota |
| **CSF** | Cerebrospinal fluid | Crebrospinální tekutina |
| **ESF** | Edge spread function | Rozptylová funkce hrany |
| **ToF** | Time-of-flight | Čas letu pozitronu |
| **LOR** | Line of response | Linie odpovědi |
| **FWHM** | Full width at half maximum | Šířka v polovině maxima |
| **I-S** | Inferior-Superior | Inferiorně-superiorní |
| **P-A** | Posterior-Anterior | Posteriorně-anteriorní |
| **L-R** | Left-Right | Pravo-levý |
| **AC** | Attenuation correction | Korekce útlumu |
| **IQR** | Interquartile range | Mezikvartilový rozsah |
| **PSF** | Ponit spread function | Rozptylová funkce |
| **MG** | Müller-Gärtner method | Müller-Gärtnerova metoda |
| **TPR** | Sensitivity | Senzitivita |
| **TNR** | Specificity | Specificita |
| **PPV** | Positive predictive value | Pozitivně prediktivní hodnota |
| **MCC** | Matthews correlation coefficient | Matthewsův korelační koeficient |

# Chapter 1

# Introduction

Epilepsy is a group of neurological disorders characterized by occurrence of spontaneous repeated epileptic seizures that are caused by abnormal brain activity. In developed countries, epilepsy is present in 0.5 % - 1 % of the population and is the most common serious neurological disorder [1]. Epilepsy can be caused by various factors: genetically determined higher excitability of neurons, malformations of cortical development, serious brain trauma, brain infection, brain tumor etc.

The standard way of epilepsy treatment is pharmacotherapy with anticonvulsant medications. However, the pharmacotherapy is not successful in approximately one-third of patients and these patients suffer from drug-resistant epilepsy. In case of drug-resistant focal epilepsy, the epileptic seizure is caused only by a limited region of brain cortex - by epileptogenic lesion. One of the treatment options for patients with drug-resistant focal epilepsy is epilepsy resective surgery. The main goal of resective surgery is the complete removal of the tissue of epileptogenic lesion. However, the delineation of the extend of epileptogenic tissue is a complex process which involves an interdisciplinary cooperation and fusion of results of many presurgical examinations.

Neuroimaging methods play an important role in presurgical examinations and localization of epileptogenic lesion. Magnetic resonance imaging (MRI) is a neuroimaging technique that is essential to detect structurally abnormal tissue and thus delineate the epileptogenic lesion. Positron emission tomography of 2-deoxy-2-[18F]fluoro-D-glucose radiotracer (FDG-PET) is a functional neuroimaging method that can also significantly contribute to the localization of the epileptogenic lesion. FDG-PET image visualizes the tissue metabolic activity associated with the consumption of glucose. The tissue of epileptogenic lesion often shows decreased metabolic activity (hypometabolism) and in the FDG-PET image it can be recognized as a region with hypointense signal [2].

However, the hypometabolic lesions can be very subtle and their identification in the MRI and PET image might be difficult. One of the important effects that limits the use of FDG-PET for precise localization of the subtle hypometabolic lesions is the low effective spatial resolution which leads to blurring of the image. The signals emitted from neighboring tissue structures mix together which results in so called partial volume effect (PVE). The PVE leads to an underestimation of radiotracer activity in the cortex. This effect can lead to spurious hypometabolic regions, resulting in an increased amount of false-positive hypometabolic regions.

Partial volume effect can be compensated using partial volume correction (PVC) which can additionally increase the effective spatial resolution of the PET image. Various methods for partial volume correction have been proposed [3]. One of the important inputs for partial volume correction methods is the full width at half maximum (FWHM) of the scanner point spread function (PSF). The incorrect specification of input FWHM influences the result of PVC and may lead to underestimation or overestimation of metabolic activity in the corrected PET image. The FWHM specified by the scanner manufacturer is usually used for partial volume correction. However, in clinical practice, it can be challenging to retrospectively find the type of PET scanner used and its spatial resolution. Moreover, the spatial resolution specified by the manufacturer might not corresponds to the spatial resolution achieved under the clinical acquisition and reconstruction protocol [4]. Therefore, a new method for fully automatic estimation of FWHM of the scanner PSF was proposed in this thesis that is independent of any a priori information about the PET scanner and the protocol used.

Another factor that influences the effective spatial resolution of the PET image is patient movement during the acquisition. Head motion during PET brain imaging is a well-known reason for blurred images and may lead to misinterpretation and even uselessness of the acquired image [5]. However, in clinical practice, head motion is not routinely quantified and is rather visually evaluated. Therefore, one of the objectives of this thesis is to quantify the patient movement during acquisition of PET scans in clinical practice and to assess the effect of movement on the automatic FWHM estimation method.

The visual assessment of hypometabolism in PET images is time consuming and strongly depends on the specific neuroradiologist and on the image contrast used for evaluation. Therefore a method for automatic detection of hypometabolic regions in PET images was proposed in the previous work [6]. The method detects the hypometabolic regions based of PET images that have been processed by partial volume correction. Therefore, the performance of the method may depend on the parameters of partial volume correction used. The effect of partial volume correction on the performance of automatic hypometabolism detection method was therefore investigated in this thesis.

## 1.1 Positron emission tomography

Positron emission tomography (PET) is a medical imaging technique that measure and visualize the concentration of a radioactive substance (radiotracer) in the tissue. Depending on the radiotracer used, the PET image visualizes various physiological processes in the patient body (metabolism, perfusion).

Radiotracer is a chemical compound in which one or more of the original atoms have been replaced by a radioisotope. The original substance and the radioisotope are selected so that the resulting radiotracer binds to a specific tissue proteins.

The radiotracer is administered to the patient in advance before the examination. The required advance depends on the half-life and metabolic dynamics of the radiotracer. The radiotracer then undergoes a positive beta decay (beta plus) in the target tissue of patient body and emits a positron ($e^+$) together with electron ($e^-$). The total energy of the moving particle depends on the mass of the radioisotope (heavier particles reach higher energies). The emitted positron travels through the tissue and looses kinetic energy through multiple collisions with electrons present in the neighboring tissues. The complete or almost complete loss of energy by the positron results into its combination (annihilation) with electron. The annihilation leads to emission of two gamma-photons with energy of 511 keV each in almost opposite directions [7] (Figure 1.1, A). The photons are emitted at almost 180 degrees to each other and their trajectories thus ideally form a line (also called the line of response - LOR). The pairs of gamma-photons further travel through the tissue and are then detected almost at the same time by the scintillation detectors of the PET scanner (Figure 1.1, B). The scintillation detector is composed of scintillation crystals ( e.g. Bismuth Germinate (BGO), Lutetium Oxyorthosilicate (LSO)) that absorb the energy of the gamma-photon and re-emit the absorbed energy in the form of light. The light is then detected and converted to electrical signal.

If a pair of positrons is detected by two scintillation detectors situated at the LOR in sufficiently short interval (4 - 12 ns [8]), the detection is considered a true detection of annihilated photons (coincidence event). Coincidence events can be stored either in a raw list-mode data format or in the form of sinogram. List-mode format uses data packets that contain information about the nature of the event, the detector pair address of the LOR detector, time markers and other [9]. In the case of sinogram, each LOR is represented by an angle and offset, and the value in the sinogram corresponds to the number of coincidences detected along the LOR in the specified time frame. Storing and processing list mode data is usually preferred in comparison to sinograms as the raw nature of the list-mode preserves all the spatio-temporal information which is partially lost using the sinogram format (e.g. it is difficult to correct for motion that occurred within the time frame of the sinogram) [9].

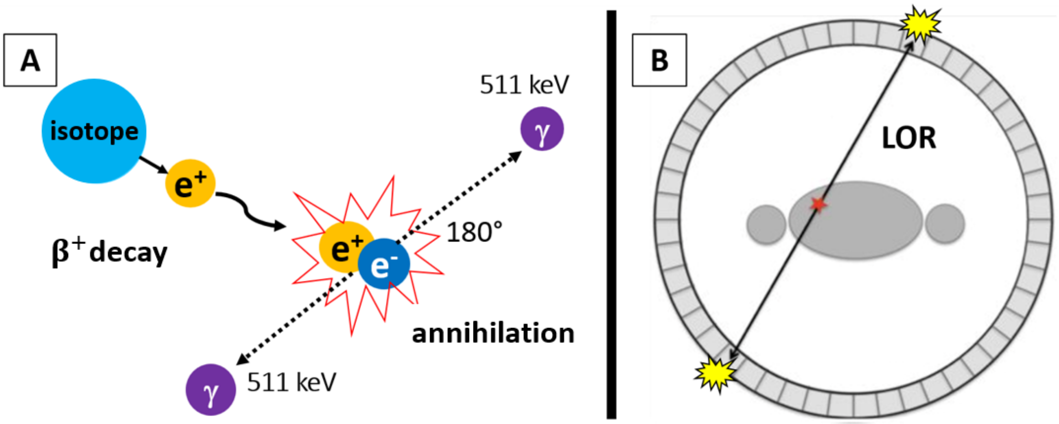

**Figure 1.1:** (A) Visualization of a positive beta decay and annihilation of the positron with the electron. (B) The pair of gamma-photons is simultaneously detected by a pair of opposite scintillation detectors. Their trajectories form a line of response - LOR. ([10], edited).

The resulting PET image is reconstructed based on the recorded coincidences. The traditional reconstruction techniques are based on an analytical Radon transform approach - e.g., filtered backprojection (FBP). Conversely, iterative reconstruction (IR) is based on estimating the probability of a particular data distribution being detected at individual locations for each projection. The IR better integrates additional data and information in the reconstruction process (e.g., attenuation correction, 1.3.1) and eliminates the noise and artifacts associated with FBP. Therefore, in clinical practice, iterative reconstruction is typically preffered over FBP and IR implementations are available as part of commercial software packages from major vendors [8].

In diagnostics of epilepsy, the typical radiotracer used for PET imaging is 2-deoxy-2-[18F]fluoro-D-glucose (FDG, Figure 1.2, A). The FDG is synthesized using 2-deoxy-2-glucose, where the normal hydroxyl group at the C-2 position in the glucose molecule is substituted with the radioisotope fluorine-18. The FDG-PET image visualizes the tissue metabolic activity associated with the consumption of glucose (Figure 1.2, B-D). The activity is often displayed using various color palettes (rainbow, iron etc.) rather than using a basic grayscale palette.

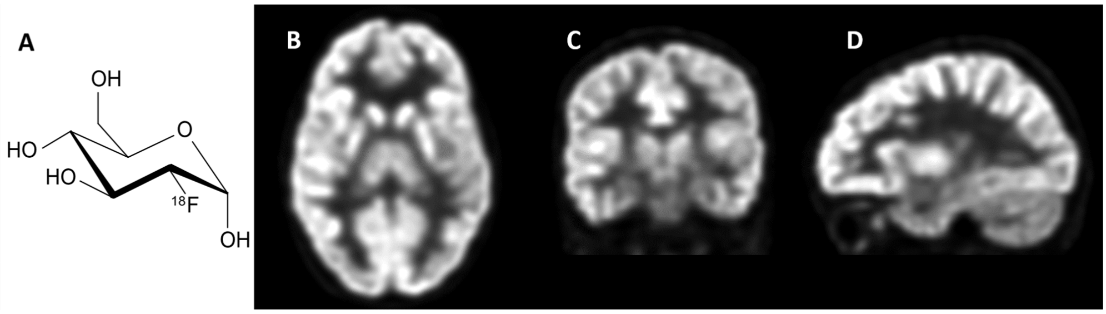

**Figure 1.2:** The scheme of the FDG molecule. (A) An example of FDG-PET image of the brain metabolic activity. (B-D).

## 1.2 Drug-resistant focal epilepsy

In drug-resistant focal epilepsy, the epileptic seizure is caused by a delimited region of brain cortex - by epileptogenic lesion. The most common cause of drug-resistant focal epilepsy is focal cortical dysplasia (FCD) [11]. Focal cortical dysplasia is a group of malformations of cortical development that are caused by improper migration of cells during the prenatal stage of brain development. This work is aimed at patients who are suspected of suffering from drug-resistant focal epilepsy based on FCD and might benefit from surgical treatment of epilepsy.

### 1.2.1 Surgical treatment of drug-resistant focal epilepsy

Epilepsy surgery is one of the treatment options for patients with drug-resistant focal epilepsy. The most common surgical method used to treat drug-resistant focal epilepsy is resective surgery, which is an established and effective therapeutic method in the treatment of patients with drug-resistant focal epilepsy, with an expected effectiveness of up to 80% [1], [12]. The main goal of resective surgery is complete removal of the epileptogenic tissue with preservation of the eloquent brain structures which leads to complete elimination of epileptic seizures or at least to significant reduction in their number and severity with preservation of patient cognitive functions.

In general, the extent of epileptogenic tissue region is not known with certainty when planning resection. Therefore, a compromise is sought between two approaches: to resect as much tissue as possible to achieve higher probability of including the entire epiletogenic region in the resection, or, on the contrary, to resect as little tissue as possible so that the procedure is maximally gentle and preserves the eloquent cortex and the physiological functions of the other areas [1]. The delineation of the extend of resection is a complex process which involves an interdisciplinary cooperation and fusion of results of many presurgical examinations. Neuroimaging methods play an important role in diagnostic and presurgical examinations. MRI is a fundamental neuroimaging technique used to reveal structurally abnormal tissue and thus delineate the epileptogenic lesion. Functional imaging methods such as PET can futher significantly contribute to localize the epileptogenic tissue.

### 1.2.2 Epileptogenic lesion in MRI and PET images

The brain cortex affected by focal cortical dysplasia often shows an abnormal signal in the neuroimaging modalities (MRI, PET). The most widely used neuroimaging modality for localization of FCD lesion is MRI, due to its good contrast and resolution for soft tissue imaging and the absence of ionizing radiation [1]. In MRI, the epileptogenic lesion is often characterized by cortical thickening (Figure 1.3 A, C), increased signal of gray and white matter tissue on T2/FLAIR weighted images (Figure 1.3 ,B, F), blurring of the gray-white matter interface (Figure 1.3 E) or a transmantle sign in the white matter tissue (Figure 1.3 D, C) [13]. However, especially in the cases of subtle or diffuse lesions, these characteristics are difficult to identify in the MRI and the image is then indicated as non-lesional. In non-lesional cases, another diagnostic methods must be used to localize the epileptogenic lesion and the presence of FCD can be confirmed only based on retrospective histological examination.

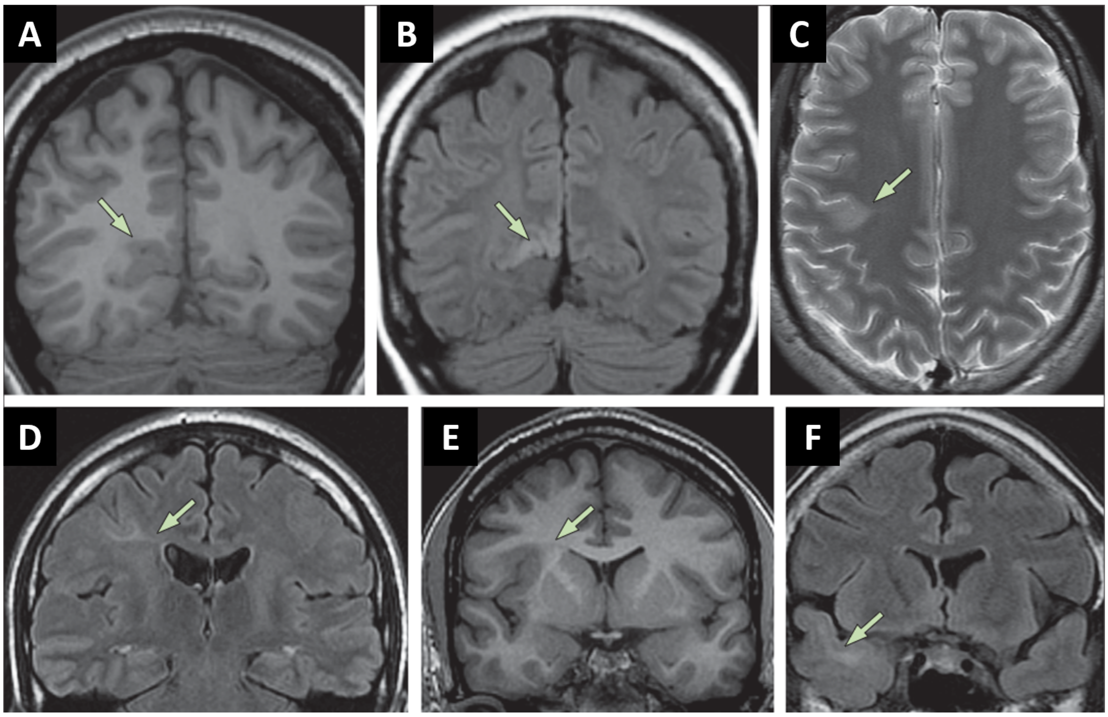

**Figure 1.3:** The typical characteristics of epileptogenic lesion caused by focal cortical dysplasia. (A, C) Cortical thickening. (B, F) Increased signal of gray and white matter tissue on T2/FLAIR weighted images. (C, D) The transmantle sign. (E) Blurring of the gray-white matter interface. [13]

Another modality important for the diagnostics of epilepsy caused by FCD is FDG-PET. The tissue of FCD epileptogenic lesion often shows decreased metabolic activity (hypometabolism) and in the FDG-PET image it is manifested as a region with hypointense signal. The FDG-PET examination can significantly help to localize the epileptogenic lesion especially in the non-lesional cases where the information from MRI is not available [14], [15]. However, the FCD hypometabolic lesions can be very subtle and their identification in the PET image might be difficult. One of the important effects that limits the use of FDG-PET for precise localization of the subtle hypometabolic lesions is the low effective spatial resolution which leads to blurring of the image [2].

The PET images are routinely assessed visually by neuroradiologists, often in corregistration with MRI to evaluate the relationship between the PET metabolic activity and anatomical structures. The hypometabolic regions are then identified either as the cortex regions with globally decreased metabolic activity or, in case of slight changes in metabolism, as cortex regions with relative decrease of metabolic activity compared to the contralateral anatomical region. However, the result of the visual assessment is subjective and strongly depends on the specific neuroradiologist and on the image contrast used for evaluation. Therefore, methods for automatic detection of hypometabolic regions has been proposed [16]–[23] that can assist the neuroradiologist to localize suspect hypometabolic regions and make the assessment simpler and faster.

In a previous work, a new method of hypometabolism detection was proposed [6]. The method is based on comparing the metabolic activity in contralateral brain regions of the anatomical atlas. The metabolic activity in each voxel of the cortex is compared with the overall metabolic activity of the contralateral anatomical region. As a result, a map of significantly hypometabolic voxels is obtained that has the same image dimension as the original PET image. The method also provides an option to perform the hypometabolism detection based of PET image whose effective spatial resolution has been increased by partial volume correction (see Sections 1.3, 1.4 for more details).

## 1.3 Effective spatial resolution of positron emission tomography

The effective spatial resolution of positron emission tomography (PET) describes the ability of the PET imaging to differentiate two independent objects. Another type of spatial resolution is the voxel size (sampling rate) of the PET image. In PET images, the voxel size is in general smaller compared to the effective resolution. Therefore, a low effective resolution results in apparent image blurring which affects the quality of the PET image. The effective resolution is influenced by many factors which are discussed in more detail in Sections 1.3.1 and 1.3.2.

The effective spatial resolution of the PET imaging can be described by a point spread function (PSF). PSF describes the response of a PET scanner to a point source, that is, the blurring of the point source in the resulting PET image (Figure 1.4, A). In general the PSF of the PET scanner is spatially variant — meaning that the PSF depends on the position of the point source in the field of view of the scanner. However, a spatially invariant PSF is usually assumed and the reconstructed PET image can be considered as a result of convolution of the true activity distribution with the PSF [3]. The PSF of the

PET scanner is often modeled as a Gaussian distribution that is uniquely defined by its full width at half maximum (FWHM), which can be different in different spatial directions [3]. FWHM represents the width of the point spread function measured between those points on the y-axis which are half the maximum amplitude (Figure 1.4, B). In case of normal Gaussian distribution, the FWHM directly depends on the standard deviation ($\sigma$) of the distribution according to relationship 1.1.

$$FWHM = 2 \cdot \sqrt{2 \cdot \ln(2)} \cdot \sigma \cong 2.355 \cdot \sigma \tag{1.1}$$

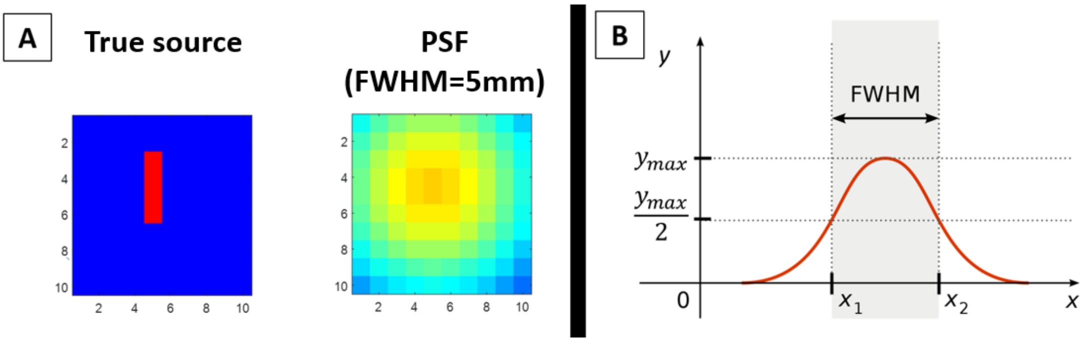

**Figure 1.4:** (A) The influence of the point spread function (PSF) on the source of activity signal (Image provided by supervisor of the thesis). (B) Visualization of FWHM (full width at half maximum).

The effective spatial resolution can be also described by the edge spread function (ESF). ESF describes the response of a PET scanner to a high contrast edge, that is, the blurring of a sharp edge in the resulting PET image. Edge spread function and point spread function are in direct relationship - ESF is given by the integral of the PSF. Therefore, under assumption that point spread function of PET scanner is modeled by normal Gaussian distribution, the edge spread function takes the form of normal cumulative distribution function [24]. In this case, the ESF can be uniquely defined by the FWHM of the underlying Gaussian distribution which is equal to the FWHM of the point spread function.

### 1.3.1 Factors influencing the fundamental effective spatial resolution

The effective spatial resolution is influenced by many factors. The most important of the factors are listed below.

#### Detector size

The resolution of the detector is given by the front size of the scintillation crystals which is in the range of 3-6 mm depending on the PET scanner model. The line of response (LOR) is therefore defined as the space of cuboid shape between two opposite scintillation crystals. Under this conditions, it is not possible to differentiate between two annihilations within the same LOR (Figure 1.5). Further distortions occur when a gamma-photon is detected in a different crystal than the one that the photon entered. The transfer of photon energy to the crystal and the subsequent light emission only occur at a certain depth of the crystal (>20 mm). If the source of the gamma-photon is located far from the center of field of view, the gamma-photon enters the crystal at an acute angle and can therefore be captured by a neighboring crystal which leads to a wrong LOR identification 1.5.

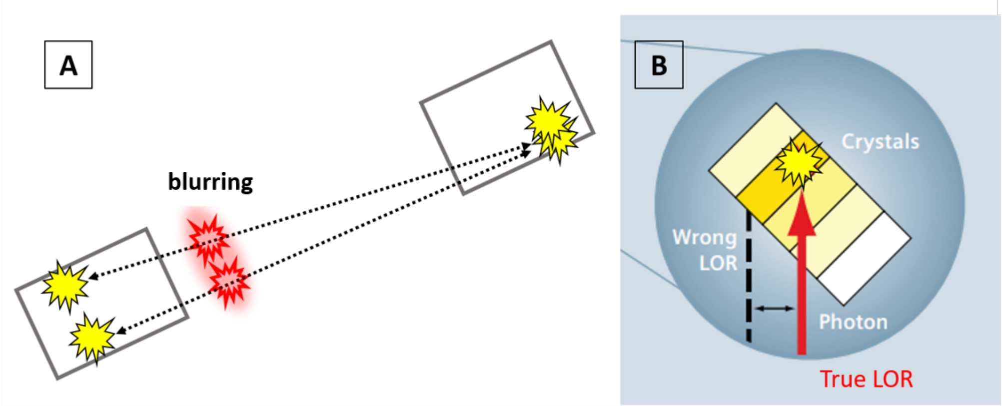

**Figure 1.5:** (A) Limitation of PET scanner resolution due to the scintillation detector size. (B) Incorrect detection due to acute angle of the line of response. The gamma-photon enters the crystal at an acute angle and can therefore be captured by a neighboring crystal which leads to a wrong LOR identification.[25].

### Random and multiple coincidence events

In the case when positrons are annihilated simultaneously at different location and always one of the pair of gamma-photons gets absorbed in the patient's body, the remaining two gamma-photons are incorrectly evaluated as a pair. A false LOR is therefore recorded (Figure 1.6, A). Multiple pairs of photons can also be detected at the same time. In this case, it is not possible to reliably distinguish the correct LOR where the annihilation occurred (Figure 1.6, B).

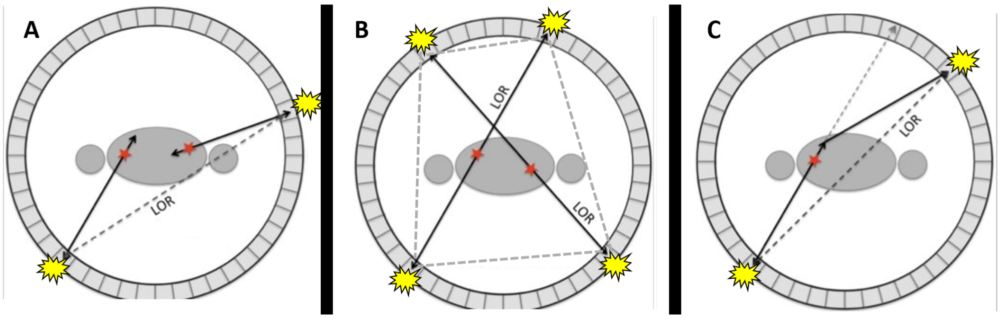

**Figure 1.6:** Visualization of the false detection of annihilation due to the random coincidence event (A), multiple coincidence event (B) and Compton scattering (C) [10], edited.

### Compton scattering

Gamma-photons emitted during annihilation can be deflected from their original opposite trajectories due to the Compton scattering. Therefore, the gamma-photons are detected by an incorrect pair of detectors along an incorrect LOR (Figure 1.6C). Due to the high energy of the photons (511 keV), the resolution is not strongly affected by the Compton scatter.

#### Positron range

The positron emitted during a positive beta decay travels a certain distance through the tissue before it gets annihilated. Therefore, the annihilation events that are later detected by the detectors occur at positions in a certain range from the original position (positron range). This results in the blurring of the image which is proportional to the positron range (Figure 1.1). The positron range depends on the radioisotope used (e.g. for $^{18}$F 0.2-2.4 mm, mean range 0.54 mm [26])

#### Photon attenuation

After annihilation, the gamma-photons travel through the tissue and loose energy through interactions with particles present in the neighboring tissues. Therefore, the photons might get absorbed in the tissue before they are detected by the scintillation detectors. This phenomenon is called a photon attenuation. The fraction of attenuated photons grows exponentially depending on the distance that the photon travels to reach the detector. The photon attenuation can lead up to 90% decrease in the number of detected coincidence events [27]. Therefore, it is necessary to perform the attenuation correction. The attenuation correction is based on estimation of the photon attenuation at the points of the scanner field of view using either information from a special PET transmission scan or from another modality (for combined CT-PET and MRI-PET scanners). However, inaccurate attenuation correction can significantly affect the final effective spatial resolution of the PET image [27].

### 1.3.2 The effect of patient movements on effective spatial resolution

The acquisition of brain PET scan usually takes several minutes. Therefore, it is difficult for the patient to to stay still during the acquisition. Head motion during PET brain imaging is a well-known reason for blurred images and may lead to misinterpretation and even uselessness of the acquired image [5]. The blurring of PET image results in an unrealistic representation of the true PET radiotracer distribution, increases the apparent size of the imaged target, and reduces the apparent radiotracer uptake of the target [28]. Patient movement can also cause a mismatch between emission and transmission (or CT) scan resulting in inappropriate attenuation correction [29]. The effective resolution of PET image can be therefore significantly deteriorated by artifacts caused by patient motion [30]. In the clinical practice, the visual evaluation of static PET images is generally not apparently influenced by slight head motion. However, the motion artifacts can induce an unrealistic picture of PET tracer distribution [30]. The patient movement can also influence results of statistical parametric evaluation of PET images [5], [29], [31]. The final degree of image deterioration does not only depend on the magnitude of the patient movement, but also on the fraction of the scan time that the movement has occurred [32]. As the effective spatial resolution of clinical PET scanners increases up to 3 mm, the negative effects of patient movement becomes even more important [30].

The head movement can be regarded as a rigid-body type of movement that can be described by three translations and three rotations in the direction of coordinate axis. The head movement can be measured either directly using external tracking system [5] or indirectly via corregistration of dynamic PET frames [29]. Several works quantified and reported patient head movement during acquisition of PET scan [29], [5], [33], a head movement during CT acquisition was reported in [34]. A translation of the head in range of 1-12 mm and rotation in range of 0.2-4.1° was reported across the publications. However, in clinical practice, head motion is not routinely quantified and is rather visually evaluated based on sinograms or reconstructed dynamic sequences.

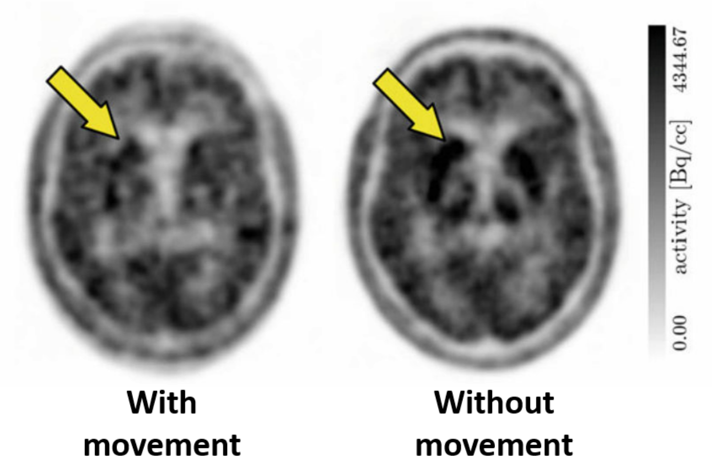

**Figure 1.7:** An example of the effect of patient movement during the acquisition of a PET scan on the effective spatial resolution of the reconstructed image.[35]

One approach to prevent and reduce head motion is to restrain the head during the PET scan by a support such as an individually molded cushion, by a thermoplastic mask, or even by a stereotactic device [5]. However, such solutions are uncomfortable for the patient. Moreover, even with head restraint, small head movements can occur during data acquisition that are sufficiently large to result in detectable artifacts in the final reconstruction. Even with the small movements recorded with head restraint, measurable effects can be demonstrated [31], [36]. Another approach that can significantly reduce the effect of patient motion is to reconstruct the PET image only based on frames that were not affected by movement [29].

Many methods that can correct patient movement have been proposed [36], [35], [28] [30]. However, motion correction was not routinely performed in clinical practice because it required installation of external device or implementation of specific software. Recently, the combined PET-MRI scanners started to be used in clinical practice that offer motion correction provided with the software from the manufacturer [37].

### 1.3.3 Measurement of effective spatial resolution of PET scanner

The effective spatial resolution of clinical PET scanners is standardly measured according to National Electrical Manufacturers Association (NEMA) standards [38]. According to NEMA standards, the effective spatial resolution should be characterized through point source measurements at different locations. The scans of the point source are reconstructed using the standard reconstruction protocol - filtered backprojection (FBP) with no smoothing or correction. Spatial resolution is then measured by calculating the FWHM of the point spread function from the image profiles along the radial, tangential and possibly also axial directions [4]. Axial resolution is measured in the direction of the main scanner axis (axis through the ring of scanner detectors) which corresponds to the Inferior-Superior axis in terms of patient position, the radial resolution is measured along the Left-Right axis and tangential resolution is measured along the Posterior-Anterior axis. The position of the point source changes in the Left-Right axis during the standard measurement. Therefore, radial resolution is expected to change depending on the point source position and conversely tangential resolution should remain the same. An illustration of radial and tangential resolution measurement is shown in Figure 1.8.

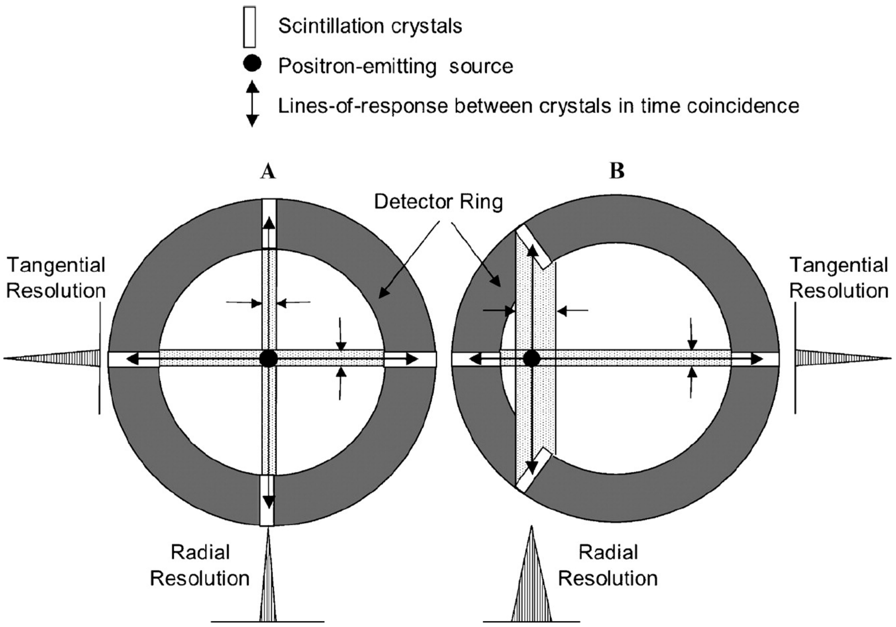

**Figure 1.8:** Visualization of the standard measurement of radial and tangential full width at half maximum (FWHM) of the scanner point spread function. [39]

As the FBP algorithm is linear, the measured spatial resolution is independent of any activity distribution in the background and is therefore suitable for resolution comparison among scanners [4]. In recent years, iterative reconstruction is typically preffered over FBP in clinical practice [8]. However, there is a mismatch between spatial resolution measured using the FBP algorithm and spatial resolution achieved using an iterative reconstruction [4]. Therefore, in order to measure clinical effective spatial resolution, it is desirable to measure the spatial resolution of a PET system using an iterative reconstruction algorithm directly. [4], [40].

Apart from a point source, other phantoms like a line source (capillary phantom) or cylinder phantom [24] can also be used to measure the spatial resolution of a PET system [4]. The capillary phantom is aligned to the scanner axis and the radial and tangential spatial resolution is measured analogically as for the point source according to NEMA standard [41]. In case of the capillary phantom, the axial resolution cannot be in principal measured because of the length of the capillary in the axial direction. In case of cylinder phantom, the effective resolution is measured through estimation of the edge spread function (ESF). The edge profiles through edges of the cylinder phantom are measured and fitted with analytical function. The FWHM of the edge spread function is then determined based on the parameters of the fitted analytical function[24].

The effective spatial resolution measured using one of the standard phantoms might not precisely represent the resolution achieved when imaging a real patient because of the effects of tissue scatter and attenuation and a limited number of acquired coincidence events [38]. Also the measurement using any of the standard stationary phantoms cannot in principle capture the potential effect of patient movement on the effective spatial resolution.

## 1.4 Partial volume effect

The hypometabolic areas on FDG-PET images corresponding to the FCD epileptogenic lesion can be very subtle and difficult to visually localize or automatically detect. One of the main reasons of this issue is the limited spatial resolution of the PET system [2]. The FWHM of the scanner point spread function is in the range of 4 - 6 mm for typical clinical PET. However, FWHM of 3 mm can be reached for the newest scanners [42]. Limited effective resolution causes blurring of the image of the metabolic activity. The signals emitted from neighboring structures mix together which results in so called spill-over effect between the nearby structures of the tissue. This effect is called a partial volume effect (PVE), an example of the partial volume effect is showed in Figure 1.9 A, B.

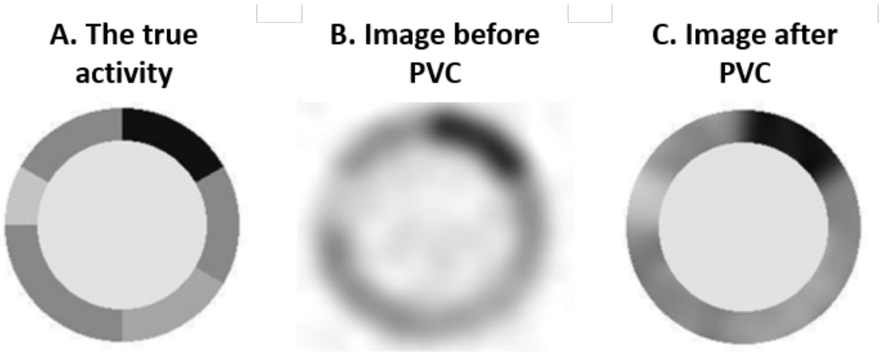

**Figure 1.9:** The phantom image represent the true activity of the radiotracer in the tissue. (B) The reconstructed PET image without partial volume correction (PVC). (C) The PET image after PVC [39], edited.

The severity of PVE is dependent on the size of the object being measured. Therefore, smaller structures with size comparable to the scanner FWHM are affected more than larger ones. The cortical thickness varies between 1 and 4.5 mm, with an overall average of approximately 2.5 mm [43]. Indicating that it the cortex be extensively affected by partial volume effect. PVE significantly affects especially the structures that are smaller than 2.5–3 times the FWHM of the scanner [2] which corresponds to the subtle cortex structures as bottoms of gyri or borderes of sulci. The PVE most seriously affects the edge area of target region, which has different tissue type or physiological state from adjacent regions [30].

A lower concentration of FDG is generally observed in white matter tissue and cerebrospinal fluid than in gray matter tissue. The PVE therefore leads to an underestimation of tracer activity in the cortex. This effect can lead to spurious hypometabolic regions, resulting in an increased amount of false-positive hypometabolic regions. Moreover, a spillover of activity to neighbouring regions can occur, leading to a misinterpretation of the extent of hypometabolic regions [2].

### 1.4.1 Partial volume correction (PVC)

The ultimate goal of partial volume correction (PVC) is to reverse the effect of the system PSF and eliminate the blurring of PET images which is caused by partial volume effect (PVE), an example of PVC is shown in Figure 1.9. Although the scanner PSF varies with position within the PET field-of-view, when applying PVC, the PSF is usually approximated by a spatially-invariant Gaussian kernel. While this simplification may not be appropriate for whole-body imaging, this assumption is generally accepted when applying PVC to brain PET data [44]. In this case, the PET image can be viewed as the result of convolution of the image of the true radiotracer activity with the scanner PSF. Thus, an approximation of the true image can be ideally obtained by deconvolution. Therefore, some of the methods for PVC are based on deconvolution of the PET image with the scanner PSF. However, this approach results in high-frequency noise amplification and introduction of artifacts, and some type of regularization must be used to avoid this effects [3].

Therefore, another anatomically based PVC methods were proposed that incorporate the anatomical information and tissue homogeneity constraints. The aim of anatomically based PVC methods is to utilize structural information from other imaging modalities (MRI, CT) as a priori information in order to to suppress the noise and artifacts. These modalities achieve better effective spatial resolution (FWHM $<$ 1mm), and therefore better depict the edges in the image and provide more accurate information about the high-frequency components of the image. Anatomically based PVC methods are therefore in principal based on the use of tissue segmentation of the structural image or parcellation into regions of the anatomical atlas [3]. Some of the anatomically based PVC methods perform the correction at the level of individual voxels, others estimate average values of entire anatomical regions.

PVC methods can either be included within the PET reconstruction or applied as a post-reconstruction step. Within-reconstruction PVC is often referred to as resolution recovery. Reconstruction PVC methods must be supported by the scanner manufacturer, or requires an implementation of reconstruction software, which is not easily obtainable outside of a research setting [44]. Post-reconstruction PVC methods utilize the existing reconstructed PET images and therefore can be used in both research and clinical setting. In this thesis, a post-reconstruction Müller-Gärtner method was used for partial volume correction 1.4.2.

One of the important inputs for most of the post-reconstruction methods is the full width at half maximum (FWHM) of the scanner point spread function. The incorrect specification of input FWHM influences the result of partial volume correction and may lead to underestimation or overestimation of metabolic activity in the corrected PET images [44]. The FWHM specified by the scanner manufacturer is usually used for partial volume correction. However, in clinical practice, it can sometimes be challenging to retrospectively find the type of PET scanner used and its spatial resolution. Moreover, the spatial resolution specified by the manufacturer is measured under standard protocol and therefore might not corresponds to the spatial resolution achieved under the clinical acquisition and reconstruction protocol. Also, the PET scanner point spread function in standardly measured using static phantoms and therefore does not capture the potential effect of patient movement on the effective spatial resolution.

It would therefore be beneficial to develop a method that would estimate the FWHM independently of any a priori knowledge of the PET scanner and the protocol used. Nevertheless, there have not been many works devoted to this topic. In one of the works, the PSF was estimated from the PET image line profiles drawn through centers of left and right carotid arteries defined in MRI [45]. However, this approach required a manual segmentation of carotid arteries in MRI which can be time consuming and prone to errors. Therefore, a new method for fully automatic estimation of FWHM of the scanner PSF was proposed in this thesis. The only inputs for the method are MRI and PET images and the method is therefore independent of any a priori information about the PET scanner and the protocol used.

### 1.4.2 Muller-Gartner method

In this thesis, partial volume correction was performed with Müller-Gärtner method [46] using implementation from publicly available PETPVC toolbox [44]. Müller-Gärtner method is one of the post-reconstruction methods for PVC. The method performs correction of radiotracer activity for each voxel in the gray matter tissue segment. Therefore, it can increase the quality of the PET image for visual or automatic evaluation of the hypometabolic regions in the brain cortex.

Müller-Gärtner method uses binary maps of the segments of gray matter tissue ($\mathbf{GM}$), white matter tissue ($\mathbf{WM}$) and cerebrospinal fluid ($\mathbf{CSF}$) obtained by segmentation of MRI image. The main assumption of the method is that the resulting PET image ($\mathbf{PET}$) can be described as a convolution of the PET image of true radiotracer concentration ($\mathbf{PET_{true}}$) with the tree-dimensional scanner PSF ($\mathbf{H_{PSF}}$, equation 1.2).

$$\mathbf{PET} = \mathbf{PET_{true}} \star \mathbf{H_{PSF}} \tag{1.2}$$

Image $\mathbf{PET_{true}}$ can be described as a sum of PET images of true radiotracer concentrations in brain tissues ($\mathbf{PET_{GM}}$, $\mathbf{PET_{WM}}$, $\mathbf{PET_{CSF}}$) that are spatially limited by the tissue segments $\mathbf{GM}$, $\mathbf{WM}$ a $\mathbf{CSF}$ (equation 1.3). The goal of the method is to obtain an approximation of $\mathbf{PET_{GM}}$.

$$\mathbf{PET_{true}} = \mathbf{PET_{GM}} \cdot \mathbf{GM} + \mathbf{PET_{WM}} \cdot \mathbf{WM} + \mathbf{PET_{CSF}} \cdot \mathbf{CSF} \tag{1.3}$$

After substitution of $\mathbf{PET_{true}}$ from equation 1.2 to the equation 1.3 and applying the linearity of the convolution operation, equation 1.4 is obtained.

$$\mathbf{PET} = (\mathbf{PET_{GM}} \cdot \mathbf{GM}) \star \mathbf{H_{PSF}} + (\mathbf{PET_{WM}} \cdot \mathbf{WM}) \star \mathbf{H_{PSF}} + (\mathbf{PET_{CSF}} \cdot \mathbf{CSF}) \star \mathbf{H_{PSF}} \tag{1.4}$$

To obtain a solution of Müller-Gärtner method, a simplifying assumption of constant activity of the radiotracer in the tissue of white matter and cerebrospinal fluid was applied. The intensity values in $\mathbf{PET_{WM}}$ and $\mathbf{PET_{CSF}}$ are therefore further substituted with constant values $\overline{PET_{WM}}$ (average over the **WM** segment, equation 1.5) and $\overline{PET_{CSF}}$ (zero value, 1.6). With those substitutions, equation 1.7 is obtained.

$$\overline{PET_{WM}} = \frac{\sum_v PET_{WM}(v)}{\sum_v WM(v)}, \qquad v \in \mathbf{WM} \tag{1.5}$$

$$\overline{PET_{CSF}} = 0 \tag{1.6}$$

$$\mathbf{PET} = (\mathbf{PET_{GM}} \cdot \mathbf{GM}) \star \mathbf{H_{PSF}} + (\overline{PET_{WM}} \cdot \mathbf{WM}) \star \mathbf{H_{PSF}} + (\overline{PET_{CSF}} \cdot \mathbf{CSF}) \star \mathbf{H_{PSF}} \tag{1.7}$$

Under assumption that $(\mathbf{PET_{GM}} \cdot \mathbf{GM}) \star \mathbf{H_{PSF}} = \mathbf{PET_{GM}} \cdot (\mathbf{GM} \star \mathbf{H_{PSF}})$ (does not hold in general), the final approximation of the image of radiotracer activity in the gray matter tissue $\mathbf{PET_{GM}}$ can be expressed according to equation 1.8. The nominator in the equation 1.8 corresponds to the correction of a spill-over effect from **WM** and **CSF** segments to **GM**, the denominator corresponds to to the correction of a spill-over effect from the **GM** segment to the other segments.

$$\mathbf{PET_{GM}} = \frac{\mathbf{PET} - (\overline{PET_{WM}} \cdot \mathbf{WM}) \star \mathbf{H_{PSF}} - (\overline{PET_{CSF}} \cdot \mathbf{CSF}) \star \mathbf{H_{PSF}}}{\mathbf{GM} \star \mathbf{H_{PSF}}} \tag{1.8}$$

The partial volume correction performed by Müller-Gärtner method thus provides the corrected values of radiotracer activity only in the segment of gray matter tissue. The diagram of the principle of partial volume correction performed by Müller-Gärtner method is shown in Figure 1.10.

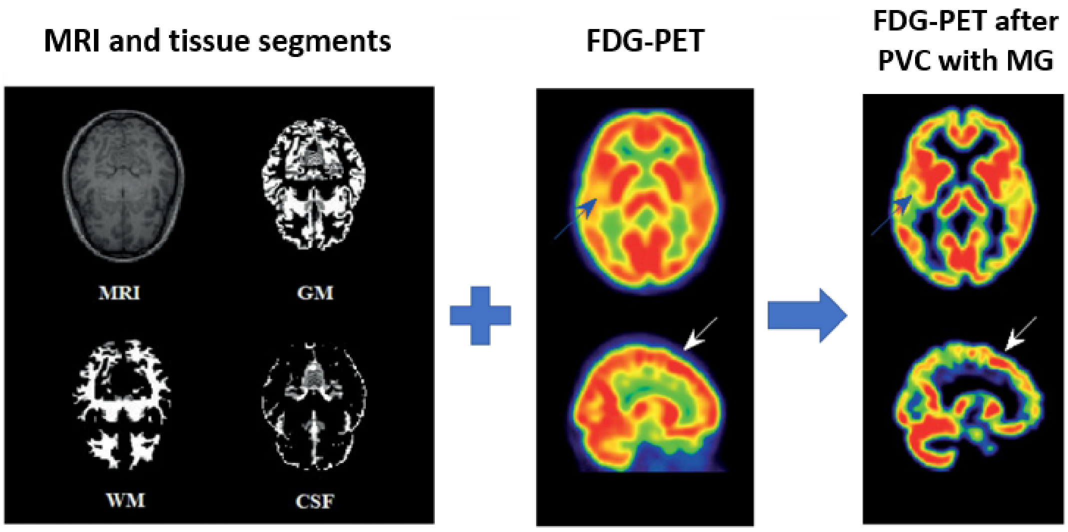

**Figure 1.10:** Visualization of partial volume correction (PVC) with Müller-Gärtner method (MG). The inputs of the method are the tissue segments GM, WM and CSF obtained by segmentation of magnetic resonance image (MRI) together with the FDG-PET image. The method outputs partial volume corrected FDG-PET images where the activity signal is focused to the gray matter region. [47], edited.

## 1.5 Motivation

Precise delineation of the epileptogenic lesion is a key factor that influences the result of the resective surgery in patients with drug-resistant focal epilepsy. The tissue of epileptogenic lesion is often hypometabolic. One of the important effects that limits the use of FDG-PET for precise localization of the subtle hypometabolic lesions is the low effective spatial resolution which leads to blurring of the image. The PET images are routinely assessed visually by neuroradiologists. However, the result of the visual assessment is time consuming and strongly depends on the specific neuroradiologist and on the image contrast used for evaluation.

The low effective resolution of PET images can be additionally compensated by partial volume correction which can possibly increase the quality of the PET image for visual and automatic assessment of hypometabolism. One of the important inputs for Müller-Gärtner partial volume correction method is the full width at half maximum (FWHM) of the scanner point spread function (PSF). The incorrect specification of input FWHM influences the result of PVC and may lead to underestimation or overestimation of the metabolic activity in the corrected PET image. The FWHM specified by the scanner manufacturer is usually used for partial volume correction. However, in clinical practice, it can be challenging to retrospectively find the type of PET scanner used and its spatial resolution. Moreover, the spatial resolution specified by the manufacturer might not corresponds to the spatial resolution achieved under the clinical protocol. Therefore, a new method for fully automatic estimation of FWHM of the scanner point spread function was proposed in this thesis. The method is independent of any a priori information about the PET scanner and the protocol used.

In order to validate the results of the method for automatic FWHM estimation, a reference measurement of the scanner PSF was performed under a clinical protocol using a capillary phantom. However, a phantom measurement cannot capture the effect of patient movements on the effective spatial resolution. Therefore, the movements of the patient head that occurred during the acquisition of PET images were measured and quantified. The effect of the patient movement on the automatic estimation of FWHM was investigated.

In a previous work, a method for automatic detection of hypometabolic regions in PET images was proposed. The method can assist the neuroradiologist to localize suspect hypometabolic regions and therefore make the assessment faster and statistically quantified. The method detects the hypometabolic regions based on PET images that have been processed by partial volume correction. Therefore, the performance of the method may depend on the parameters of the partial volume correction. The effect of FWHM on the performance of hypometabolism detection was therefore evaluated.

The main goal of this thesis was to investigate the effect of the main input parameter FWHM on the results of partial volume correction and automatic hypometabolism detection. This could allow to choose the best setting so that the methods are maximally beneficial for the assessment of PET images in clinical practice.

# Chapter 2

# Methods

A new method for fully automatic estimation of FWHM of the scanner point spread function is proposed in Section 2.3. It was necessary to validate the method with reference measurements of FWHM. The reference measurements could only be performed on scanners that were currently in use in the PET Center of the Na Homolce Hospital. The reference measurements of a capillary phantom were performed on Siemens Biograph mCT scanner and Siemens Biograph Vision scanner under the clinical protocol that was used to examine patients with epilepsy between 2022-2023 (see Section 2.2 for more details).

A Control dataset (dataset C, 2.1.1) was composed from patients with epilepsy who were examined on the same PET scanners under the same protocol as the capillary phantom. The protocol included PET images reconstructed by two types of OSEM iterative reconstruction and a dynamic PET sequence. Dataset C was used to validate the method for automatic estimation of FWHM with respect to the reference measurements according to Section 2.3. The dynamic PET sequences from dataset C were used to measure and quantify the patient movement during acquisition of a PET scan according to Section 2.4. The effect of measured movement on the estimated FWHM was then evaluated according to Section 2.4.3.

In a previous work, a method for automatic detection of hypometabolic regions in PET images was proposed [6]. One of the objectives of this thesis is to evaluate the effect of estimated FWHM on the performance of the method for automatic hypometabolism detection. The detection performance was evaluated based on an overlap of detected hypometabolic regions with the extend of surgical resection in patients with a seizure-free postsurgical outcome.

Therefore, the Test dataset (dataset T, 2.1.2) was composed from patients with drug-resistant focal epilepsy who underwent surgical resection, had a seizure-free postsurgical outcome, and whose extent of resection was delineated in MRI. Automatic estimates of FWHM were obtained for PET images of patients from dataset T according to Section 2.3. PET images of patients from dataset T were acquired at various clinics using various PET scanners, some of which are of unknown model or are no longer in operation. The FWHM values specified by the manufacturers (if available) were considered as an approximate reference for automatic FWHM estimation for dataset T. Dataset T was used to evaluate the effect of estimated FWHM on partial volume correction and automatic hypometabolism detection according to Section 2.5.

All tasks of this thesis were solved in MATLAB with the use of the SPM12 toolbox.

*3D Slicer 5.0.3* software was used for the visualizations of medical imaging data. The diagram of the pipeline of this thesis is shown in Figure 2.1.

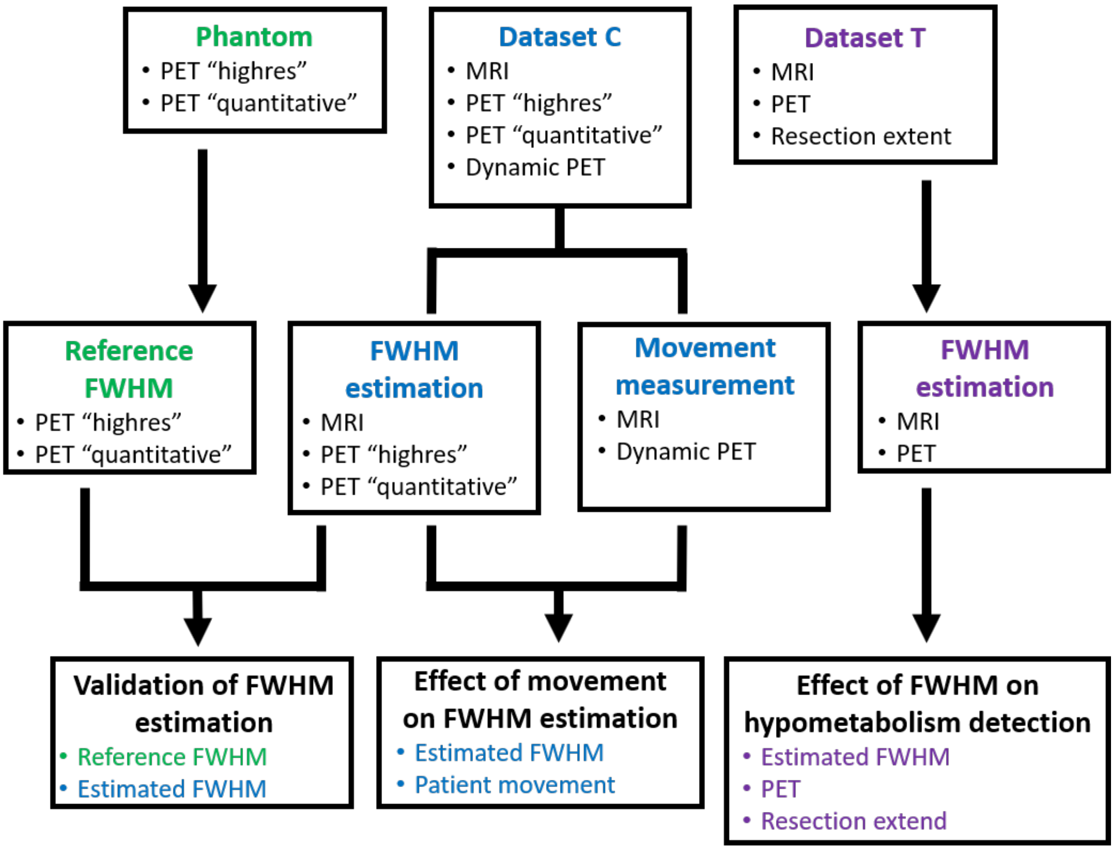

**Figure 2.1:** The diagram of the pipeline of this thesis. A method of automatic estimation of FWHM was proposed. The method was validated on the Control dataset (dataset C) with reference measurements using a capillary phantom. The patient movement during acquisition of the PET image was measured and quantified on the dataset C. The effect of patient movement on estimated FWHM was evaluated on dataset C. The effect of estimated FWHM on automatic hypometabolism detection performance was evaluated on the Test dataset (dataset T).

## 2.1 Data

This thesis was focused on patients who suffered with epilepsy and were candidates for surgical treatment of epilepsy in the Motol Epilepsy Center between 2009 and 2023. All of the patients underwent neuroimaging examination as one of the presurgical examinations. Some of the patients already underwent a resective surgery and some of them are still in the process of diagnostics. Control dataset and Test dataset were selected from these patient according to criteria described in 2.1.1 and 2.1.2.

### 2.1.1 Control dataset

Control dataset (dataset C) was selected to validate the method for automatic FWHM estimation and to quantify patient movements in the scanner during acquisition. The control dataset included patients who were examined on the same PET scanners under the same protocol as the capillary phantom.

Data from patients were selected according to the following criteria: (1) the patient underwent a presurgical structural MRI brain examination, (2) the patient underwent a presurgical FDG-PET brain examination at the PET Center of Na Homolce Hospital between 2022-2023, (3) The patient had not undergone resective surgery at the time of MRI and FDG-PET examination. The criteria were met by 31 patients.

FDG-PET examination was performed on Siemens Biograph mCT and Siemens Biograph Vision PET scanners under epi-protocol. A low-dose CT scan was obtained for attenuation correction followed by a PET scan. The reconstruction protocol included two types of OSEM iterative reconstruction [48], referred to as "highres" and "quantitative", and a reconstruction of dynamic PET sequence. The configuration of the "highres" and "quantitative" reconstruction parameters is listed in Table 2.1 for the Siemens Biograph mCT scanner and Table 2.2 for the Siemens Biograph Vision scanner. The dynamic PET sequence contained five dynamic scans obtained at a 2-minute interval and was reconstructed with OSEM iterative reconstruction without any correction.

**Siemens Biograph mCT**

| **reconstruction** | **Highres** | **Quantitative** |
|---|---|---|
| Matrix dimension | 400x400 | 200x200 |
| Number of iterations | 5 | 5 |
| Number of subsets | 21 | 21 |
| Gaussian filter | - | 4 mm |
| Corrections | ToF, AC, PSF | ToF, AC |

**Table 2.1:** Configuration of OSEM iterative reconstruction parameters for the Siemens Biograph mCT PET scanner. An attenuation correction (AC), time-of-flight correction (ToF) and point spread function correction (PSF) was used for the "highres" reconstruction. ToF and AC correction were used for "quantitative" reconstruction

**Siemens Biograph Vision**

| **reconstruction** | **Highres** | **Quantitative** |
|---|---|---|
| Matrix dimension | 440x440 | 220x220 |
| Number of iterations | 8 | 8 |
| Number of subsets | 5 | 5 |
| Gaussian filter | - | 4 mm |
| Corrections | ToF, AC, PSF | ToF, AC |

**Table 2.2:** Configuration of OSEM iterative reconstruction parameters for the Siemens Biograph Vision PET scanner. An attenuation correction (AC), time-of-flight correction (ToF) and point spread function correction (PSF) was used for the "highres" reconstruction. ToF and AC correction were used for "quantitative" reconstruction

### 2.1.2 Test dataset

The test dataset (dataset T) was selected to test the automatic FWHM estimation method and to assess the effect of the FWHM value on partial volume correction and automatic hypometabolism detection method performance. Data from patients were selected according to the following criteria: (1) the patient underwent resective surgery, (2) the patient underwent a presurgical and postsurgical structural MRI brain examination, (3) the extent of the resection was manually delineated using presurgical and postsurgical MRI, (4) two years after surgery outcome was classified as seizure-free, (5) the patient underwent a presurgical brain FDG-PET examination. The criteria were met by 32 patients.

FDG-PET examination was performed at various clinics in the Czech Republic and Slovak Republic with various scanners (Siemens Biograph Timepoint 40 HD, Siemens Biograph mCT, Siemens Biograph mMR, GE Medical Discovery LS, Siemens Biograph ECAT and unknown scanners) and protocols. The protocols included FDG-PET brain scan with attenuation correction applied but without including dynamic sequence. The spatial resolution of the PET scanners that was specified by the manufacturers was in the range of 4 to 6 mm. The information about spatial resolution was not available for unknown scanners and for Siemens Biograph ECAT because the exact model of the scanner was not specified.

The extent of resection was manually delineated using presurgical and postsurgical MRI and saved in a form of 3-dimensional binary label map using approach described in detail in the previous work [6].

## 2.2 Reference measurement of scanner effective resolution using a capillary phantom

The spatial resolution specified by the manufacturer is routinely measured under the standard acquisition and reconstruction protocol and might not accurately represent the spatial resolution in clinical settings. Therefore, spatial resolution was measured for Siemens Biograph mCT and Siemens Biograph Vision PET scanners under the same clinical acquisition and reconstruction protocol that was used to examine patients in the Control dataset (dataset C, 1.2.1). The settings of the protocol are specified in Section 1.2.1 and Tables 2.1 and 2.2. A capillary phantom of known size and activity was used to measure the reference spatial resolution.

The preparation of the capillary phantom and the acquisition and reconstruction of the PET phantom scans were performed by the radiological physicist Ing. Jiří Terš in the PET Center of the Na Homolce Hospital. The capillary phantom had a diameter of 0.1 mm and was 10 mm long in the case of the Siemens Biograph mCT scanner. In the case of the Siemens Biograph Vision scanner, the capillary had a diameter of 0.1 mm and was 3 mm long. In both cases, the capillary phantom had an activity of 10 MBq. The capillary phantom was attached to a polystyrene holder and aligned to the scanner's axis using positioning lasers. The phantom was then moved 1 cm and 10 cm horizontally with respect to the scanner's axis (I-S axis). A PET scan was acquired for each position of the phantom. The PET scans were reconstructed using both "highres" and "quantitative" reconstruction. As a result, a total of four reconstructed PET images of the phantom were obtained per scanner. Each of those PET images was then used to measure the spatial resolution of the scanner under the corresponding settings. A diagram that describes the reference measurement of the capillary phantom is shown in Figure 2.2.

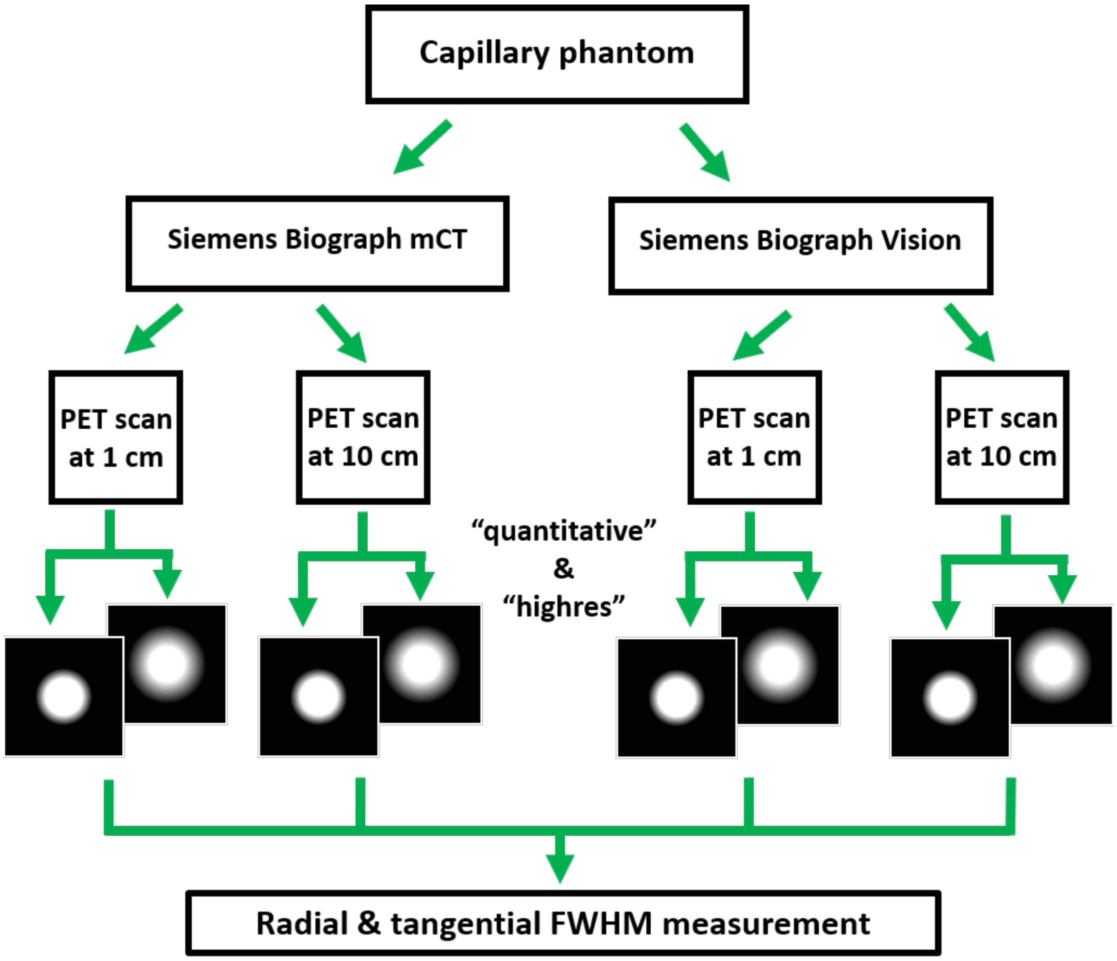

**Figure 2.2:** A diagram of the reference measurement of full width at half maximum (FWHM) using a capillary phantom. The capillary phantom was imaged on Siemens Biograph mCT and Siemens Biograph Vision scanner at positions 1 cm and 10 cm horizontally from the scanner axis. The scan of the phantom were reconstructed with "highres" and "quantitative" iterative reconstruction. The radial and tangential FWHM were then measured using reconstructed images.

### 2.2.1 Measurement of full width at half maximum

The effective spatial resolution was measured in the L-R axis direction to determine the radial resolution and in the P-A axis direction to determine the tangential resolution. The capillary phantom was not suitable for axial resolution measurement because the capillary length significantly exceeded the size of the voxel in the scanner axis (I-S) direction. The effective spatial resolution was described by FWHM of the point spread function.

The measurement was performed according to the NEMA NU 2-2018 standard for spatial resolution [38] as follows. A one-dimensional response function was formed along profiles through the PET image volume in directions of L-R and P-A axes through the peak of the activity distribution. The maximum value of the response function was determined by a parabolic function fit using the peak point and its two nearest neighboring points respectively. Each FWHM was determined by linear interpolation between adjacent pixels of the response function at half of the maximum value of the response function. The process of FWHM measurement is visualized in Figure 2.3.

The measured FWHM values were then used as a reference for evaluation of the automatic FWHM estimation method proposed in Section 2.3. The measured FWHM was also compared with the values specified by the scanner manufacturers.

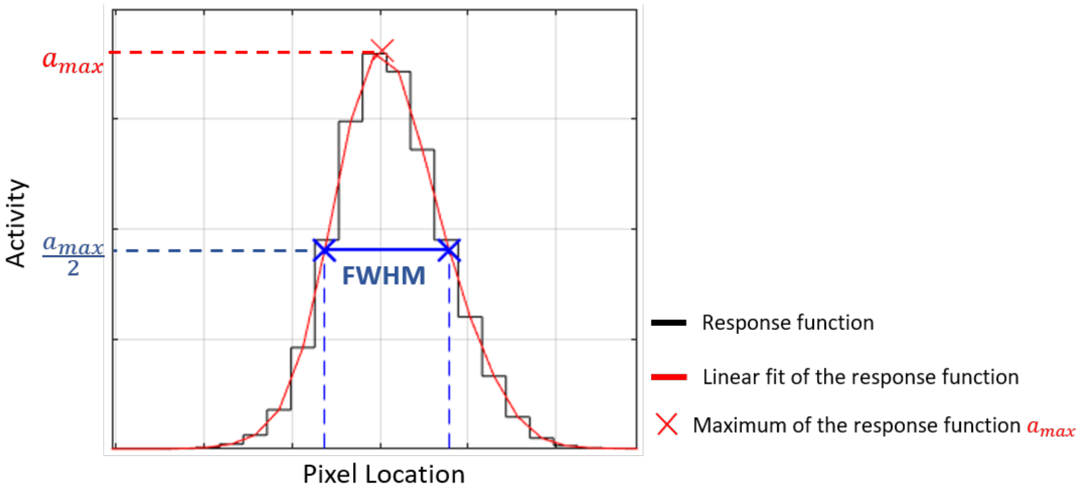

**Figure 2.3:** Visualization of the measurement of full width at half maximum (FWHM) according to NEMA standards. A response function is formed through the peak of activity distribution. The maximum value of the response function is determined by a parabolic fit. FWHM is determined by linear interpolation between adjacent pixels of the response function at half of the maximum value of the response function

## 2.3 Automatic FWHM estimation method

The FWHM of the point spread function (PSF) of the PET scanner is one of the fundamental input parameters of post-processing methods for partial volume correction. However, in clinical practice, it can sometimes be challenging to retrospectively find the type of PET scanner used and its spatial resolution. In the cases where the spatial resolution specified by the manufacturer is known, it is not clear whether it corresponds to the spatial resolution achieved under the clinical acquisition and reconstruction protocol. Therefore, in this thesis, a method for automatic estimation of the FWHM is proposed. The only inputs for the method are FDG-PET and MRI volumes and the method is therefore independent of any prior information about the PET scanner and the protocol used. The method outputs three values of the FWHM estimates in the L-R, P-A and I-S axes directions.

The main assumption for the method is that gray matter tissue is the dominant source of activity in the FDG-PET image and that neighboring tissue activity is significantly lower compared to gray matter [49]. The gray matter region can be obtained by segmenting the MRI volume. The gray matter region has a complex shape that is far from the point source, and direct measurement of the PSF is therefore not possible in this case. However, the lateral border of the gray matter can be regarded as a sharp step edge which is the source of activity. Under this assumption the gray matter border can be directly used to estimate the edge spread function (ESF). The method is therefore based on estimating the edge spread function rather than directly estimating the point spread function.

### 2.3.1 Definition of voxels of interest for the automatic FWHM estimation method

The aim of the method was to measure FWHM in the directions of the coordinate axes $x$ (L-R), $y$ (P-A), and $z$ (I-S). To achieve this, the ESF should be measured at the voxels where the lateral surface of the cortex is perpendicular to the axes or, in other words, where the normal vector of the surface is parallel to the axes (Figure2.4, 6-[1], 6-[2], 6-[3])). Additionally, the voxel should not be located in a sulcus because the signal from the neighboring cortex could corrupt the measurement (Figure2.4, 6-[2], 6-[3])).

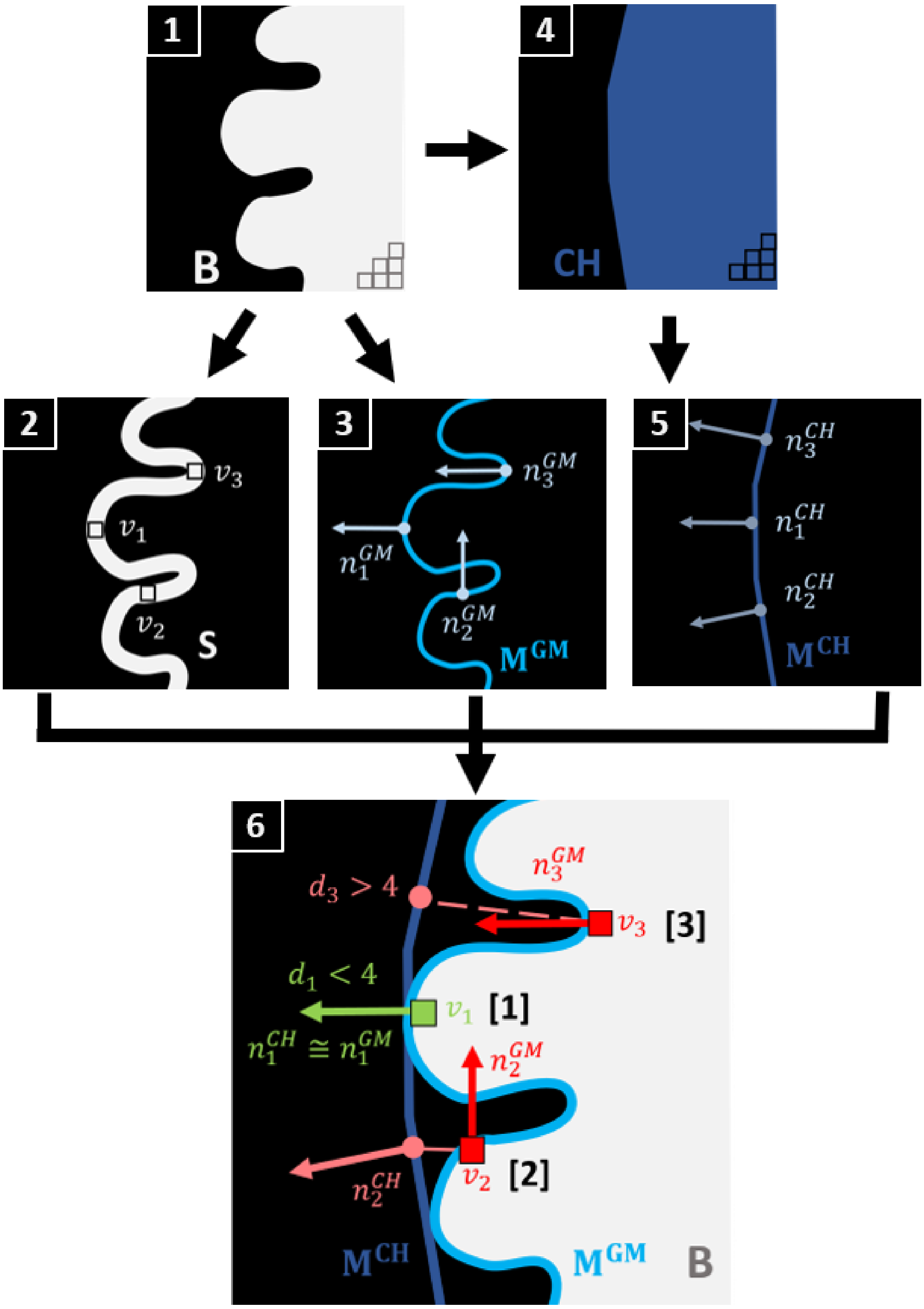

**Figure 2.4:** A diagram of selection of voxels of interest for the method for automatic estimation of FWHM. (1) The binary brain mask **B** is obtained a a union of gray matter and white matter tissue segments. (2) The surface **S** of the brain mask is obtained. (3) A vertex model $\mathbf{M}^{\mathbf{GM}}$ of the surface of the brain mask **B** is computed. (4) A convex hull **CH** of the brain mask **B** is obtained. (5) A vertex model $\mathbf{M}^{\mathbf{CH}}$ of the convex hull **CH** is computed. (6) The voxels of interest where the normal vectors $n_s^{GM}$ of the model $\mathbf{M}^{\mathbf{GM}}$ and also the normal vectors $n_s^{CH}$ of the model $\mathbf{M}^{\mathbf{CH}}$ are parallel to the axes are selected. The voxels with distance $d_s$ from the convex hull **CH** higher then 4.5 mm are excluded.

As a preprocessing step, MRI was segmented into brain tissue segments using *segment* function from SPM12 toolbox. The MRI and brain tissue segments were then corregistered and resliced to match the PET resolution with functions *coregister* and *reslice* from SPM12 toolbox. The binary brain mask **B** was obtained as a union of gray matter (GM) and white matter (WM) tissue segments. The brain mask **B** was a binary 3-dimensional volume (Figure 2.4, 1). The surface **S** of the brain mask **B** was obtained using the *bwperim* function from Image Processing toolbox for MATLAB. The surface **S** was a binary 3-dimensional volume where the voxels of the surface had value one. The voxels of the surface **S** are denoted $v_s$ where $s$ is a linear index into the volume **S** (Figure 2.4, 2). The vertex model $\mathbf{M^{GM}}$ of the brain mask **B** was obtained by *isosurface* function from MATLAB. Function *isonormals* from MATLAB was used to compute normal vectors of the vertices of the model $\mathbf{M^{GM}}$ (Figure 2.4, 3). Each surface voxel $v_s$ was assigned a normal vector $n_s^{GM}$, where the vector $n_s^{GM}$ was obtained as the mean of normal vectors corresponding to the two vertices from $\mathbf{M^{GM}}$ spatially nearest to the voxel $v_s$ (Figure 2.4, 6). The angles $\alpha_s^x$, $\alpha_s^y$, $\alpha_s^z$ between the coordinate axes $x$ (l-R), $y$ (P-A), and $z$ (I-S) and the normal vectors $n_s^{GM}$ were computed.

In order to eliminate the voxels situated in sulci, further processing followed. The convex hull **CH** of the brain mask **B** was obtained with *alphaShape* function from MATLAB. The convex hull **CH** was a binary 3-dimensional volume (Figure 2.4, 4). The vertex model of the convex hull $\mathbf{M^{CH}}$ was obtained with *isosurface* function from MATLAB. Function *isonormals* from MATLAB was used to compute normal vectors of the vertices of the model $\mathbf{M^{CH}}$ (Figure 2.4, 5). Each surface voxel $v_s$ was assigned a normal vector $n_s^{CH}$, where the vector $n_s^{CH}$ was obtained as the mean of normal vectors corresponding to the two vertices from $\mathbf{M^{CH}}$ spatially nearest to the voxel $v_s$. Each voxel $v_s$ was also assigned a distance in millimeters $d_s$ to the spatially nearest vertex from $\mathbf{M^{CH}}$ (Figure 2.4, 6). The angles $\gamma_s^x$, $\gamma_s^y$, $\gamma_s^z$ between the coordinate axes $x$ (l-R), $y$ (P-A), and $z$ (I-S) and the normal vectors $n_s^{CH}$ were computed. The sets of voxels of interest $\mathbf{V^x}$, $\mathbf{V^y}$, and $\mathbf{V^z}$ for the estimation of ESF along the axes $x$, $y$, and $z$ were selected according to criteria 2.1, 2.3, **??**.

$$\mathbf{V^x} = \{v_s : (\alpha_s^x < 10^\circ \vee \alpha_s^x > 170^\circ) \wedge (\gamma_s^x < 10^\circ \vee \gamma_s^x > 170^\circ) \wedge d_s < 4.5\} \tag{2.1}$$

$$\mathbf{V^y} = \{v_s : (\alpha_s^y < 10^\circ \vee \alpha_s^y > 170^\circ) \wedge (\gamma_s^y < 10^\circ \vee \gamma_s^y > 170^\circ) \wedge d_s < 4.5\} \tag{2.2}$$

$$\mathbf{V^z} = \{v_s : (\alpha_s^z < 10^\circ) \wedge (\gamma_s^z < 10^\circ) \wedge d_s < 4.5\} \tag{2.3}$$

The conditions on $\alpha_s^x$, $\alpha_s^y$, and $\alpha_s^z$ select voxels $v_s$ where the normal vectors to the brain surface $n_s^{GM}$ are parallel with the coordinate axes with the tolerance of ten degrees (Figure2.4, 6-[1], 6-[2],6-[3])). The conditions on $\gamma_s^x$, $\gamma_s^y$, and $\gamma_s^z$ eliminate the voxels $v_s$ on the side of sulci where the vector $n_s^{GM}$ is parallel with the coordinate axes but the normal vector to the convex hull $n_s^{CH}$ is not parallel with the coordinate axes with the tolerance of 10 degrees (Figure2.4, 6-[2]). The condition on $d_s$ eliminates the voxels $v_s$ at the bottom of sulci where the distance from the convex hull $d_s$ is high (Figure2.4, 6-[3]). If the size of the set $|V^x|$, $|V^y|$ or $|V^z|$ was less than four, the tolerance on corresponding $\alpha$ and $\gamma$ was increased by ten degrees and eventually by twenty degrees to increase the number of voxels in the set. In the case of the $z$ axis, only voxels with normal vectors in the same direction as the $z$ axis (from inferior to superior) were selected because the inferior part of the brain surface is surrounded by head tissue, which could corrupt the measurements.

### 2.3.2 Estimation of edge spread function parameters

The point spread function of PET scanners can be approximated by a Gaussian function [3]. Under this assumption, the edge spread function (ESF) is expected to have approximately the shape of a normal cumulative distribution function. The parameters of the ESF were therefore estimated by fitting a normal cumulative distribution function to the edge profiles through the selected voxels of interest $\mathbf{V^x}$, $\mathbf{V^y}$, $\mathbf{V^z}$ situated on the cortex border. Normal cumulative distribution function is parameterized by the mean and standard deviation of the underlying Gaussian normal distribution. The FWHM of the scanner PSF could therefore be obtained using the estimated standard deviation of the ESF according to relation 1.1. The FWHM estimate in the direction of $x$ (L-R) axis $FWHM^x$ was computed as follows. The process of estimation of the $FWHM_i^x$ is visualized in Figure 2.5.

A one-dimensional edge profile was formed through each of the voxels of interest $v_i^x$ from $\mathbf{V^x}$ along $x$ coordinate axis in the PET image. The local maximum $lmax_i$ and local minimum $lmin_i$ of the edge profile nearest to the position of voxel $v_i^x$ were found. The edge spread function of the cortex border $ESF_i^{CB}$ was determined as a section of the edge profile between the position of the local minimum $lmin_i$ with the offset of -3 mm and position of the local maximum $lmax_i$ with the offset of 2 mm. The offsets were selected experimentally to restrict the influence of signals from neighboring tissues. $ESF_i^{CB}$ was then normalized by the value of the local maximum $lmax_i$. A normal cumulative distribution function model (*normcdf*) with parameters $\mu$ (mean) and $\sigma$ (standard deviation) was fitted to $ESF_i^{CB}$ using a *fit* function from MATLAB. As a result, the estimates of $ESF_i^{CB}$ parameters mean $\hat{\mu_i^x}$ and standard deviation $\hat{\sigma_i^x}$ were obtained. Estimated $FWHM_i^x$ for each voxel of interest $v_i^x$ was computed according to Equation 2.4.

$$FWHM_i^x = 2 \cdot \sqrt{2 \cdot \ln(2)} \cdot \hat{\sigma_i^x} \cong 2.355 \cdot \hat{\sigma_i^x} \tag{2.4}$$

The overall FWHM estimate in the direction of $x$ axis $FWHM^x$ was computed as a median of estimated $FWHM_i^x$ values over all voxels of interest from $\mathbf{V^x}$ according to equation 2.5.

$$FWHM^x = \operatorname*{median}_i \left(FWHM_i^x\right) \tag{2.5}$$

The FWHM estimates $FWHM^y$, and $FWHM^z$ in the directions of $y$ (P-A) and $z$ (I-S) axes were obtained analogically.

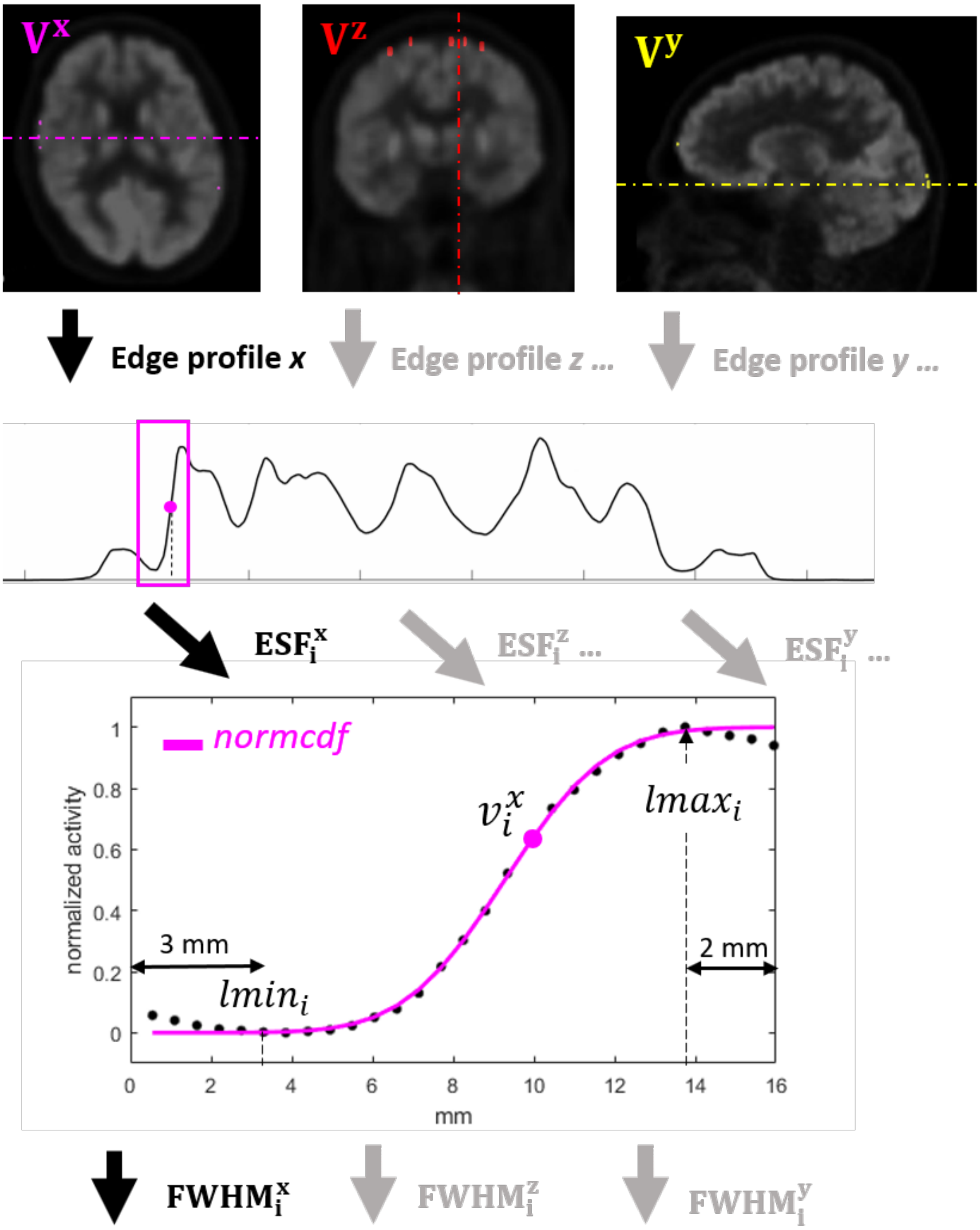

**Figure 2.5:** A one-dimensional edge profile was formed through each of the voxels of interest $v_i^x$ from $\mathbf{V^x}$ along $x$ coordinate axis in the PET image. The edge spread function of the cortex border $ESF_i^{CB}$ was determined as a section of the edge profile between the position of the local minimum $lmin_i$ with the offset of -3 mm and position of the local maximum $lmax_i$ with the offset of 2 mm. A normal cumulative distribution function model (*normcdf*) with parameters $\mu$ (mean) and $\sigma$ (standard deviation) was fitted to $ESF_i^{CB}$. Estimated $FWHM_i^x$ for each voxel of interest $v_i^x$ was computed using estimated $\sigma$ of the *normcdf*. The FWHM estimates $FWHM^y$, and $FWHM^z$ in the directions of $y$ (P-A) and $z$ (I-S) axes were obtained analogically.

### 2.3.3 Evaluation of automatic FWHM estimation method

The effective spatial resolution described by $FWHM^x$, $FWHM^y$, and $FWHM^z$ was estimated for each of PET images of the patients in control dataset (dataset C). Estimated FWHM values were compared with the reference values of FWHM that were measured using a capillary phantom according to Section 2.2. The absolute and relative error of the estimate from the reference were reported.

The effective spatial resolution described by $FWHM^x$, $FWHM^y$, and $FWHM^z$ was also estimated for each of PET images of the patients in test dataset (dataset T). In case of dataset T, it was not possible to conduct reference measurement. Estimated FWHM was therefore compared to the FWHM specified by the manufacturers.

## 2.4 Quantification of patient movements during acquisition of positron emission tomography scan

The movement of the patient in the scanner during the acquisition of the PET scan is one of the important factors that influences the effective spatial resolution of the PET image [28]. In extreme cases, patient movement can lead to complete deterioration of the image. However, patient movement is rarely systematically measured and quantified in clinical practice. A method for automatic estimation of PET image FWHM was proposed in Section 2.3. Considering that patient movement can influence the effective spatial resolution of PET images, the effect of patient movement on the method should be evaluated.

### 2.4.1 Description of patient movements with a rigid body transformation matrix

Direct measurement of patient movement in the scanner is problematic and cannot be performed retrospectively. Therefore, an indirect approach based on spatial rigid body corregistration of the dynamic PET sequence was used. All processing was performed in MATLAB with the use of the SPM12 toolbox.

The dynamic sequence included an initial CT transmission image and five dynamic PET images obtained in a 2-minute interval. The image origin of all images from the sequence was set at the anterior commissure of the first dynamic PET scan. The position of the patient on CT was considered the reference position. The movement of the patient relative to a reference position was measured using corregistration of dynamic PET images to the reference position. Direct corregistration of dynamic PET images to CT systematically failed due to different contrast of soft tissues. Therefore, an indirect corregistration using MRI was used. Initially, MRI was segmented into tissue segments. Then, MRI was corregistered to CT together with tissue segments. Finally, dynamic PET images were corregistered to gray matter tissue segment. The registration transformation matrices $\mathbf{T_{1-5}}$ obtained for each of the five dynamic PET images were then used to extract patient movement parameters.

## 2.4.2 Parametrization of patient movements

Each of the registration transformation matrices $\mathbf{T_{1-5}}$ was decomposed into translation and rotation components with *spm_imatrix* function. As a result, translation in L-R axis $t^x_{1-5}$, translation in P-A axis $t^y_{1-5}$, translation in I-S axis $t^z_{1-5}$, rotation about L-R axis $\theta^x_{1-5}$, rotation about P-A axis $\theta^y_{1-5}$ and rotation about I-S axis $\theta^z_{1-5}$ were obtained. Absolute values of the components $|t^x_{1-5}|$, $|t^y_{1-5}|$, $|t^z_{1-5}|$, $|\theta^x_{1-5}|$, $|\theta^y_{1-5}|$ and $|\theta^z_{1-5}|$ were computed to assess the magnitude of the movement regardless of the axis direction.

A 3-dimensional translation vectors $\mathbf{t_{1-5}}$ were obtained according to 2.6.

$$\mathbf{t_n} = \begin{bmatrix} t^x_n \\ t^y_n \\ t^z_n \end{bmatrix}, \qquad n = 1,..,5 \tag{2.6}$$

The magnitudes of translation $t_{1-5}$ were obtained as sizes of the translation vectors $\mathbf{t_{1-5}}$.

Rotation matrices $\mathbf{R_{1-5}}$ were formed using $\theta^x_{1-5}$, $\theta^y_{1-5}$ and $\theta^z_{1-5}$ according to 2.7 to follow the right-hand-rule convention[1].

$$\mathbf{R_n} = \begin{bmatrix} 1 & 0 & 0 \\ 0 & cos(\theta^x_n) & -sin(\theta^x_n) \\ 0 & sin(\theta^x_n) & cos(\theta^x_n) \end{bmatrix} \begin{bmatrix} cos(\theta^y_n) & 0 & sin(\theta^y_n) \\ 0 & 1 & 0 \\ -sin(\theta^y_n) & 0 & cos(\theta^y_n) \end{bmatrix} \begin{bmatrix} cos(\theta^z_n) & -sin(\theta^z_n) & 0 \\ sin(\theta^z_n) & cos(\theta^z_n) & 0 \\ 0 & 0 & 1 \end{bmatrix} \tag{2.7}$$
$$, n = 1,..,5$$

The angle-axis representation of the rotation was computed so that the overall rotation could be quantified. The absolute angles of 3-dimensional rotation $\theta_{1-5}$ were computed according to 2.8.

$$\theta_n = \cos^{-1}\left(\frac{\text{trace}(\mathbf{R_n}) - 1}{2}\right), \qquad n = 1,..,5 \tag{2.8}$$

The euler rotation axes $\mathbf{a_n}$ were computed according to 2.9.

$$\mathbf{a_n} = \frac{1}{2\sin(\theta_n)} \begin{bmatrix} (R_{n,32} - R_{n,23}) \\ (R_{n,13} - R_{n,31}) \\ (R_{n,21} - R_{n,12}) \end{bmatrix}, \qquad n = 1,..,5 \tag{2.9}$$

The displacement parameter was introduced to describe the total change in patient position and capture both the translation and rotation component of patient movement in one parameter. The initial RAS coordinates of voxels in the PET image $(\mathbf{X_0}, \mathbf{Y_0}, \mathbf{Z_0})$ were transformed by the transformation matrices $\mathbf{T_{1-5}}$ according to 2.10. The transformed coordinates $(\mathbf{X_{1-5}}, \mathbf{Y_{1-5}}, \mathbf{Z_{1-5}})$ corresponded to the position where the voxels were moved by the patient movement in each dynamic scan.

---

[1] SPM12 convention for rotations does not follow the right-hand-rule for the $x$ and $z$ axis. Therefore, the signs of $\theta^x_{1-5}$ and $\theta^z_{1-5}$ were flipped and the rotation matrices $\mathbf{R_{1-5}}$ were formed to follow the right-hand-rule convention instead of the SPM12 convention.

$$\begin{bmatrix}\mathbf{X_n}\\ \mathbf{Y_n}\\ \mathbf{Z_n}\\ \mathbf{1}\end{bmatrix} = \mathbf{T_n}\cdot\begin{bmatrix}\mathbf{X_0}\\ \mathbf{Y_0}\\ \mathbf{Z_0}\\ \mathbf{1}\end{bmatrix}, \qquad n = 1,..,5 \tag{2.10}$$

The displacement $\mathbf{d_{1-5}}$ of image voxels was computed as the distance between the initial and transformed coordinates of the voxels according to 2.11.

$$\mathbf{d_n} = \left\lVert\begin{matrix}\mathbf{X_n}-\mathbf{X_0}\\ \mathbf{Y_n}-\mathbf{Y_0}\\ \mathbf{Z_n}-\mathbf{Z_0}\end{matrix}\right\rVert, \qquad n = 1,..,5 \tag{2.11}$$

Due to the rotational component of movement, the displacement of individual voxels vary depending on their position in the image. Therefore, the mean displacements $d_{1-5}^{mean}$ and maximum displacements $d_{1-5}^{max}$ of voxels corresponding to the gray matter region **GM** were computed according to 2.12, and 2.13.

$$d_n^{mean} = \underset{i\in\mathbf{GM}}{\text{mean}}\left(d_n^i\right) \tag{2.12}$$

$$d_n^{max} = \max_{i\in\mathbf{GM}}\left(d_n^i\right) \tag{2.13}$$

Displacement $\mathbf{d_{1-5}}$ measure the distance between initial and final position of the voxel and does not account for the whole trajectory of the voxel movement. From this it follows that displacement cannot fully describe a "zigzag" type of movement. Therefore, a cumulative displacement was introduced that measure the total length of the voxel trajectory. A cumulative displacement $\mathbf{c_{1-5}}$ for each dynamic scan was computed according to 2.14.

$$\mathbf{c_n} = \left\lVert\begin{matrix}\mathbf{X_n}-\mathbf{X_{n-1}}\\ \mathbf{Y_n}-\mathbf{Y_{n-1}}\\ \mathbf{Z_n}-\mathbf{Z_{n-1}}\end{matrix}\right\rVert + \mathbf{c_{n-1}}, \qquad \mathbf{c_0} = \mathbf{0}, \qquad n = 1,..,5 \tag{2.14}$$

The mean cumulative displacements $c_{1-5}^{mean}$ and maximal cumulative displacement $c_{1-5}^{max}$ of the voxels from **GM** were computed according to 2.15 and 2.16.

$$c_n^{max} = \max_{i\in\mathbf{GM}}\left(c_n^i\right) \tag{2.15}$$

$$c_n^{mean} = \underset{i\in\mathbf{GM}}{\text{mean}}\left(c_n^i\right) \tag{2.16}$$

### 2.4.3 Evaluation of patient movement trajectory

The movement of patients during acquisition was parameterized according to 2.4.2 based on dynamic PET sequences from patients from the control dataset (dataset C). The movement was evaluated based on median and interquartile range of the parameters over the dataset C.

According to the observations of clinicians, if any movement is observed, the patients typically move steadily in the scanner and the magnitude of movement increases with the time spent in the scanner. Therefore, the monotonicity and increasing tendency of dynamic change of movement parameters was evaluated.

The magnitude of patients movements was quantified using shift $t$, rotation angle $\theta$, mean displacement $d^{mean}$ and maximum displacement $d^{max}$. The median values were reported together with the interquartile range.

In order to prevent patient movements, it can be beneficial to find out if there is any dominant type of movement that can be observed between patients. The difference in the magnitude of translation ($|t^x|$, $|t^y|$, $|t^z|$) and rotation ($|\theta^x|$, $|\theta^y|$, $|\theta^z|$) between coordinate axes was tested using Kruskal-Wallis test (function *kruskalwallis*) to identify the dominant axis of translation and rotation. The difference in the range of translational ($t^x$, $t^y$, $t^z$) or rotational ($\theta^x$, $\theta^y$, $\theta^z$) movement between coordinate axes was tested using Brown-Forsythe test on variances (function *vartestn*). The dominant axis with highest range of movement was eventually identified by post hoc tests using *vartesn* function with Bonferroni correction.

Estimates of FWHM for PET images from patients from the dataset C were obtained according to Section 2.3. The maximum cumulative displacement parameter $c^{max}$ was used to assess the effect of patient movement on FWHM estimates because it provided information about the total length of movement trajectory. PET images from dataset C were acquired on two scanners (Siemens Biograph mCT, Siemens Biograph Vision) with different effective spatial resolution. Therefore, the estimated FWHM was modeled with multiple linear regression to test whether the estimated FWHM can be predicted based on the scanner model and whether patient movement represented by the maximum cumulative displacement significantly influences the FWHM estimate. The model is described by equation 2.17 where $\overline{FWHM}$ denotes the average of estimated FWHM over coordinate axes, *scanner* is a discrete variable which denotes the PET scanner model, $\beta_0$ is the intercept, $\beta_1$, and $\beta_2$ are coefficients of the model and $\epsilon$ denotes the residuals.

$$\overline{FWHM} = \beta_0 + \beta_1 \cdot scanner + \beta_2 \cdot c^{max} + \epsilon \tag{2.17}$$

The effect of patient movement on estimated FWHM was also evaluated for each PET scanner independently by fitting a simple linear regression model according to equation 2.18.

$$\overline{FWHM} = \beta_0 + \beta_1 \cdot c^{max} + \epsilon \tag{2.18}$$

## 2.5 Effect of FWHM on automatic hypometabolism detection

The epileptogenic lesion is often hypometabolic [2], and FDG-PET images can therefore help to localize it. However, PET suffers from low effective resolution, which can complicate the localization of subtle hypometabolic lesions. Partial volume correction postprocessing methods can help to retrospectively increase effective spatial resolution. Full width at half maximum (FWHM) of the scanner point spread function (PSF) is one of the input parameters which influence the result of partial volume correction in most of the postprocessing methods including the Müller-Gärtner method [46] that was used for partial volume correction in this thesis. Therefore, one of the objectives of this thesis is to investigate the effect of the input FWHM on the result of partial volume correction performed with the Müller-Gärtner method.

Visual detection of hypometabolic regions in PET images is time consuming and may vary between radiologists. Therefore, a method for the automatic detection of hypometabolism was proposed in a previous work [6]. The method detects hypometabolic regions in the PET or pvcPET image. Briefly, the method is based on the comparison of metabolic activity in contralateral brain regions of the anatomical atlas. The metabolic activity in each voxel of the cortex is compared with the overall metabolic activity of the contralateral anatomical region using an asymmetry index. Hypometabolic voxels are then identified as voxels with significantly low asymmetry index values using a statistical z-test. As a result, a map of significantly hypometabolic voxels is obtained that has the same image dimension as the original PET image. The example of the map of significantly hypometabolic voxels is shown in Figure 2.6, C, in orange.

Detection performance was evaluated based on an overlap of detected hypometabolic voxels with the extent of surgical resection in patients with a seizure-free post-surgical outcome. The region of surgical resection was manually delineated based on MRI using approach described in [6]. The example of the delineated resection is shown in Figure 2.6, C, in blue. The dataset used for detection performance evaluation in the previous work is identical with the test dataset (dataset T) used in this thesis. However, implementation of Müller-Gärtner partial volume correction from PETPVC toolbox [44] was used in this thesis instead of PETPVE12 toolbox [50] that was used in the previous work because it returned infinite values for some of the voxels which corrupted the statistics. In the previous work [6], the hypometabolism detection based on pvcPET images showed better results compared to detection based on PET images. However, the identical value of FWHM (5mm) was used for partial volume correction of all PET images from the dataset. The effect of FWHM used for partial volume correction on the detection performance is therefore unclear.

Therefore, one of the objectives of this thesis is to investigate the effect of FWHM on automatic hypometabolism detection and to assess if the method is sensitive to a small change in the input FWHM.

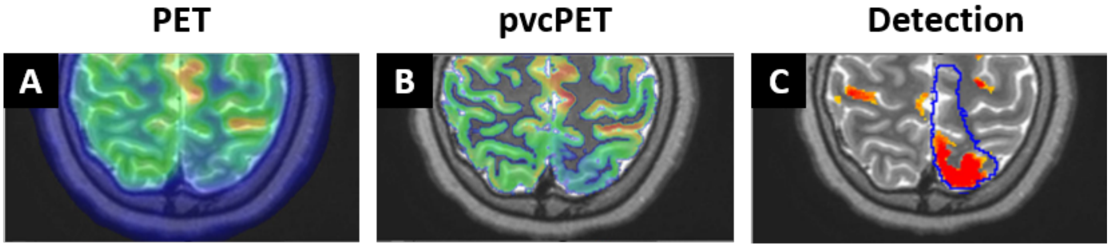

**Figure 2.6:** An example of the result of automatic hypometabolism detection. (A) The input for the method is the PET image. (B) The PET image is processed by partial volume correction. (C) The statistically hypometabolic voxels (in orange) are obtained as voxels with significantly low values of the asymmetry index. The detection performance is evaluated based on the overlap with the extent of surgical resection (in blue)

### 2.5.1 Effect of partial volume correction on metabolism measurement

The partial volume correction modifies the metabolic activity values of the original PET image to compensate the partial volume effect (PVE) and restore the true metabolic activity as accurately as possible. The metabolic activity of gray matter tissue is in general higher compared to other types of brain tissue and is therefore underestimated due to the partial volume effect. Partial volume correction compensates the PVE and increases the metabolic activity values. However, if the input FWHM is not specified correctly, the metabolic activity of gray matter can remain underestimated or conversely can get overestimated. Therefore, the effect of input FWHM on the result of partial volume correction of the gray matter metabolic activity was investigated.

The estimates of FWHM were computed for PET images from patients in the test dataset (dataset T) according to Section 2.3. pvcPET with input FWHM of 50, 100, 150, and 200 % of the estimated FWHM was computed with Müller-Gartner method implemented in PETPVC toolbox [44]. The original PET image is denoted **PET** and resulting pvcPET images are denoted $\mathbf{pvcPET^{50\%}}$,$\mathbf{pvcPET^{100\%}}$,$\mathbf{pvcPET^{150\%}}$ and $\mathbf{pvcPET^{200\%}}$.

The mean ratio ($MRA^{50\%}$) between the activity values in $\mathbf{pvcPET^{50\%}}$ and **PET** in the voxels corresponding to the region of gray matter **GM** was computed according to equation 2.19.

$$MRA^{50\%} = \operatorname*{mean}_{i \in \mathbf{GM}} \left( \frac{pvcPET_i^{50\%}}{PET_i} \right) \tag{2.19}$$

The mean ratios of activity $MRA^{100\%}$, $MRA^{150\%}$ and $MRA^{200\%}$ for $\mathbf{pvcPET^{100\%}}$, $\mathbf{pvcPET^{150\%}}$ and $\mathbf{pvcPET^{200\%}}$ were computed analogically. The median values of mean ratios of activity were reported together with the interquartile range. The effect of FWHM on the $MRA$ values was investigated.

### 2.5.2 Effect of partial volume correction on the hypometabolism detection

Dataset T included a map of delineated extent of resection for each patient. Therefore, it was possible to evaluate the effect of partial volume correction on the performance of the automatic hypometabolism detection. The hypometabolic voxels were automatically detected for the **PET** image and for each of the pvcPET images $\mathbf{pvcPET^{50\%}}$, $\mathbf{pvcPET^{100\%}}$, $\mathbf{pvcPET^{150\%}}$ and $\mathbf{pvcPET^{200\%}}$ obtained according to Section 2.5.1. The numbers of true positive (TP), true negative (TN), false positive (FP) and false negative (FN) classified voxels were computed. The performance of hypometabolism detection with respect to the extend of resection was investigated using sensitivity (TPR), specificity (TNR), positive predictive value (PPV) and Matthews correlation coefficient (MCC) parameters.

Sensitivity ($TPR$) is defined as the ratio of true positive classified voxels to all voxels of the resection (equation 2.20). It describes the fraction of voxels from the resection that were labeled as significantly hypometabolic.

$$TPR = \frac{TP}{TP + FN} \tag{2.20}$$

Specificity ($TNR$) is defined as the ratio of true negative classified voxels to all voxels from the cortex outside of the resection (equation 2.21). It describes the fraction of voxels from the cortex that were not labeled as significantly hypometabolic.

$$TNR = \frac{TN}{TN + FP} \tag{2.21}$$

Positive predictive value ($PPV$) is defined as the ratio of true positive classified voxels to all voxels that were labeled as significantly hypometabolic (equation 2.22). It describes the fraction of significantly hypometabolic voxels that corresponded with the resection.

$$PPV = \frac{TP}{TP + FP} \tag{2.22}$$

Matthews correlation coefficient ($MCC$) is defined by equation 2.23. It describes whether the detection performance was better or worse then random. Zero value of MCC means that the detection performance was comparable to a random result. MCC value equal to one means that the classification was correct for all voxels. MCC value equal to minus one means that the classification was false for all voxels.

$$MCC = \frac{TP \cdot TN - FP \cdot FN}{\sqrt{(TP + FP) \cdot (TP + FN) \cdot (TN + FP) \cdot (TN + FN)}} \tag{2.23}$$

MCC is suitable for evaluation of detection performance even in the cases where the classes are represented by unbalanced numbers of samples [51].

The performance of hypometabolism detection based on **PET**, $\mathbf{pvcPET^{50\%}}$, $\mathbf{pvcPET^{100\%}}$, $\mathbf{pvcPET^{150\%}}$ and $\mathbf{pvcPET^{200\%}}$ was described using $TPR$, $TNR$, $PPV$ and $MCC$ parameters. The effect of FWHM value used for partial volume correction on detection parameters was investigated using paired non-parametric Friedman test on 0.05 significance level (function *friedman* in MATLAB) and post hoc tests (function *multcompare* in MATLAB).

# Chapter 3

# Results

## 3.1 Reference measurement of scanner effective resolution using a capillary phantom

The reference measurement of effective spatial resolution of the Siemens Biograph mCT and Siemens Biograph Vision PET scanners was performed in a setup described in Section 2.2. A PET scan of the capillary phantom was acquired at positions 1 cm and 10 cm horizontally from the scanner axis. The scans were reconstructed under both "highres" and "quantitative" protocols. The full width at half maximum (FWHM) was measured according to the NEMA standard [38] for each of the resulting PET images of the phantom. The measured values of FWHM are reported in Table 3.1 for the Siemens Biograph mCT scanner and in Table 3.2 for the Siemens Biograph Vision scanner. The results of measurements for the Siemens Biograph mCT scanner are shown in Figure A.1 for "highres" reconstruction and Figure A.2 for "quantitative" reconstruction. The results of measurements for the Siemens Biograph Vision scanner are shown in Figure A.3 for "highres" reconstruction and in Figure A.4 for "quantitative" reconstruction.

Measured FWHM was in general higher for "quantitative" reconstruction compared to "highres" reconstruction. The manufacturer specified isotropic FWHM of 4.3 mm for Siemens Biograph mCT and isotropic FWHM of 3.7 mm for Siemens Biograph Vision under standard protocol. As expected, measured FWHM was lower under "highres" reconstruction compared to standard protocol. Measured FWHM was slightly higher in case of Siemens Biograph mCT scanner which corresponded to expectations. The tangential resolution was expected to be stable and the radial resolution was expected to increase across the positions of the phantom. This was satisfied only for the Siemens Biograph Vision scanner.

**Siemens Biograph mCT**

| **reconstruction** | **Highres** | | **Quantitative** | |
|---|---|---|---|---|
| **direction** | **radial** | **tangential** | **radial** | **tangential** |
| **FWHM at 1 cm** | 2.4 mm | 2.8 mm | 6.9 mm | 6.9 mm |
| **FWHM at 10 cm** | 2.6 mm | 2.4 mm | 7.1 mm | 8.1 mm |
| **average FWHM** | 2.5 mm | 2.6 mm | 7 mm | 7.5 mm |

**Table 3.1:** Results of reference measurement of FWHM for the Siemens Biograph mCT PET scanner.

**Siemens Biograph Vision**

| reconstruction | Highres | | Quantitative | |
|---|---|---|---|---|
| **direction** | **radial** | **tangential** | **radial** | **tangential** |
| **FWHM at 1 cm** | 2.6 mm | 2.5 mm | 5.4 mm | 5.4 mm |
| **FWHM at 10 cm** | 3.2 mm | 2.2 mm | 6.3 mm | 6.8 mm |
| **average FWHM** | 2.9 mm | 2.3 mm | 5.9 mm | 6.1 mm |

**Table 3.2:** Results of reference measurement of FWHM for the Siemens Biograph Vision PET scanner.

## 3.2 Automatic FWHM estimation

A method for automatic estimation of FWHM of the scanner point spread function was proposed in Section 2.3. The inputs for the method were PET and MRI volumes. The method is based on estimating the parameters of edge spread function (ESF) through the voxels of interest at the cortex border. The example of voxels of interest selected for estimation of ESF parameters in shown in 3.1. The example of the ESF of the cortex border together with fitted normal cumulative distribution function is shown in 3.2. The method generally performed as expected and returned reasonable values of FWHM. However, obviously incorrect values of FWHM were obtained in two cases where the PET images were acquired on older scanner models with voxel size larger than 4 mm.

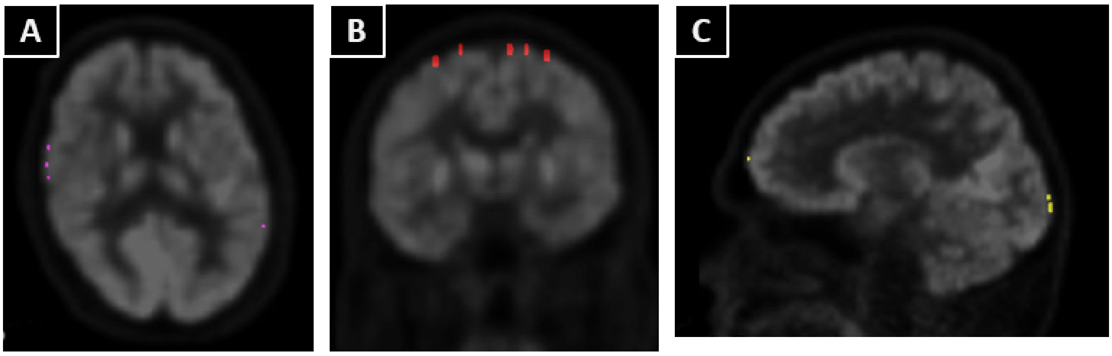

**Figure 3.1:** The example of voxels of interest selected for estimation of ESF parameters. (A) Voxels of interest for the Left-Right axis. (B) Voxels of interest for the Inferior-Superior axis. (C) Voxels of interest for the Posterior-Anterior axis.

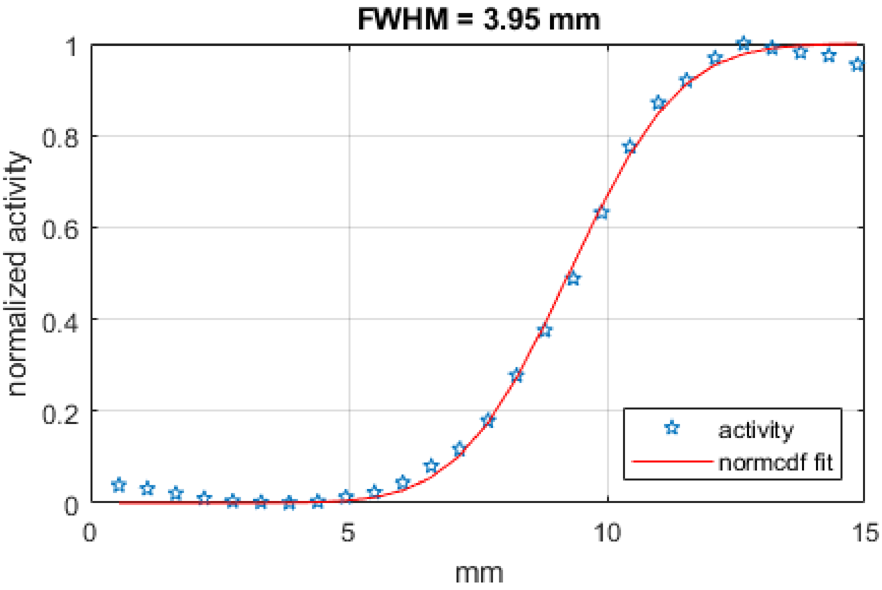

**Figure 3.2:** The example of the edge spread function together with fitted normal cumulative distribution function (*normcdf*). The FWHM was estimated using the parameters of the *normcdf*.

### 3.2.1 Automatic FWHM estimation for the control dataset

The automatic estimates of full width at half maximum (FWHM) were calculated for PET images of patients from the control dataset using the method described in Section 2.3. The control dataset included PET images that were acquired on the same PET scanners under the same reconstruction protocols as the reference PET images of the capillary phantom. The estimated FWHM values could therefore be compared with the reference FWHM values that were measured using a phantom according to Section 2.2. The median absolute and relative errors of the estimated FWHM were computed with respect to the reference average FWHM. The median estimated values of FWHM together with the absolute and relative errors are reported in Table 3.3 for the Siemens Biograph mCT scanner and Table 3.4 for the Siemens Biograph Vision scanner. The summary of the FWHM estimation results is visualized in Figure 3.3.

For "highres" reconstruction, the automatic FWHM estimates were 12-58 % overestimated compared to the reference. For "quantitative" reconstruction, the automatic FWHM estimates were 11-19 % underestimated compared to the reference. The variance of the FWHM estimates was in general higher for the $z$ (I-S) axis.

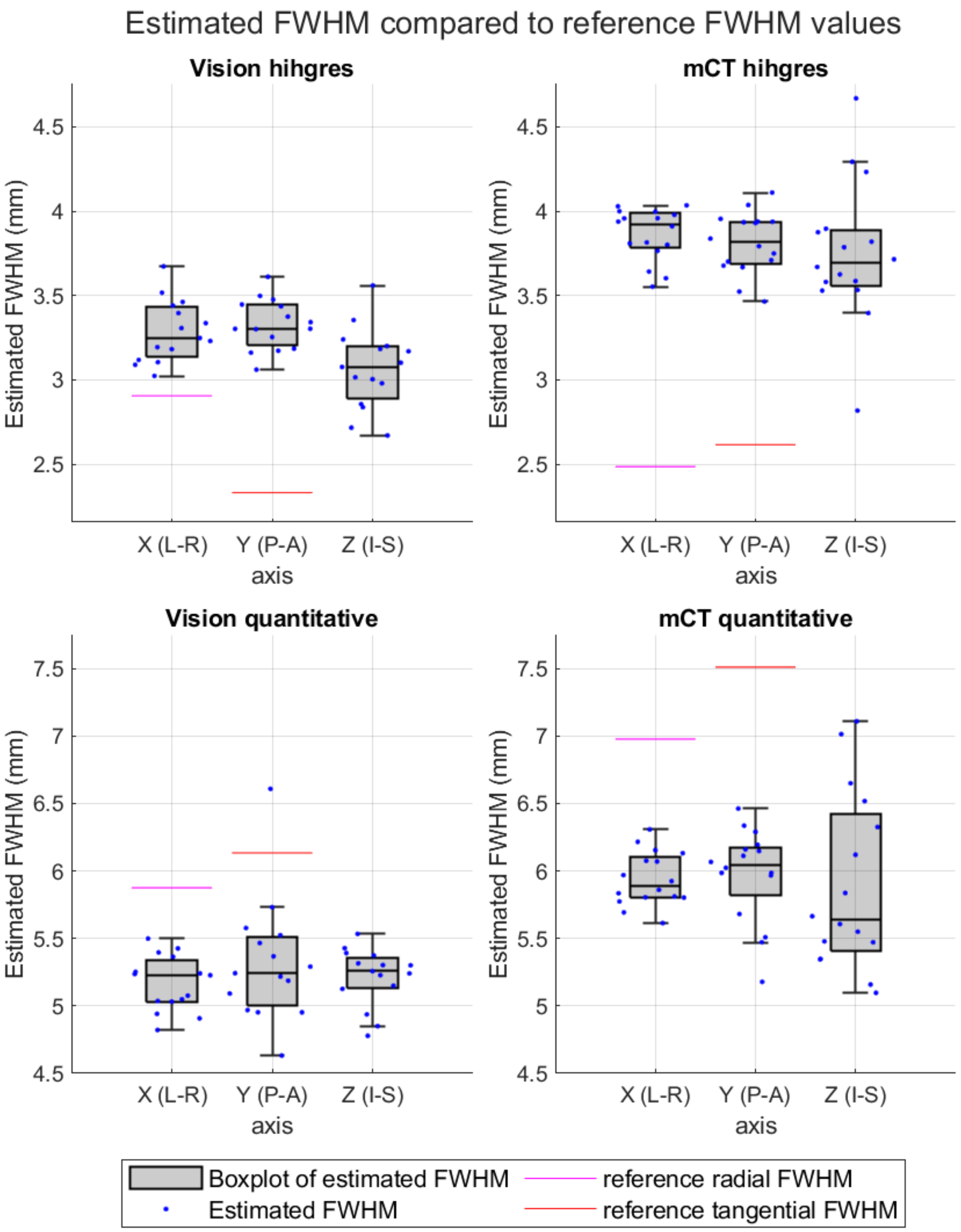

**Figure 3.3:** Resulting estimated FWHM in the directions of the coordinate axis for patients from the Control dataset. The estimated FWHM values are compared with the reference values. Patients from the Control dataset were examined on Siemens Biograph mCT and Siemens Biograph Vision scanners under "highres" and "quantitative" reconstruction protocol.

**Estimated FWHM for Siemens Biograph mCT**

| Reconstruction | Highres | | |
|---|---|---|---|
| **Direction** | **radial (L-R)** | **tangential (P-A)** | **axial (I-S)** |
| **Median FWHM (IQR)** | 3.9 (3.8-4) mm | 3.8 (3.7-3.9) mm | 3.7 (3.6-3.9) mm |
| **Av. reference FWHM** | 2.5 mm | 2.6 mm | NA |
| **Absolute error** | -1.4 mm | -1.2 mm | NA |
| **Relative error** | -58 % | -46 % | NA |

| Reconstruction | Quantitative | | |
|---|---|---|---|
| **Direction** | **radial (L-R)** | **tangential (P-A)** | **axial (I-S)** |
| **Median FWHM (IQR)** | 5.9 (5.8-6.1) mm | 6 (5.8-6.2) mm | 5.6 (5.4-6.4) mm |
| **Av. reference FWHM** | 7 mm | 7.5 mm | NA |
| **Absolute error** | 1.1 mm | 1.5 mm | NA |
| **Relative error** | 16 % | 19 % | NA |

**Table 3.3:** Results of the estimation of FWHM for the Siemens Biograph mCT PET scanner. The reference values of axial FWHM were not available (NA) for the capillary phantom.

**Estimated FWHM for Siemens Biograph Vision**

| Reconstruction | Highres | | |
|---|---|---|---|
| **Direction** | **radial (L-R)** | **tangential (P-A)** | **axial (I-S)** |
| **Median FWHM (IQR)** | 3.3 (3.1-3.4) mm | 3.3 (3.2-3.4) mm | 3.1 (2.9-3.2) mm |
| **Av. reference FWHM** | 2.9 mm | 2.3 mm | NA |
| **Absolute error** | -0.3 mm | -1 mm | NA |
| **Relative error** | -12 % | -42 % | NA |

| Reconstruction | Quantitative | | |
|---|---|---|---|
| **Direction** | **radial (L-R)** | **tangential (P-A)** | **axial (I-S)** |
| **Median FWHM (IQR)** | 5.2 (5-5.3) mm | 5.2 (4.6-5.7) mm | 5.3 (5.1-5.4) mm |
| **Av. reference FWHM** | 5.9 mm | 6.1 mm | NA |
| **Absolute error** | 0.6 mm | 0.9 mm | NA |
| **Relative error** | 11 % | 15 % | NA |

**Table 3.4:** Results of the estimation of FWHM for the Siemens Biograph Vision PET scanner. The reference values of axial FWHM were not available (NA) for the capillary phantom.

### 3.2.2 Automatic FWHM estimation for the test dataset

Automatic estimates of FWHM were also calculated for PET images of patients from the test dataset using the method described in Section 2.3. PET images of patients from the test dataset were acquired at various clinics using various PET scanners, some of which are of unknown model or are no longer in operation. Therefore, it was not possible to specify the reference value of FWHM under clinical protocol. The FWHM value specified by the manufacturers (if available) had to be considered as an approximate reference. The reference FWHM values were in the range of 4-6 mm.

The median of the estimated radial FWHM was 4.7 (4.3 - 4.8) mm, the median of the estimated tangential FWHM was 4.5 (4.2 - 4.9) mm, and the median of the estimated axial FWHM was 4.4 (3.9 - 5) mm. The estimated FWHM values for individual PET scanners are reported in Table 3.5 together with the mean voxel size. The summary of the FWHM estimation results for individual PET scanners is visualized in Figure 3.4, where the PET scanners are sorted according to the mean voxel size.

A trend of increasing values of estimated FWHM related to the increasing voxel size was observed. The estimated values of FWHM approximately corresponded to the values specified by manufactures. However, obviously incorrect value was obtained in case of radial FWHM of scanner "unknown 3" and also in case of axial FWHM of the scanner GE Discovery LS. In both cases, the size of the voxel in the corresponding axis exceeded 4 mm.

**Median estimated FWHM on test dataset**

| Scanner | radial (L-R) | tangential (P-A) | axial (I-S) | Voxel size |
|---|---|---|---|---|
| mCT | 4.1 mm | 4.1 mm | 4.5 mm | 1.2 mm |
| mMR | 4.4 mm | 4.4 mm | 3.9 mm | 1.4 mm |
| Truepoint | 4.7 (4.3-4.8) mm | 4.4 (4-5.2) mm | 4.2 (3.8-5.1) mm | 1.5 mm |
| unknown 2 | 4.9 mm | 5 mm | 4.6 mm | 2 mm |
| Discovery | 4.9 mm | 4.7 mm | 4.1 mm | 2.7 mm |
| ECAT | 7.8 mm | 6.6 mm | 6.9 mm | 2.8 mm |
| unknown 3 | 1.4 mm | 7.8 mm | 4.3 mm | 3.4 mm |

**Table 3.5:** Results of the estimated FWHM values for individual PET scanners. A median value of FWHM for each scanner is reported. The interquartile range is reported in case of sufficient number of estimated FWHM values per scanner.

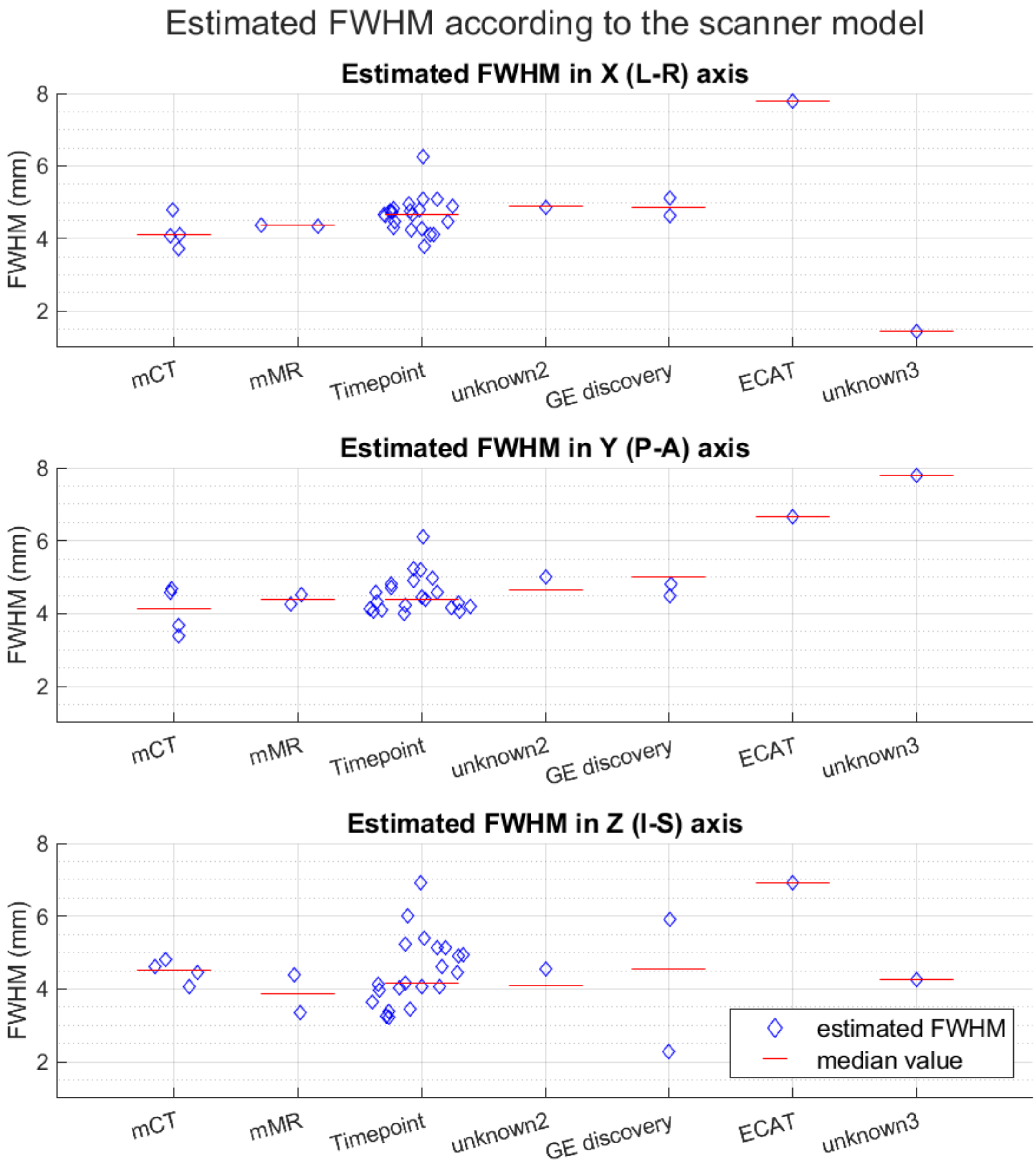

**Figure 3.4:** Resulting estimated FWHM in the directions of the coordinate axis for patients from the Test dataset. The results are displayed for individual PET scanners where the scanner are sorted according to the mean voxel size.

## 3.3 Quantification of patient movement during acquisition

The patient movement during acquisition of PET scan was evaluated based on dynamic PET sequence from patients from the control dataset according to Section 2.4. The control dataset included PET images and dynamic PET sequences that were acquired on the same PET scanners as the reference PET images of capillary phantom. Patient movement was parameterized to quantify the typical character and magnitude of movements according to

Section 2.4.3. The dynamic change in translation in the directions of the coordinate axes ($t^x_{1-5}$, $t^y_{1-5}$, $t^z_{1-5}$) is shown in Figure 3.5. The magnitude of translation in the directions of the coordinate axes ($|t^x_{1-5}|$, $|t^y_{1-5}|$, $|t^z_{1-5}|$) is shown in Figure 3.6. The dynamic change in rotation about the coordinate axes ($\theta^x_{1-5}$, $\theta^y_{1-5}$, $\theta^z_{1-5}$) is shown in Figure 3.7. The magnitude of rotation about the coordinate axes ($|\theta^x_{1-5}|$, $|\theta^y_{1-5}|$, $|\theta^z_{1-5}|$) is shown in Figure 3.8. The dynamic change in translation magnitude ($t_{1-5}$), rotation magnitude ($\theta_{1-5}$), mean and maximum displacement ($d^{mean}_{1-5}$, $d^{max}_{1-5}$), and mean and maximum cumulative displacement ($c^{mean}_{1-5}$, $c^{max}_{1-5}$) is shown in Figure 3.9.

In median, the parameters $t^x_{1-5}$, $t^y_{1-5}$, $t^z_{1-5}$, $\theta^z_{1-5}$, changed monotonically with time and the parameters $\theta^x_{1-5}$, $\theta^y_{1-5}$ changed almost monotonically with a maximum deviation from monotonicity of 0.1 mm (Figures 3.5, 3.7). In median, the parameters $|t^x_{1-5}|$, $|t^y_{1-5}|$, $|t^z_{1-5}|$, $|\theta^x_{1-5}|$, $|\theta^y_{1-5}|$, $|\theta^z_{1-5}|$, $t_{1-5}$, $\theta_{1-5}$, $d^{mean}_{1-5}$, $d^{max}_{1-5}$, $c^{mean}_{1-5}$, $c^{max}_{1-5}$ increased monotonically with time (Figures 3.6, 3.8, 3.9). The range of patient movement represented by the interquartile range was the largest for the last dynamic scan for all parameters. These results indicate that patients typically moved steadily in the scanner and the movement increased with time spent in the scanner. Therefore, all further analysis was performed on the parameter values corresponding to the last dynamic scan.

The total magnitude of patient movement was evaluated based on parameters $t_5$, $\theta_5$, $d^{mean}_5$, and $d^{max}_5$. Following values were measured for $t_5$: [1 (0.6-1.4) mm], $\theta_5$: [1.1 (0.7-1.9)°], $d^{mean}_5$: [1.6 (0.9-2.5) mm], and $d^{max}_5$: [2.7 (1.7-4.5) mm]. The results are visualized in Figure 3.9. The mean displacement $d^{mean}_5$ was comparable to the translation magnitude $t_5$. However, the maximum displacement $d^{max}_5$ was in median 1.7 mm larger than the translation magnitude $t_5$, indicating that in some brain regions the rotational movement $\theta_5$ accounted for the majority of displacement.

The typical character of patient movement was evaluated according to Section 2.4.3. The range of patient movement in the coordinate axes was represented by the interquartile range of parameters $t^x_5$, $t^y_5$, $t^z_5$, $\theta^x_5$, $\theta^y_5$, $\theta^z_5$. The magnitude of patient movement in the coordinate axis was represented by parameters $|t^x_5|$, $|t^y_5|$, $|t^z_5|$, $|\theta^x_5|$, $|\theta^y_5|$, $|\theta^z_5|$. There was a significant difference in the range of translational movement between the coordinate axes ($p$=0.003, Brown-Forsythe, Figure 3.10). The range of translational movement on the $z$ axis (I-S) was significantly larger than on the $y$ (P-A) axis ($p$=0.02; Bonferroni). However, there was no preferred translation direction in the $z$ axis ($p$>0.05; signed rank). There was a significant difference in the magnitude of translational movement between the coordinate axes ($p$=0.004, Kruskal-Wallis, Figure 3.10). The magnitude of translational movement in $z$ axis was significantly larger than in $y$ axis [$z$: 0.7 (0.3-1.2) mm, $y$: 0.3 (0.1-0.5) mm; $p$ =0.007; Tukey-Kramer] and larger than in the $x$ axis [$z$: 0.7 (0.3-1.2) mm, $x$: 0.3 (0.1-0.7) mm; $p$ =0.055; Tukey-Kramer].

There was a significant difference in the range of rotational movement between the coordinate axes ($p$=0.004, Brown-Forsythe, Figure 3.10). The range of rotational movement around the $x$ axis was significantly larger than around the $y$ axis ($p$=0.003; Bonferroni). However, there was no preferred rotation direction for the $x$ axis ($p$>0.05; signed rank). There was a significant difference in the magnitude of rotation between the coordinate axes ($p$=0.004, Kruskal-Wallis, Figure 3.10). The magnitude of rotation about the $x$ axis was significantly larger than about the $y$ axis [$x$: 0.8 (0.5-1.6)°, $y$: 0.4 (0.2-0.6)°; $p$=0.007; Tukey-Kramer] and the $z$ axis [$x$: 0.8 (0.5-1.6)°, $z$: 0.4 (0.2-0.7)°; $p$=0.017; Tukey-Kramer].

These results indicate that patients typically rotated their head about the $x$ (L-R) axis and translated their head in the $z$ (I-S) axis, that is, they rotated their chin up or down ("nodded") and moved their head up or down towards their feet.

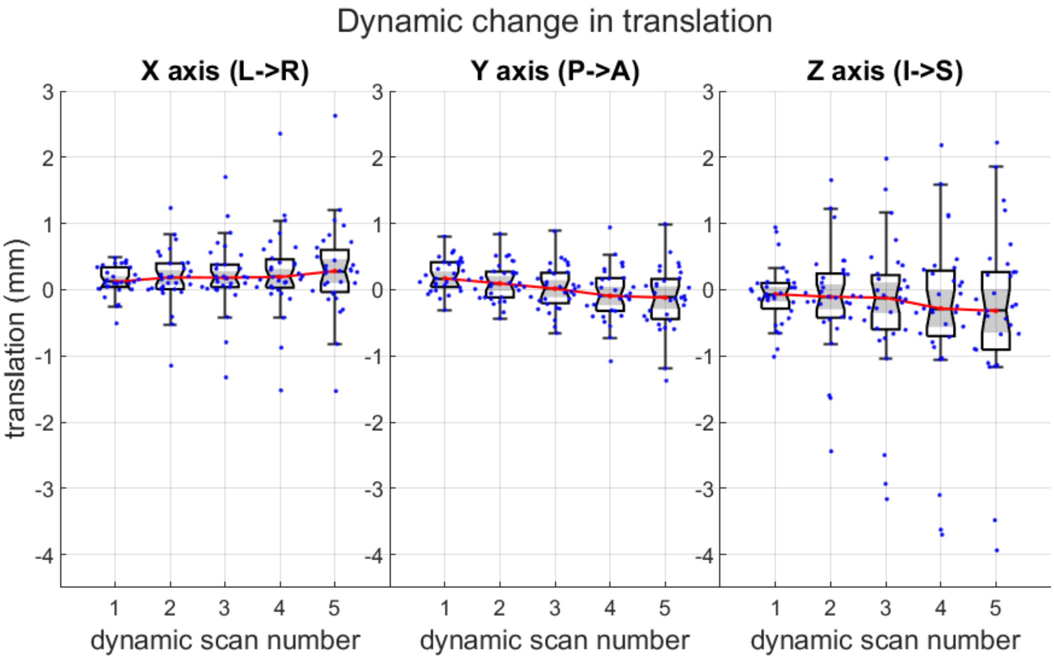

**Figure 3.5:** Dynamic change in translations in the directions of coordinate axes $t^x_{1-5}$, $t^y_{1-5}$, $t^z_{1-5}$.

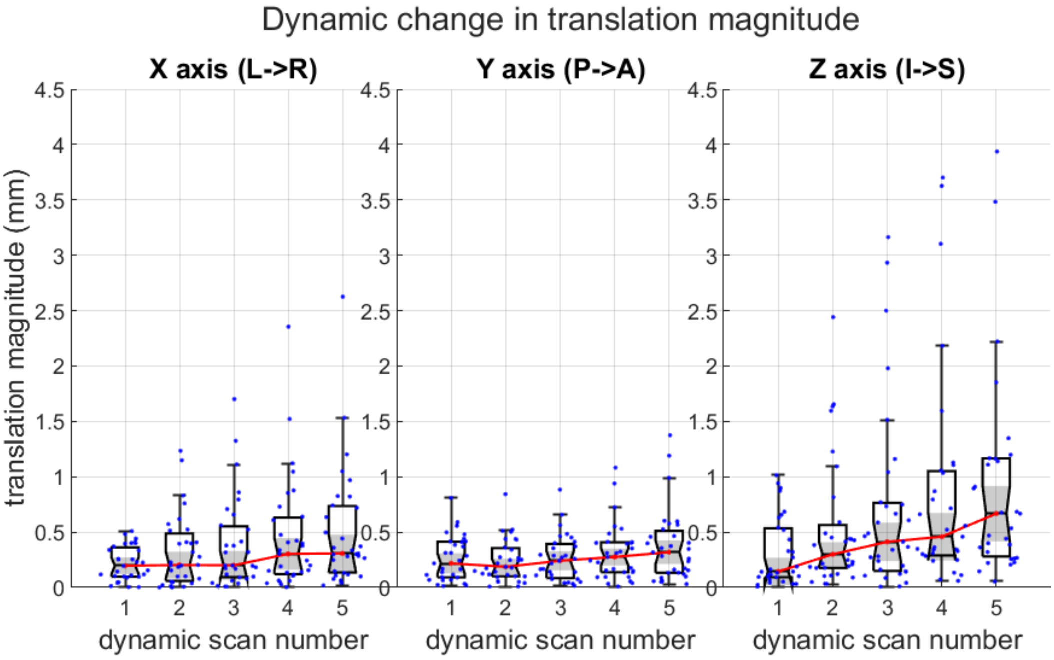

**Figure 3.6:** Dynamic change in the magnitudes of translations in the directions of coordinate axes $|t^x_{1-5}|$, $|t^y_{1-5}|$, $|t^z_{1-5}|$.

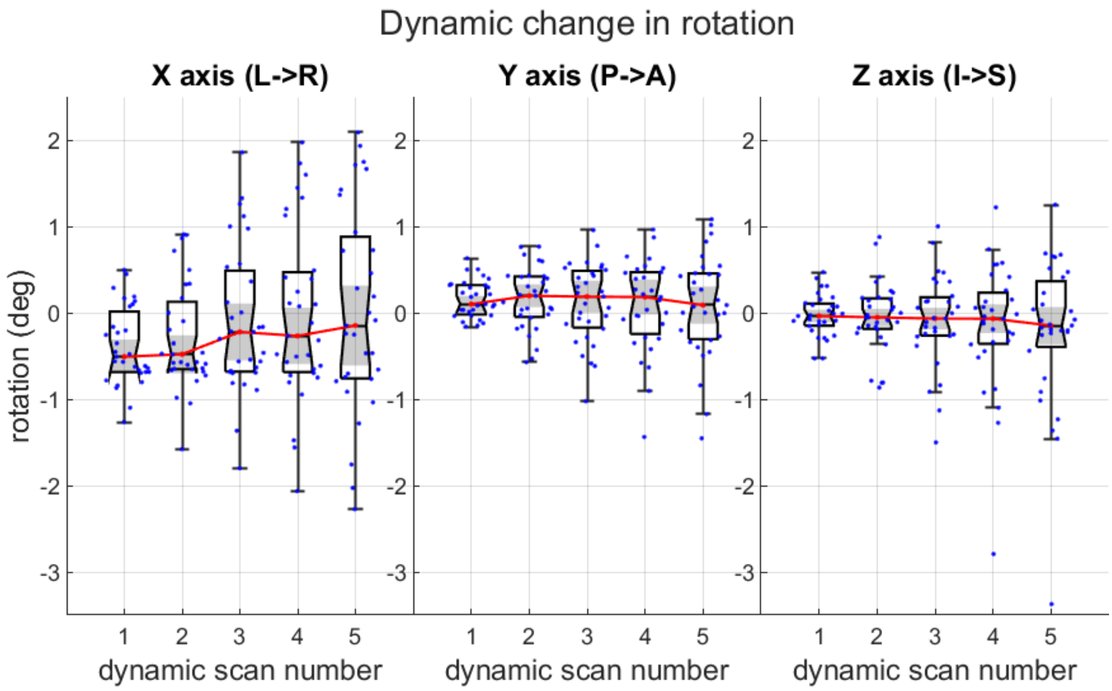

**Figure 3.7:** Dynamic change in rotations about coordinate axes $\theta^x_{1-5}$, $\theta^y_{1-5}$, $\theta^z_{1-5}$.

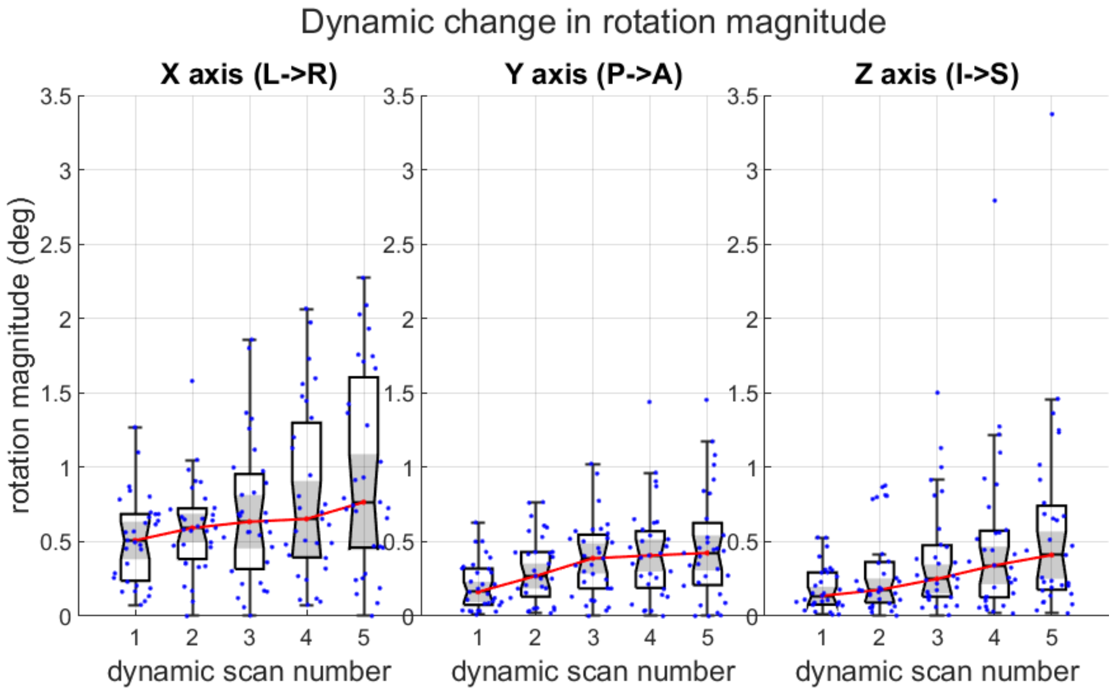

**Figure 3.8:** Dynamic change in magnitudes of rotations about coordinate axes $|\theta^x_{1-5}|$, $|\theta^y_{1-5}|$, $|\theta^z_{1-5}|$.

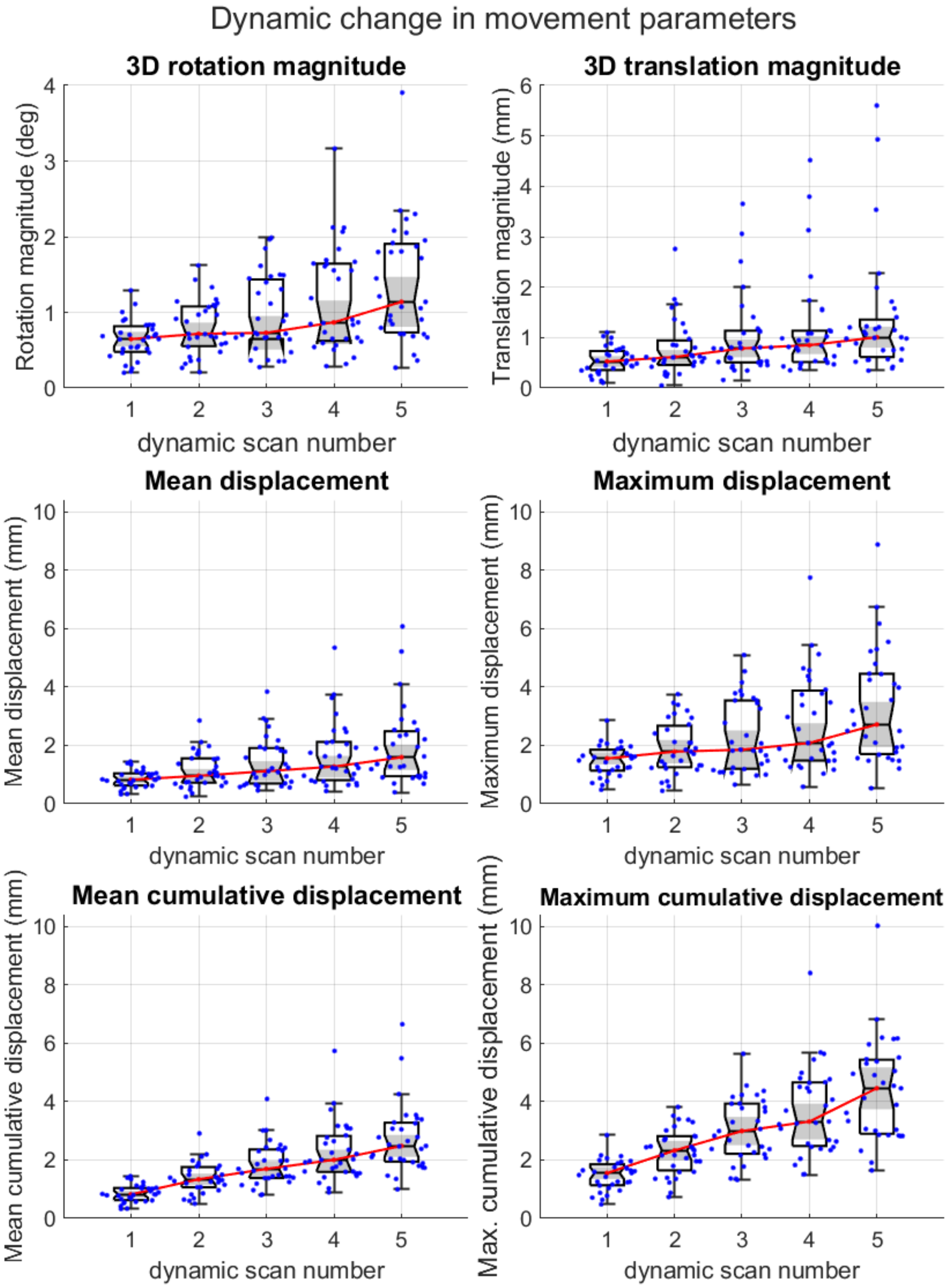

**Figure 3.9:** The dynamic change in translation magnitude ($t_{1-5}$), rotation magnitude ($\theta_{1-5}$), mean and maximum displacement ($d^{mean}_{1-5}$, $d^{max}_{1-5}$), and mean and maximum cumulative displacement ($c^{mean}_{1-5}$, $c^{max}_{1-5}$).

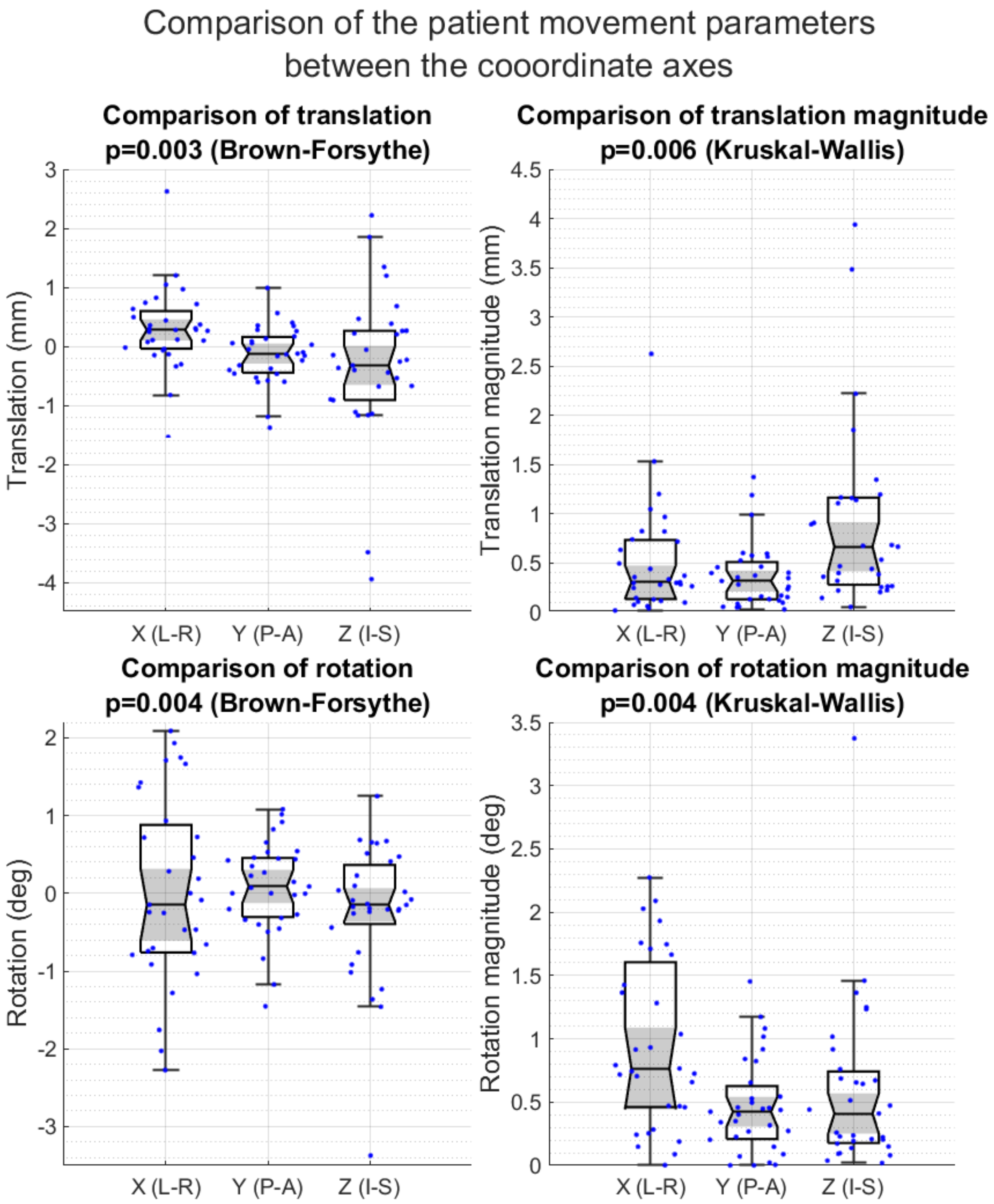

**Figure 3.10:** The comparison of translations $t_5^x$, $t_5^y$, $t_5^z$, translation magnitudes $|t_5^x|$, $|t_5^y|$, $|t_5^z|$, rotations $\theta_5^x$, $\theta_5^y$, $\theta_5^z$ and rotation magnitudes $|\theta_5^x|$, $|\theta_5^y|$, $|\theta_5^z|$ between the coordinate axes.

### 3.3.1 Effect of patient movement on values of estimated FWHM

The effect of patient movement on the estimated FWHM was evaluated using a linear regression model with the mean estimated FWHM as the response variable according to Section 2.4.3. The average estimated FWHM was computed as the mean of radial, tangential and axial estimated FWHM. The maximum cumulative displacement parameter $c_5^{max}$ (2.4.2) was used to assess the effect of patient movement on estimated FWHM because it provided information about the total length of movement trajectory.

The estimated FWHM was modeled with multiple linear regression to test whether the estimated FWHM can be predicted based on the scanner model ($scanner$) and whether patient movement represented by the maximum cumulative displacement ($c_5^{max}$) significantly influences the FWHM estimate. The Siemens Biograph mCT scanner was represented as $scanner = 0$ and Siemens Biograph Vision scanner as $scanner = 1$. The multiple linear regression model was fitted according to 2.4.3.

The fitted model for "highres" reconstruction is described by equation 3.1. The regression was statistically significant ( $p < 0.001$, $RSS = 0.82$) and the scanner model significantly predicted the estimated FWHM ($p < 0.001$). The patient movement $c_5^{max}$ was not a significant predictor of the estimated FWHM ($p > 0.05$).

$$\overline{FWHM} = 3.73 - 0.59 \cdot scanner + 0.02 \cdot c_5^{max} + \epsilon \tag{3.1}$$

The fitted model for "quantitative" reconstruction is described by equation 3.2. The regression was statistically significant ( $p < 0.001$, $RSS = 0.69$) and the scanner model significantly predicted the estimated FWHM ($p < 0.001$). The patient movement $c_5^{max}$ was not a significant predictor of the estimated FWHM ($p > 0.05$).

$$\overline{FWHM} = 5.8 - 0.73 \cdot scanner + 0.03 \cdot c_5^{max} + \epsilon \tag{3.2}$$

The effect of patient movement on estimated FWHM was also evaluated for each PET scanner independently by fitting a simple linear regression model according to 2.4.3. The results of the regressions are visualized in Figure 3.11.

The fitted model for Siemens Biograph mCT scanner is described in equation 3.3 for "highres" reconstruction. The patient movement significantly predicted the estimated FWHM ($p = 0.03$, $RSS = 0.3$).

$$\overline{FWHM} = 3.65 + 0.04 \cdot c_5^{max} + \epsilon \tag{3.3}$$

The fitted model for Siemens Biograph mCT scanner for "quantitative" reconstruction is described in equation 3.4. The patient movement did not significantly predict the estimated FWHM ($p > 0.05$, $RSS$=0.06).

$$\overline{FWHM} = 5.8 + 0.04 \cdot c_5^{max} + \epsilon \tag{3.4}$$

The fitted model for Siemens Biograph Vision scanner with "highres" reconstruction is described in equation 3.5. The patient movement did not significantly predict the estimated FWHM ($p > 0.05$, $RSS = 0.1$).

$$\overline{FWHM} = 3.39 - 0.03 \cdot c_5^{max} + \epsilon \tag{3.5}$$

The fitted model for Siemens Biograph Vision scanner with "quantitative" reconstruction is described in equation 3.6. The patient movement did not significantly predict the estimated FWHM ($p > 0.05$, $RSS = 0.1$).

$$\overline{FWHM} = 5.1 + 0.03 \cdot c_5^{max} + \epsilon \tag{3.6}$$

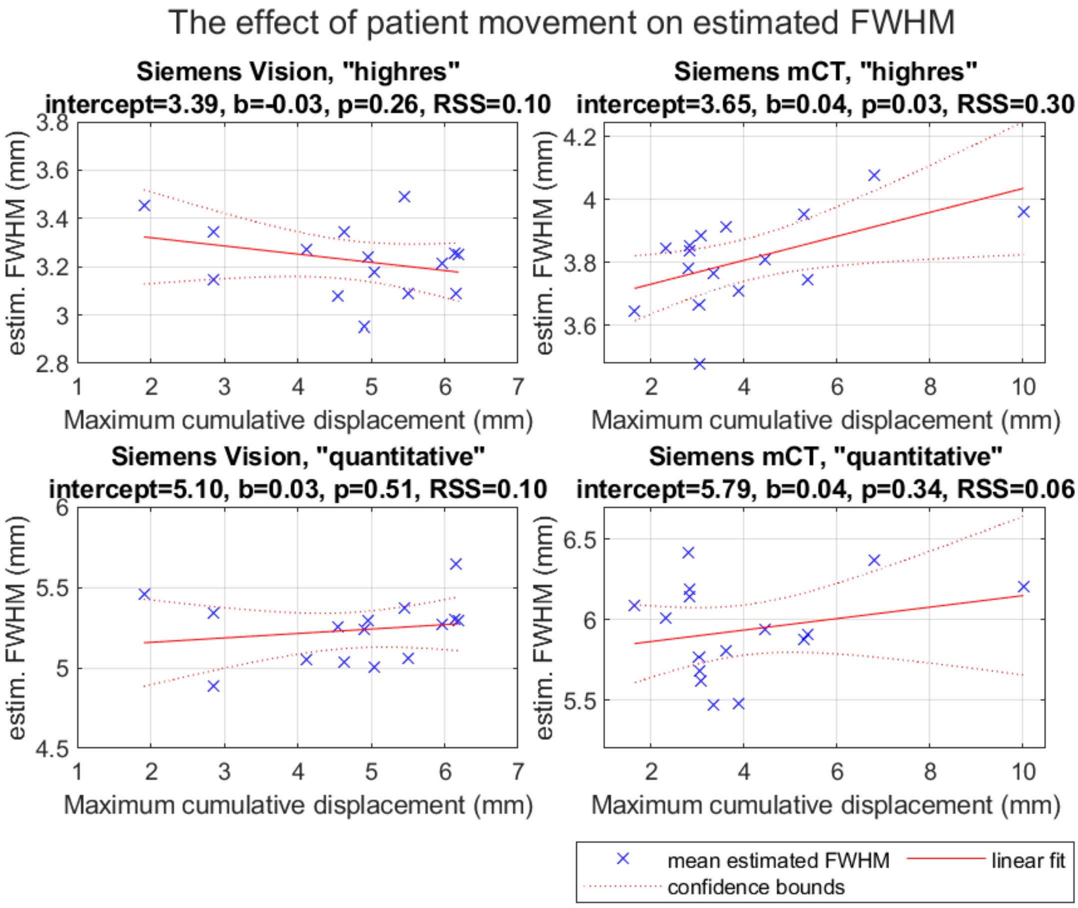

**Figure 3.11:** change in activity

These results indicate that estimated FWHM was mostly predicted by the PET scanner model. The patient movement only slightly affected the estimated values. An effect of patient movement on the estimated FWHM was observed only for Siemens Biograph mCT scanner under "highres" reconstruction.

## 3.4 The effect of FWHM on automatic hypometabolism detection

### 3.4.1 Effect of partial volume correction on effective spatial resolution

The input FWHM influences the values of activity in the resulting pvcPET image. The relative change in activity with respect to the input FWHM value was represented by the mean ratio of metabolic activity in the gray matter ($MRA$) between **pvcPET$^{50\%}$**, **pvcPET$^{100\%}$**, **pvcPET$^{150\%}$**, **pvcPET$^{200\%}$** and **PET** according to Section 2.5.1. The resulting values of $MRA$ are reported in Table 3.6 and visualized in Figure 3.12. In median, the 50% increase of the FWHM estimate resulted in 14% increase in gray matter activity in the pvcPET image.

**Mean relative change in gray matter activity**

| | $MRA^{50\%}$ | $MRA^{100\%}$ | $MRA^{150\%}$ | $MRA^{200\%}$ |
|---|---|---|---|---|
| Median (IQR) | 119 (115-122) % | 135 (127-141) % | 148 (136-156) % | 159 (145-167) % |

**Table 3.6:** The mean relative change in gray matter activity $MRA$ in partial volume corrected PET (pvcPET) images with respect to the original PET image. The median $MRA$ together with interquartile range is reported for each pvcPET image.

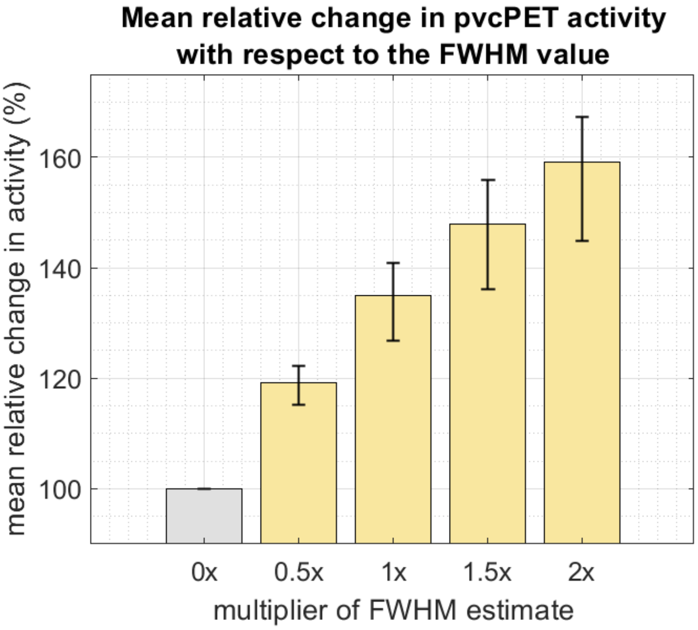

**Figure 3.12:** Visualization of the mean relative change in gray matter activity $MRA$ in partial volume corrected PET (pvcPET) images with respect to the original PET image. FWHM equal to 50, 100, 150, 200 % of the estimated FWHM was used for partial volume correction.

### 3.4.2 Effect of partial volume correction on the hypometabolism detection

The map of hypometabolic voxels was computed for the **PET** image and for each of the pvcPET images **pvcPET**$^{50\%}$, **pvcPET**$^{100\%}$, **pvcPET**$^{150\%}$ and **pvcPET**$^{200\%}$ that were obtained according to Section 2.5.1. For each map of hypometabolic voxels, the detection performance was described using the sensitivity (TPR), specificity (TNR), positive predictive value (PPV), and Matthew's correlation coefficient (MCC) parameters according to Section 2.5.2. The results of detection performance are visualized in Figure 3.13. The detection performance based on **pvcPET**$^{100\%}$ was compared to the detection performance based on the other images using a Friedman test with Tukey-Kramer correction for multiple comparisons. The results of the tests are reported in table 3.7 together with median and interquartile range of the parameters.

| | **Median (IQR), Friedman test, Tukey-Kramer correction** | | | |
|---|---|---|---|---|
| **FWHM** | **TPR** | **TNR** | **PPV** | **MCC** |
| **0** | 0.29 (0.14-0.42)<br>NS | 0.93 (0.91-0.94)<br>$p$=**0.001** | 0.07 (0.02-0.09)<br>$p$<**0.001** | 0.09 (0.04-0.17)<br>$p$<**0.001** |
| **50%** | 0.21 (0.13-0.4)<br>$p$=**0.003** | 0.95 (0.94-0.97)<br>NS | 0.08 (0.040.15)<br>NS | 0.1 (0.05-0.19)<br>$p$=0.08 |
| **100%** | 0.25 (0.15-0.48) | 0.95 (0.94-0.97) | 0.08 (0.05-0.16) | 0.13 (0.07-0.22) |
| **150%** | 0.25 (0.15-0.45)<br>NS | 0.96 (0.94-0.97)<br>$p$=**0.008**; | 0.09 (0.05-0.16)<br>NS | 0.13 (0.07-0.22)<br>NS |
| **200%** | 0.23 (0.13-0.43)<br>$p$=0.06 | 0.96 (0.95-0.97)<br>$p$<**0.001** | 0.09 (0.05-0.17)<br>NS | 0.13 (0.07-0.22)<br>NS |

**Table 3.7:** Comparison of the automatic hypometabolism detection performance with respect to the FWHM that was used for partial volume correction. The detection performance was evaluated for the original PET image and for partial volume corrected PET images (pvcPET) that were obtained with FWHM equal to 50, 100, 150, 200 % of the estimated FWHM. The detection performance based on pvcPET obtained with 100% of the estimated FWHM was compared to the performance based on the other values of FWHM.

There was a trend of increasing $MCC$, $TNR$, and $PPV$ for the input FWHM increasing from 0 to 100 % of the estimated FWHM. The values of $TPR$ were comparable, however, a decrease in $TPR$ was observed for 50% of the FWHM estimate. There was a break point in the increasing trend of $TPR$, $MCC$, and $PPV$ around 100-150 % of the estimated FWHM. From this point, there was a trend of decreasing $TPR$ and increasing $TNR$ for the input FWHM increasing from 100 % to 200 % of the estimated FWHM. $MCC$ and $PPV$ were comparable.

The detection performance was evaluated mainly based on $MCC$. $TPR$ was the second most important parameter for the evaluation, because high sensitivity is preferred and false positive detections can be rejected by the neuroradiologists. All pvcPET images had better detection performance than the original PET image. The best detection performance was achieved for 100% of the FWHM estimate and for 150 % of the FWHM estimate. The results for 100% of the FWHM estimate and for 150 % were comparable, except that there was higher specificity for 150 % of the FWHM estimate.

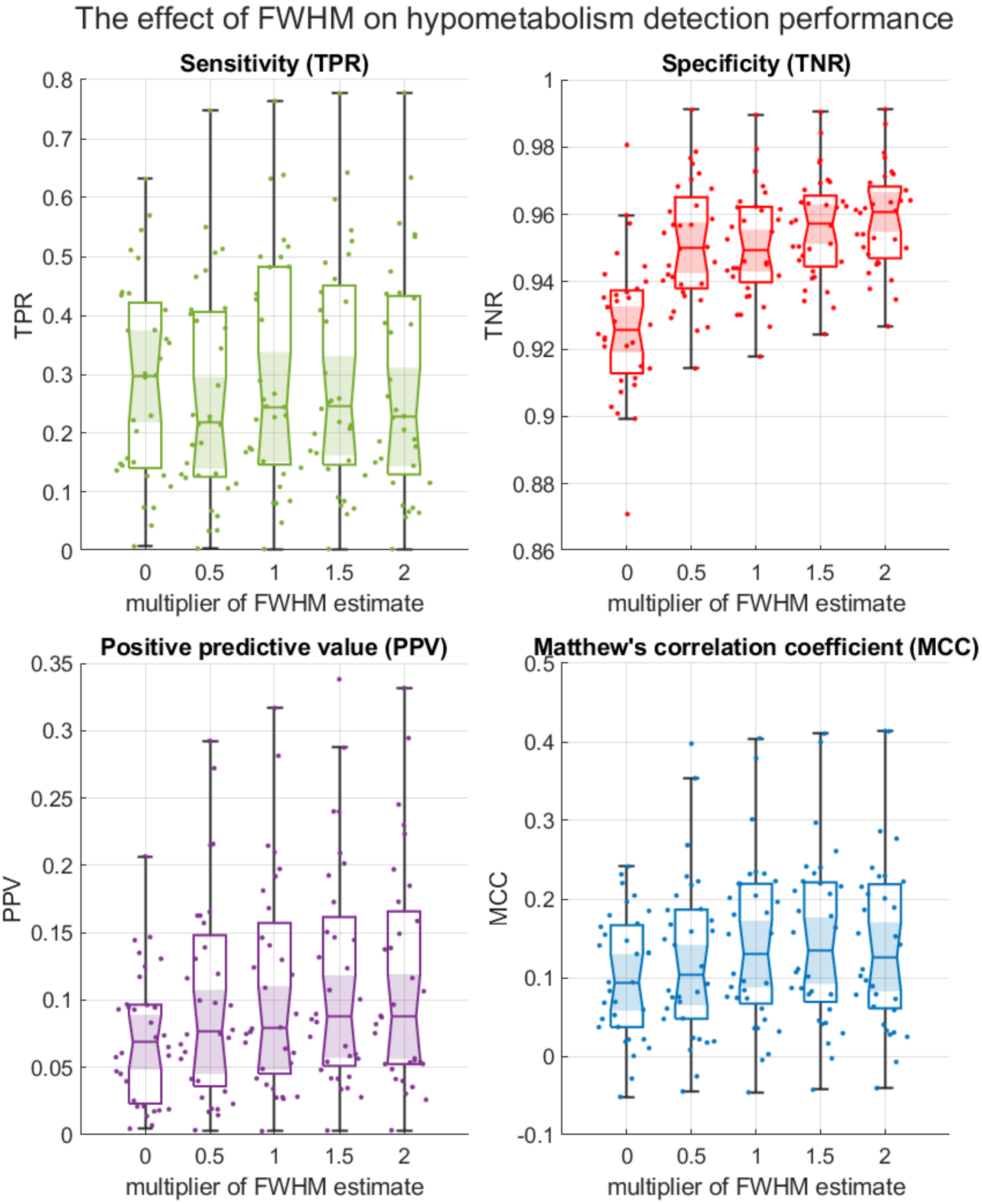

**Figure 3.13:** Visualization of the influence of input FWHM that was used for partial volume correction on the detection performance. The detection performance was evaluated for the original PET image and for partial volume corrected PET images (pvcPET) that were obtained with FWHM equal to 50, 100, 150, 200 % of the estimated FWHM. The detection performance was parameterized by sensitivity, specificity, positive predictive value and Matthew's correlation coefficient with respect to the extent of surgical resection.

# Chapter 4

# Discussion

Precise delineation of the epileptogenic lesion is a key factor that influences the result of the resective surgery in patients with drug-resistant focal epilepsy. The tissue of epileptogenic lesion often shows hypometabolic activity. The low effective resolution is one of the key factors that limit the use of FDG-PET for precise localization of the subtle hypometabolic lesions.

The low effective resolution of PET images can be additionally compensated by partial volume correction which can possibly increase the quality of the PET image for visual and automatic assessment of hypometabolism. Full width at half maximum (FWHM) of the scanner point spread function is one of the important inputs for Müller-Gärtner partial volume correction method. The FWHM specified by the scanner manufacturer is usually used for partial volume correction. However, the specifications of the PET scanner may be difficult to find retrospectively. Moreover, the spatial resolution specified by the manufacturer might not correspond to the spatial resolution achieved under the clinical protocol. Therefore, a new method for fully automatic estimation of FWHM of was proposed in this thesis.

A reference measurement of the scanner PSF was performed under a clinical protocol using a capillary phantom in order to validate the results of the method for automatic FWHM estimation. However, a phantom measurement cannot capture the effect of patient movements on the effective spatial resolution. Therefore, the effect of patient movement on the automatic estimation of FWHM was investigated.

In a previous work, a method for automatic detection of hypometabolic regions in PET images was proposed. The method detects the hypometabolic regions based on partial volume corrected PET images. Therefore, the performance of the method may depend on the parameters of the partial volume correction. The effect of FWHM on the performance of hypometabolism detection was therefore evaluated.

The main goal of this thesis was to investigate the effect of the main input parameter FWHM on results of partial volume correction and automatic hypometabolism detection. This could allow to choose the best setting so that the methods are maximally beneficial for the assessment of PET images in clinical practice.

## 4.1 Reference measurement of scanner effective resolution using a capillary phantom

Effective spatial resolution was measured for Siemens Biograph mCT and Siemens Biograph Vision PET scanners under the same clinical acquisition and reconstruction protocol that was used to examine patients in the control dataset. A capillary phantom of known size and activity was used for the measurement. The reconstruction protocol included two types of OSEM iterative reconstruction, referred to as "highres" and "quantitative".

Measured FWHM was in general higher for "quantitative" reconstruction compared to "highres" reconstruction. This corresponds to the protocol settings. The "highres" reconstruction protocol included correction of the effect of the point spread function which provides higher effective spatial resolution. Conversely, the "quantitative reconstruction included Gaussian smoothing which suppresses the noise but decreases the effective spatial resolution.

Measured FWHM was slightly higher in case of Siemens Biograph mCT scanner compared to the Siemens Biograph Vision scanner. These results correspond to the specifications from the manufacturer that were also slightly higher for the Siemens Biograph mCT scanner.

The tangential resolution was expected to be stable and the radial resolution was expected to increase across the positions of the phantom. This assumption was satisfied only for the Siemens Biograph Vision scanner. This might be caused by the uncertainty of the measurement. It could also be caused by the use of a clinical reconstruction instead of the standard reconstruction. The measurement should be repeated to confirm this observation.

Measured FWHM was in general surprisingly low for the "highres" reconstruction. According to [4], the measured spatial resolution of a point source can be underestimated if the point source image is reconstructed with iterative reconstruction. It has been observed that iterative reconstruction can artificially enhance the apparent spatial resolution if a point source is imaged in air and is reconstructed without any background activity [52]. Results of [4] indicate that the measured FWHM monotonically decreases with increasing contrast between the point source and background. Thus, the low values of measured FWHM could be caused by this property of the iterative reconstruction.

In the future, the reference measurement should be repeated in a setting more suitable for the clinical protocol. According to [4], a low contrast point source should be used when measuring PET scanner resolution with iterative reconstruction. In [24], it is suggested to use a cylinder phantom for the measurement of effective spatial resolution under clinical protocol. The measurement on the cylinder phantom is based on estimation of the edge spread function. This phantom could be therefore suitable for validation of the automatic estimation method that was proposed in this thesis.

## 4.2 Automatic FWHM estimation method

A fully automatic method for estimation of FWHM of the scanner point spread function was proposed. The automatic estimates of FWHM were computed for both the control dataset and the test dataset. The method generally performed as expected and returned reasonable values of FWHM.

The control dataset included PET images that were acquired on the same PET scanners under the same reconstruction protocols as the reference PET images of the capillary phantom. The estimated FWHM values could therefore be compared with the reference FWHM values that were measured using a phantom. For "highres" reconstruction, the automatic FWHM estimates were 12-58 % overestimated compared to the reference. For "quantitative" reconstruction, the automatic FWHM estimates were 11-19 % underestimated compared to the reference. The variance of the FWHM estimates was in general higher for the z (I-S) axis.

The overestimation of FWHM for "highres" reconstruction could be partly caused by inaccuracies in the reference measurement due to the properties of the iterative reconstruction (discussed in more details in 4.1). In general, the FWHM measured using a phantom might not precisely represent the FWHM achieved when imaging a real patient because of the effects as tissue scatter and attenuation, limited number of coincidence events and patient's movement during acquisition [5], [38].

Some errors in the estimation also could have arisen because the assumptions of the method were not completely fulfilled. One of the assumptions was that the border of gray matter can be regarded as an edge that is the main source of activity. The ideal edge is infinitely long. That is not true for the gray matter which is 1-4.5 mm thick [2]. The estimation could also be slightly influenced by the signal from other tissues of the head.

In the future, the method should be further validated using phantom that better represents the characteristics of the brain tissue (e.g. Hoffman phantom [53]).

The test dataset included PET images that were acquired at various clinics using various PET scanners, some of which are of unknown model or are no longer in operation. Therefore, it was not possible to measure the reference FWHM. The FWHM value specified by the manufacturers (if available) had to be considered as an approximate reference. The estimated values of FWHM approximately corresponded to the values specified by manufacturers. A trend of increasing values of estimated FWHM was observed related to the increasing reference effective spatial resolution of the individual PET scanners. However, obviously incorrect FWHM was obtained in two cases. In both cases, the size of the voxel in the corresponding axis exceeded 4 mm.

This suggests that the method can fail for images with large voxel sizes. It is probably caused by insufficient sampling of the edge profile of the cortex border. If the sampling is too low, the edge profile cannot be precisely fitted by normal cumulative distribution function. Therefore, the FWHM of the edge spread function is incorrectly estimated. This effect could also explain higher variance of the estimates in the $z$ (I-S) axis. The sampling in the $z$ axis is in general lower compared to $x$ (L-R) and $y$ (P-A) axis which could cause larger inaccuracies in the $z$ axis.

In the future, the effect of voxels size on the performance of the method should be investigated and the method should be modified to work correctly for all images.

## 4.3 Quantification of patient movement during acquisition

The movement of the patient in the scanner during the acquisition of the PET scan influences the effective spatial resolution of the resulting PET image [5], [29], [30]. In clinical practice, patient movement is not routinely quantified and is rather visually evaluated. Therefore, the movement of the head was measured and quantified for patients from the control dataset. The control dataset included the dynamic PET sequences. Therefore, it was possible to measure the dynamic change in patient movement depending on the time spent in the PET scanner. The effect of measured patient movement on the method for automatic FWHM estimation was evaluated.

The results indicate that patients typically moved steadily in the scanner and the movement increased with time spent in the scanner. The measured translation of the head was in the range of 0.3-5.6 mm and the measured rotation was in the range of 0.3-3.9°. A translation of the head in range of 1-12 mm and rotation in range of 0.2-4.1 ∘ was reported across the publications [5], [29], [33], [34]. This indicate that the translation of the head of the patients who were examined in the PET Center of the Na Homolce Hospital is lower compared to the standard. The patients typically rotated their chin up or down ("nodding" movement) around the $x$ axis and shifted their head up or down towards their feet in the $z$ axis. The dominant shift in $z$ axis is also reported in [5], [29], [54] and [5], [29] reported a dominant rotation around $x$ axis.

The effect of patient movement on the estimated FWHM was evaluated for both PET scanners Siemens Biograph mCT and Siemens Biograph Vision and for both "highres" and "quantitative" reconstruction. The estimated FWHM significantly increased with larger patient movement only for the Siemens Biograph mCT scanner under "highres" reconstruction. There was no observable effect under the "quantitative" reconstruction. The effect of patient movement on the estimated FWHM was generally smaller then expected.

This could be because the movement was not large enough to affect the effective spatial resolution of the PET images. Also it could be explained by a wrong assumption about the process of reconstruction of PET images from the control dataset. The PET images were reconstructed in the PET Center of the Na Homolce Hospital. The radiologists routinely visually assess if the patient has moved during the acquisition. The time intervals when the patient was moving are then excluded from the reconstruction. It was assumed that this modification of reconstruction is always specified in the metadata of the PET image. However, this assumption may not have been fulfilled. Therefore, the negative effect of patient movement on the PET images could have been successfully limited by this modification of reconstruction.

The effect of patient movement on estimated FWHM should be further investigated. The effect of the modification of the reconstruction should also be incorporated into the evaluation.

## 4.4 The effect of FWHM on automatic hypometabolism detection

The results of partial volume correction are influenced by input parameter FWHM. The method for automatic hypometabolism detection detects the hypometabolic regions based on partial volume corrected PET images (pvcPET) [6]. Therefore, the input FWHM can possibly influence the result of automatic hypometabolism detection.

The Test dataset included a map of delineated extent of resection for each patient. Therefore, it was possible to evaluate the effect of input FWHM on partial volume correction and on the automatic hypometabolism detection. The FWHM was estimated for PET images of patients from the Test dataset. Partial volume correction of the PET images was computed with input FWHM of 50 %, 100 %, 150 % and 200 % of the FWHM estimate. Resulting pvcPET images were used to evaluate the effect of FWHM on partial volume correction and hypometabolism detection.

The detection performance was evaluated based on the overlap of hypometabolic regions with the extent of surgical resection. The results indicate that if the FWHM is underestimated, the detection is less specific and many voxels out of resection are labeled as hypometabolic. This may lead to false detection of epileptogenic hypometabolic regions. This effect is probably caused by insufficient partial volume correction. Inversely, if the FWHM is overestimated the specificity of the detection increases, but at the cost of lower sensitivity. In this case, there are fewer voxels that are correctly labeled as hypometabolic. This trend could be due to excessive partial volume correction. If the activity of gray matter is overcompensated, there is fewer regions that have significantly decreased activity. This may lead to overlooking the true hypometabolic regions.

However, there was a wide range of input FWHM values that produced a good detection result. All pvcPET images showed better detection performance than the original PET image. This indicates that the detection performance is not critically dependent on the precise FWHM used for partial volume correction. The best detection performance was achieved for 100% of the FWHM estimate and for 150 % of the FWHM estimate. The results for 100% of the FWHM estimate and for 150 % were comparable, except that there was higher specificity for 150 % of the FWHM estimate. These results indicate that the automatically estimated values of FWHM are in general a good choice for partial volume correction and automatic hypometabolism detection. The imprecision in the automatically estimated FWHM do not significantly affect the detection performance. However, higher specificity for 150 % of the FWHM estimate suggests that the automatic FWHM estimates might be slightly underestimated.

## 4.5 Outlooks and clinical implications

The movement of the head was measured and quantified for patients from the control dataset. The patients typically rotated their chin up or down ("nodding" movement) and shifted their head up or down towards their feet. The translation of the head of the patients who were examined in the PET Center of the Na Homolce Hospital was lower compared to the standard. In practice, it is very difficult to completely limit the patient's movement. Several techniques to limit patient movement during acquisition are used in the PET center of the Na Homolce Hospital. A head restraint is routinely used to limit the patient movement. The patient lies still and relaxes a few minutes before the examination in order to prevent sudden movements during the acquisition. However, these precautions cannot fully prevent the movement. Therefore, the radiologists routinely visually assess if the patient has moved during the acquisition. The time intervals when the patient was moving are then excluded from the reconstruction.

This technique cannot fully limit the large and continuous movement that occurs during the entire acquisition. Therefore, a method for patient movement correction will be implemented based on dynamic PET images in the future [29], [55]. The method might help to limit the negative effects of patient movement in the cases where the other precautions were insufficient. A new combined MRI-PET scanner should be soon available in the PET center of the Na Homolce Hospital. Thanks to this, movement correction from the manufacturer could be incorporated directly in the reconstruction.

The effect of input FWHM on method for automatic hypometabolism detection was evaluated. The results indicate that the detection performance is not critically dependent on the precise FWHM used for partial volume correction. FWHM values specified by the manufacturer or automatically estimated values of FWHM are in general a good choice for partial volume correction and automatic hypometabolism detection in clinical practice.

These results will allow to focus on the further development of the hypometabolism detection method. Other methods of partial volume correction [44] and their effect on hypometabolism detection will be tested. Alternative approaches to parametrization of hypometabolic regions will be investigated. As part of the ongoing project, a dataset of PET brain images from controls without epilepsy will be collected. This could allow to incorporate the comparison with the control group into the method for automatic hypometabolism detection [17], [19].

# Chapter 5

# Conclusion

All of the tasks of the thesis were successfully completed. A new method for fully automatic estimation of FWHM of the scanner point spread function was proposed. A reference measurement of the scanner PSF was performed under a clinical protocol using a capillary phantom to validate the results of the method for automatic FWHM estimation. The method generally performed as expected and returned reasonable values of FWHM. The patient movements that occurred during the acquisition of PET images were measured and quantified. The patients typically rotated their chin up or down and shifted their head up or down towards their feet. The effect of patient movement on the automatic estimation of FWHM was investigated. Patient movements only slightly affected the FWHM estimation. The effect of FWHM on the performance of hypometabolism detection was evaluated. The detection performance was not critically dependent on the precise FWHM used for partial volume correction. FWHM values specified by the manufacturer or automatically estimated values of FWHM are in general a good choice for partial volume correction and automatic hypometabolism detection.

# Bibliography

[1] M. Brázdil, J. Hadač, and P. Marusič, *Farmakorezistentní epilepsie*. Praha: Triton, 2011, ISBN: 978-80-7387-495-7.

[2] K. Goffin, W. Van Paesschen, P. Dupont, *et al.*, "Anatomy-based reconstruction of FDG-PET images with implicit partial volume correction improves detection of hypometabolic regions in patients with epilepsy due to focal cortical dysplasia diagnosed on MRI", *European Journal of Nuclear Medicine and Molecular Imaging*, vol. 37, no. 6, pp. 1148–1155, 2010, ISSN: 16197070. DOI: `10.1007/s00259-010-1405-5`.

[3] K. Erlandsson, I. Buvat, P. H. Pretorius, B. A. Thomas, and B. F. Hutton, "A review of partial volume correction techniques for emission tomography and their applications in neurology, cardiology and oncology", *Physics in Medicine and Biology*, vol. 57, no. 21, 2012, ISSN: 00319155. DOI: `10.1088/0031-9155/57/21/R119`.

[4] K. Gong, S. R. Cherry, and J. Qi, "On the assessment of spatial resolution of PET systems with iterative image reconstruction", *Physics in Medicine and Biology*, vol. 61, no. 5, N193–N202, 2016, ISSN: 13616560. DOI: `10.1088/0031-9155/61/5/N193`. [Online]. Available: `http://dx.doi.org/10.1088/0031-9155/61/5/N193`.

[5] H. Herzog, L. Tellmann, R. Fulton, *et al.*, "Motion artifact reduction on parametric PET images of neuroreceptor binding", *Journal of Nuclear Medicine*, vol. 46, no. 6, pp. 1059–1065, 2005, ISSN: 01615505.

[6] K. Macková, "Hodnocení hypometabolismu v obrazech pozitronové emisní tomografie Assessment of hypometabolism in positron emission tomography", bachelor thesis, Czech Technical University in Prague, 2021.

[7] A. Shukla and U. Kumar, "Positron emission tomography: An overview", *Journal of Medical Physics*, vol. 31, no. 1, pp. 13–21, 2006, ISSN: 09716203. DOI: `10.4103/0971-6203.25665`. [Online]. Available: `/pmc/articles/PMC3003889/%20/pmc/articles/PMC3003889/?report=abstract%20https://www.ncbi.nlm.nih.gov/pmc/articles/PMC3003889/`.

[8] G. Currie, J. Hewis, and S. Bushong, "Tomographic Reconstruction: A Nonmathematical Overview", *Journal of Medical Imaging and Radiation Sciences*, vol. 46, no. 4, pp. 403–412, 2015, ISSN: 18767982. DOI: `10.1016/j.jmir.2015.07.007`.

[9] P. J. Markiewicz, K. Thielemans, J. M. Schott, *et al.*, "Rapid processing of PET list-mode data for efficient uncertainty estimation and data analysis", *Physics in Medicine and Biology*, vol. 61, no. 13, N322–N336, 2016, ISSN: 13616560. DOI: `10.1088/0031-9155/61/13/N322`.

[10] A. Konik, T. Koesters, M. T. Madsen, and J. J. Sunderland, "Evaluation of attenuation and scatter correction requirements as a function of object size in small animal PET imaging", *IEEE Transactions on Nuclear Science*, vol. 58, no. 5 PART 1, pp. 2308–2314, 2011, ISSN: 00189499. DOI: `10.1109/TNS.2011.2160998`. [Online]. Available: `https://www.researchgate.net/publication/47353137%7B%5C_%7DEvaluation%7B%5C_%7Dof%7B%5C_%7Dattenuation%7B%5C_%7Dand%7B%5C_%7Dscatter%7B%5C_%7Dcorrection%7B%5C_%7Drequirements%7B%5C_%7Din%7B%5C_%7Dsmall%7B%5C_%7Danimal%7B%5C_%7DPET%7B%5C_%7Dand%7B%5C_%7DSPECT%7B%5C_%7Dimaging`.

[11] Y.-S. Bae, H.-C. Kang, H. D. Kim, and S. H. Kim, "New Classification of Focal Cortical Dysplasia: Application to Practical Diagnosis", *Journal of Epilepsy Research*, vol. 2, no. 2, pp. 38–42, 2012, ISSN: 2233-6249. DOI: `10.14581/jer.12010`.

[12] R. Janca, M. Tomasek, A. Kalina, P. Marusic, P. Krsek, and R. Lesko, "Automated Identification of Stereoelectroencephalography Contacts and Measurement of Factors Influencing Accuracy of Frame Stereotaxy (pre-print)", *IEEE Journal of Biomedical and Health Informatics*, vol. PP, no. X, pp. 1–10, 2023. DOI: `10.1109/JBHI.2023.3271857`. [Online]. Available: `https://github.com/EpiReC-ISARG/SEEG-contact-detection-and-skull-measurement`.

[13] S. M. Sisodiya, S. Fauser, J. H. Cross, and M. Thom, "Focal cortical dysplasia type II: biological features and clinical perspectives", *The Lancet Neurology*, vol. 8, no. 9, pp. 830–843, 2009, ISSN: 14744422. DOI: `10.1016/S1474-4422(09)70201-7`. [Online]. Available: `http://dx.doi.org/10.1016/S1474-4422(09)70201-7`.

[14] R. Guerrini, M. Duchowny, P. Jayakar, *et al.*, "Diagnostic methods and treatment options for focal cortical dysplasia", *Epilepsia*, vol. 56, no. 11, pp. 1669–1686, 2015, ISSN: 15281167. DOI: `10.1111/epi.13200`.

[15] B. Gok, G. Jallo, R. Hayeri, and R. Wahl, "The evaluation of FDG-PET imaging for epileptogenic focus localization in patients with MRI positive and MRI negative temporal lobe epilepsy", pp. 541–550, 2013. DOI: `10.1007/s00234-012-1121-x`.

[16] F. Archambaud, V. Bouilleret, L. Hertz-Pannier, *et al.*, "Optimizing statistical parametric mapping analysis of 18F-FDG PET in children", *EJNMMI Research*, vol. 3, no. 1, pp. 1–10, 2013, ISSN: 2191219X. DOI: `10.1186/2191-219X-3-2`. [Online]. Available: `EJNMMI%20Research`.

[17] J. Tomás, F. Pittau, A. Hammers, *et al.*, "The predictive value of hypometabolism in focal epilepsy: a prospective study in surgical candidates", *European Journal of Nuclear Medicine and Molecular Imaging*, vol. 46, no. 9, pp. 1806–1816, 2019, ISSN: 16197089. DOI: `10.1007/s00259-019-04356-x`.

[18] Y. K. Kim, D. S. Lee, S. K. Lee, C. K. Chung, J. K. Chung, and M. C. Lee, "18F-FDG PET in localization of frontal lobe epilepsy: Comparison of visual and SPM analysis", *Journal of Nuclear Medicine*, vol. 43, no. 9, pp. 1167–1174, 2002, ISSN: 01615505.

[19] P. Van Bogaert, N. Massager, P. Tugendhaft, *et al.*, "Statistical parametric mapping of regional glucose metabolism in mesial temporal lobe epilepsy", *NeuroImage*, vol. 12, no. 2, pp. 129–138, 2000, ISSN: 10538119. DOI: `10.1006/nimg.2000.0606`.

[20] K. Shang, J. Wang, X. Fan, *et al.*, "Clinical value of hybrid TOF-PET/MR imaging-based multiparametric imaging in localizing seizure focus in patients with MRI-negative temporal lobe epilepsy", *American Journal of Neuroradiology*, vol. 39, no. 10, pp. 1791–1798, 2018, ISSN: 1936959X. DOI: `10.3174/ajnr.A5814`.

[21] K. K. Yu, S. L. Dong, K. L. Sang, *et al.*, "Differential features of metabolic abnormalities between medial and lateral temporal lobe epilepsy: Quantitative analysis of 18F-FDG PET using SPM", *Journal of Nuclear Medicine*, vol. 44, no. 7, pp. 1006–1012, 2003, ISSN: 01615505.

[22] S. Lagarde, M. Boucekine, A. McGonigal, *et al.*, "Relationship between PET metabolism and SEEG epileptogenicity in focal lesional epilepsy", *European Journal of Nuclear Medicine and Molecular Imaging*, vol. 47, no. 13, pp. 3130–3142, 2020, ISSN: 16197089. DOI: `10.1007/s00259-020-04791-1`.

[23] I. Boscolo Galazzo, M. V. Mattoli, F. B. Pizzini, *et al.*, "Cerebral metabolism and perfusion in MR-negative individuals with refractory focal epilepsy assessed by simultaneous acquisition of 18F-FDG PET and arterial spin labeling", *NeuroImage: Clinical*, vol. 11, pp. 648–657, 2016, ISSN: 22131582. DOI: `10.1016/j.nicl.2016.04.005`. [Online]. Available: `http://dx.doi.org/10.1016/j.nicl.2016.04.005`.

[24] M. A. Lodge, J. P. Leal, A. Rahmim, J. J. Sunderland, and E. C. Frey, "Measuring PET Spatial Resolution Using a Cylinder Phantom Positioned at an Oblique Angle", *J Nucl Med*, vol. 59, pp. 1768–1775, 2018. DOI: `10.2967/jnumed.118.209593`.

[25] Siemens Medical Solutions USA, "Inside Biograph TruePoint PET-CT", 2009. [Online]. Available: `https://www.siemens-healthineers.com/siemens%7B%5C_%7Dhwem-hwem%7B%5C_%7Dssxa%7B%5C_%7Dwebsites-context-root/wcm/idc/groups/public/@global/@imaging/@molecular/documents/download/mdaw/mtuz/%7B~%7Dedisp/btruep%7B%5C_%7Dtechnology%7B%5C_%7Dinsert-00046599.p`.

[26] B. Lukáš Macháček and M. Miroslav Špaček, "Využití metody FDG-PET/CT k diagnostice infekce cévní protézy v aorto-ilické oblasti", Diplomová práce, Univerzita Karlova, Praha, 2010. [Online]. Available: `https://dspace.cuni.cz/handle/20.500.11956/35062`.

[27] Y. Chen and H. An, "Attenuation Correction of PET/MR Imaging", *Magnetic Resonance Imaging Clinics of North America*, vol. 25, no. 2, pp. 245–255, 2017, ISSN: 1064-9689. DOI: `https://doi.org/10.1016/j.mric.2016.12.001`. [Online]. Available: `https://www.sciencedirect.com/science/article/pii/S1064968916301167`.

[28] D. S. Lalush, "Magnetic Resonance–Derived Improvements in PET Imaging", *Magnetic Resonance Imaging Clinics of North America*, vol. 25, no. 2, pp. 257–272, 2017, ISSN: 15579786. DOI: `10.1016/j.mric.2016.12.002`. [Online]. Available: `http://dx.doi.org/10.1016/j.mric.2016.12.002`.

[29] Y. Ikari, T. Nishio, Y. Makishi, *et al.*, “Head motion evaluation and correction for PET scans with 18F-FDG in the Japanese Alzheimer’s disease neuroimaging initiative (J-ADNI) multi-center study”, *Annals of Nuclear Medicine*, vol. 26, no. 7, pp. 535–544, 2012, ISSN: 09147187. DOI: `10.1007/s12149-012-0605-4`.

[30] Y. Zhu and X. Zhu, “MRI-driven PET image optimization for neurological applications”, *Frontiers in Genetics*, vol. 10, no. JUL, pp. 1–15, 2019, ISSN: 16648021. DOI: `10.3389/fnins.2019.00782`.

[31] B. F. Hutton, A. Z. Kyme, Y. H. Lau, D. W. Skerrett, and R. R. Fulton, “A hybrid 3-D reconstruction/registration algorithm for correction of head motion in emission tomography”, *IEEE Transactions on Nuclear Science*, vol. 49, no. 1 I, pp. 188–194, 2002, ISSN: 00189499. DOI: `10.1109/TNS.2002.998750`.

[32] M. Menke, M. S. Atkins, and K. R. Buckley, “Compensation methods for head motion detected during pet imaging”, *IEEE Transactions on Nuclear Science*, vol. 43, no. 1 PART 2, pp. 310–317, 1996, ISSN: 00189499. DOI: `10.1109/23.485971`.

[33] U. E. Ruttimann, P. J. Andreason, and D. Rio, “Head motion during positron emission tomography: is it significant?”, *Psychiatry Research: Neuroimaging*, vol. 61, no. 1, pp. 43–51, 1995, ISSN: 09254927. DOI: `10.1016/0925-4927(95)02565-F`.

[34] A. Wagner, K. Schicho, F. Kainberger, W. Birkfellner, S. Grampp, and R. Ewers, “Quantification and Clinical Relevance of Head Motion during Computed Tomography”, *Investigative Radiology*, vol. 38, no. 11, pp. 733–741, 2003, ISSN: 00209996. DOI: `10.1097/01.rli.0000084889.92250.b0`.

[35] J. van den Hoff and J. Langner, *Motion Compensation in Emission Tomography*. Springer, Berlin, Heidelberg, 2012, ISBN: 978-3-642-13270-4. DOI: `10.1007/978-3-642-13271-1_40`.

[36] Y. Picard and C. J. Thompson, “Motion correction of PET images using multiple acquisition frames”, *IEEE Transactions on Medical Imaging*, vol. 16, no. 2, pp. 137–144, 1997, ISSN: 02780062. DOI: `10.1109/42.563659`.

[37] *From simultaneous to synergistic PET-MR*, 2021. [Online]. Available: `https://www.siemens-healthineers.com/magnetic-resonance-imaging/mr-pet-scanner/biograph-mmr`.

[38] Rosslyn: National Electrical Manufacturers Association, *NEMA Standards Publication NU 2-2018 Performance Measurements of Positron Emission Tomographs (PETS)*, 2018. [Online]. Available: `www.nema.org%20https://www.nema.org/standards/view/Performance-Measurements-of-Positron-Emission-Tomographs`.

[39] M. V. Green, H. G. Ostrow, J. Seidel, and M. G. Pomper, “Experimental evaluation of depth-of-interaction correction in a small-animal positron emission tomography scanner”, *Molecular Imaging*, vol. 9, no. 6, pp. 311–318, 2010, ISSN: 15353508. DOI: `10.2310/7290.2010.00038`.

[40] M. E. Daube-Witherspoon, J. S. Karp, M. E. Casey, *et al.*, “PET Performance Measurements Using the NEMA NU 2-2001 Standard”, *J Nucl Med*, vol. 43, pp. 1398–1409, 2002. [Online]. Available: `www.nema.org`.

[41] T. R. DeGrado, T. G. Turkington, J. J. Williams, C. W. Stearns, J. M. Hoffman, and R. E. Coleman, “Performance characteristics of a whole-body PET scanner”, *Journal of Nuclear Medicine*, vol. 35, no. 8, pp. 1398–1406, 1994, ISSN: 01615505.

[42] W. W. Moses, “Fundamental Limits of Spatial Resolution in PET”, *Nucl Instrum Methods Phys Res A* ., pp. 236–240, 2010. DOI: `10.1016/j.nima`.

[43] B. Fischl and A. M. Dale, “Measuring the thickness of the human cerebral cortex”, *NeuroImage*, vol. 9, no. 6 PART II, 1999, ISSN: 10538119.

[44] B. A. Thomas, V. Cuplov, A. Bousse, *et al.*, “PETPVC: A toolbox for performing partial volume correction techniques in positron emission tomography”, *Physics in Medicine and Biology*, vol. 61, no. 22, pp. 7975–7993, 2016, ISSN: 13616560. DOI: `10.1088/0031-9155/61/22/7975`.

[45] H. Sari, K. Erlandsson, I. Law, *et al.*, “Estimation of an image derived input function with MR-defined carotid arteries in FDG-PET human studies using a novel partial volume correction method”, *Journal of Cerebral Blood Flow and Metabolism*, vol. 37, no. 4, pp. 1398–1409, 2017, ISSN: 15597016. DOI: `10.1177/0271678X16656197`. [Online]. Available: `https://doi.org/10.1177/0271678X16656197`.

[46] H. W. Müller-Gärtner, J. M. Links, J. L. Prince, *et al.*, “Measurement of radiotracer concentration in brain gray matter using positron emission tomography: MRI-based correction for partial volume effects”, *Journal of Cerebral Blood Flow and Metabolism*, vol. 12, no. 4, pp. 571–583, 1992, ISSN: 0271678X. DOI: `10.1038/jcbfm.1992.81`.

[47] X. Li, M. Zhang, P. Huang, W. Liu, and Q. Huang, “An investigation into the impact of partial volume correction on detection rate of epilepsy using 18F-FDG PET”, in *BIBE 2019; The Third International Conference on Biological Information and Biomedical Engineering*, 2019, pp. 1–5.

[48] C. Comtat, F. Bataille, C. Michel, *et al.*, “OSEM-3D reconstruction strategies for the ECAT HRRT”, *IEEE Nuclear Science Symposium Conference Record*, vol. 6, no. 3, pp. 3492–3496, 2004, ISSN: 10957863. DOI: `10.1109/nssmic.2004.1466639`.

[49] K. A. Kaphingst, S. Persky, and C. Lachance, “Brain: Normal Variations and Benign Findings in FDG PET/CT imaging”, *PET clin.*, vol. 14, no. 4, pp. 384–399, 2010, ISSN: 15378276. DOI: `10.1016/j.cpet.2013.10.006.Brain`. arXiv: `NIHMS150003`.

[50] G. Gonzalez-Escamilla, C. Lange, S. Teipel, R. Buchert, and M. J. Grothe, “PETPVE12: an SPM toolbox for Partial Volume Effects correction in brain PET – Application to amyloid imaging with AV45-PET”, *NeuroImage*, vol. 147, pp. 669–677, Feb. 2017, ISSN: 10959572. DOI: `10.1016/j.neuroimage.2016.12.077`.

[51] D. Chicco and G. Jurman, “The advantages of the Matthews correlation coefficient (MCC) over F1 score and accuracy in binary classification evaluation”, *BMC Genomics*, 2020. DOI: `10.1186/s12864-019-6413-7`. [Online]. Available: `https://doi.org/10.1186/s12864-019-6413-7`.

[52] Y. Yang, Y. C. Tai, S. Siegel, *et al.*, "Optimization and performance evaluation of the microPET II scanner for in vivo small-animal imaging", *Physics in Medicine and Biology*, vol. 49, no. 12, pp. 2527–2545, 2004, ISSN: 00319155. DOI: `10.1088/0031-9155/49/12/005`.

[53] E. J. Hoffman, P. D. Cutler, W. M. Digby, and J. C. Mazziotta, "3-D phantom to simulate cerebral blood flow and metabolic images for PET", *IEEE Transactions on Nuclear Science*, vol. 37, no. 2, pp. 616–620, 1990, ISSN: 15581578. DOI: `10.1109/23.106686`.

[54] L. Tellmann, R. Fulton, U. Pietrzyk, *et al.*, "Concepts of registration and correction of head motion in positron emission tomography", *Zeitschrift fur Medizinische Physik*, vol. 16, no. 1, pp. 67–74, 2006, ISSN: 09393889. DOI: `10.1078/0939-3889-00293`. [Online]. Available: `http://dx.doi.org/10.1078/0939-3889-00293`.

[55] J. E. Mourik, M. Lubberink, F. H. Van Velden, A. A. Lammertsma, and R. Boellaard, "Off-line motion correction methods for multi-frame PET data", *European Journal of Nuclear Medicine and Molecular Imaging*, vol. 36, no. 12, pp. 2002–2013, 2009, ISSN: 16197070. DOI: `10.1007/s00259-009-1193-y`.

# Appendix A

# Appendix

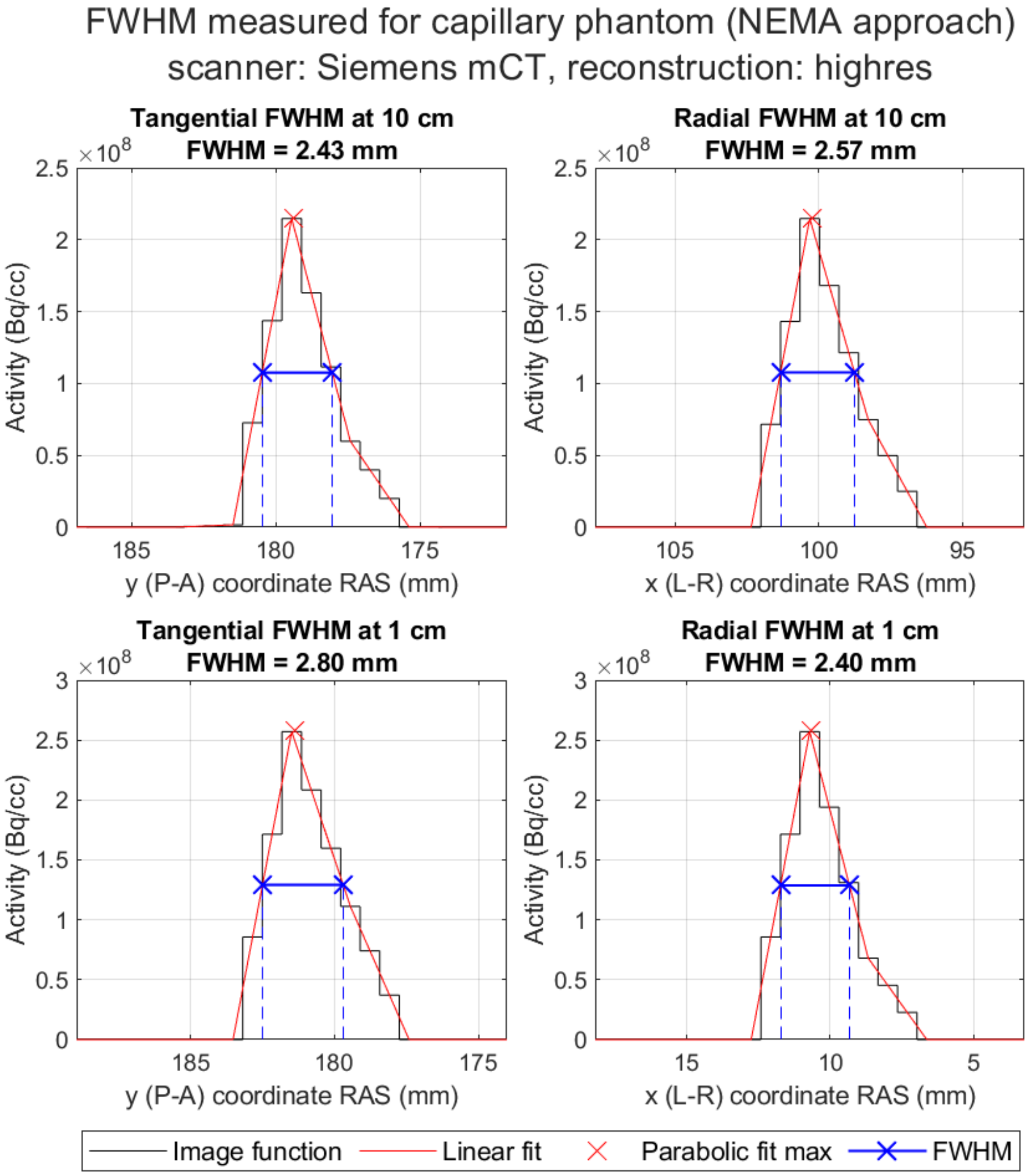

**Figure A.1:** Reference FWHM measured on the Siemens Biograph mCT scanner under "highres" reconstruction protocol.

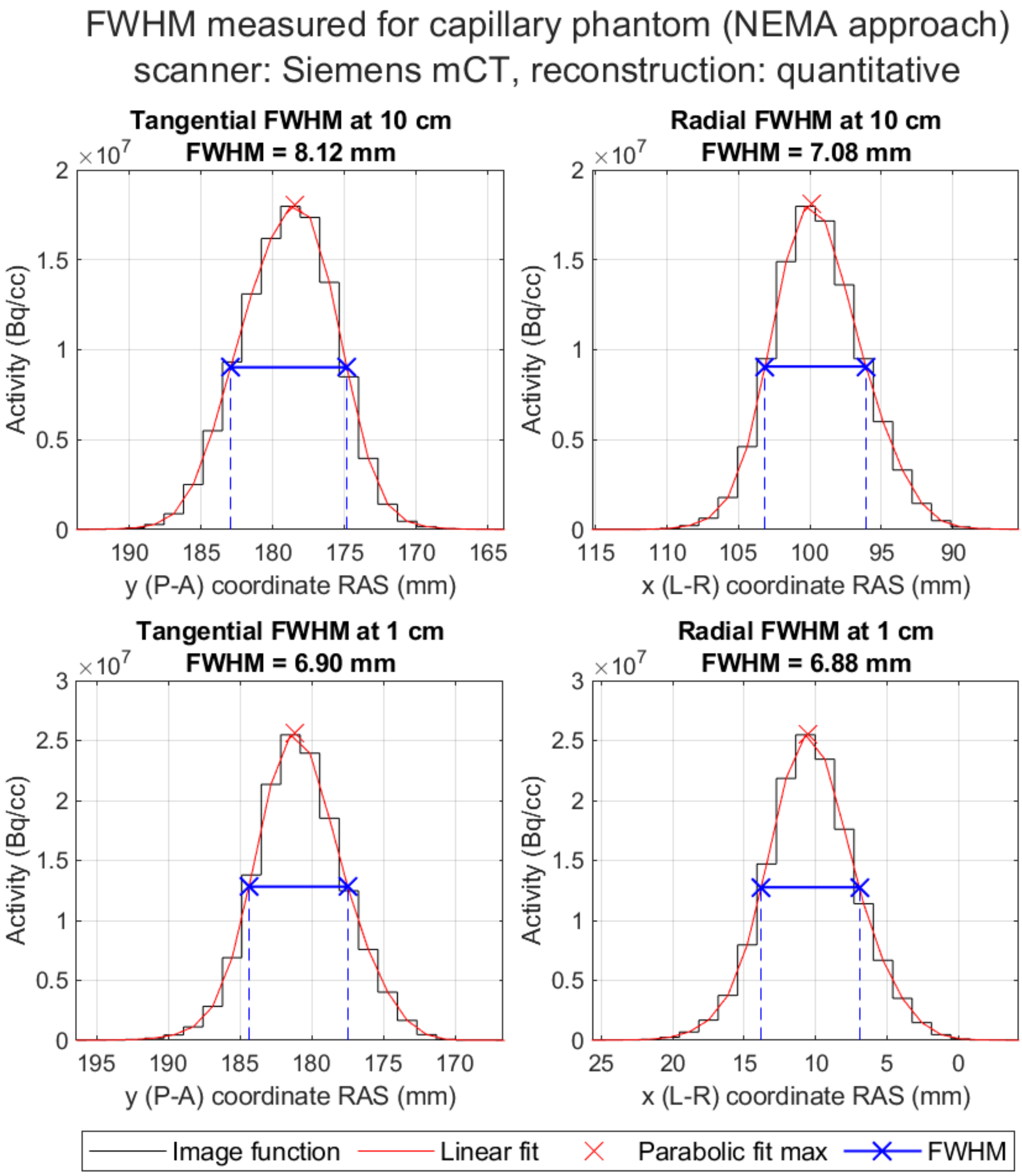

**Figure A.2:** Reference FWHM measured on the Siemens Biograph mCT scanner under "quantitative" reconstruction protocol.

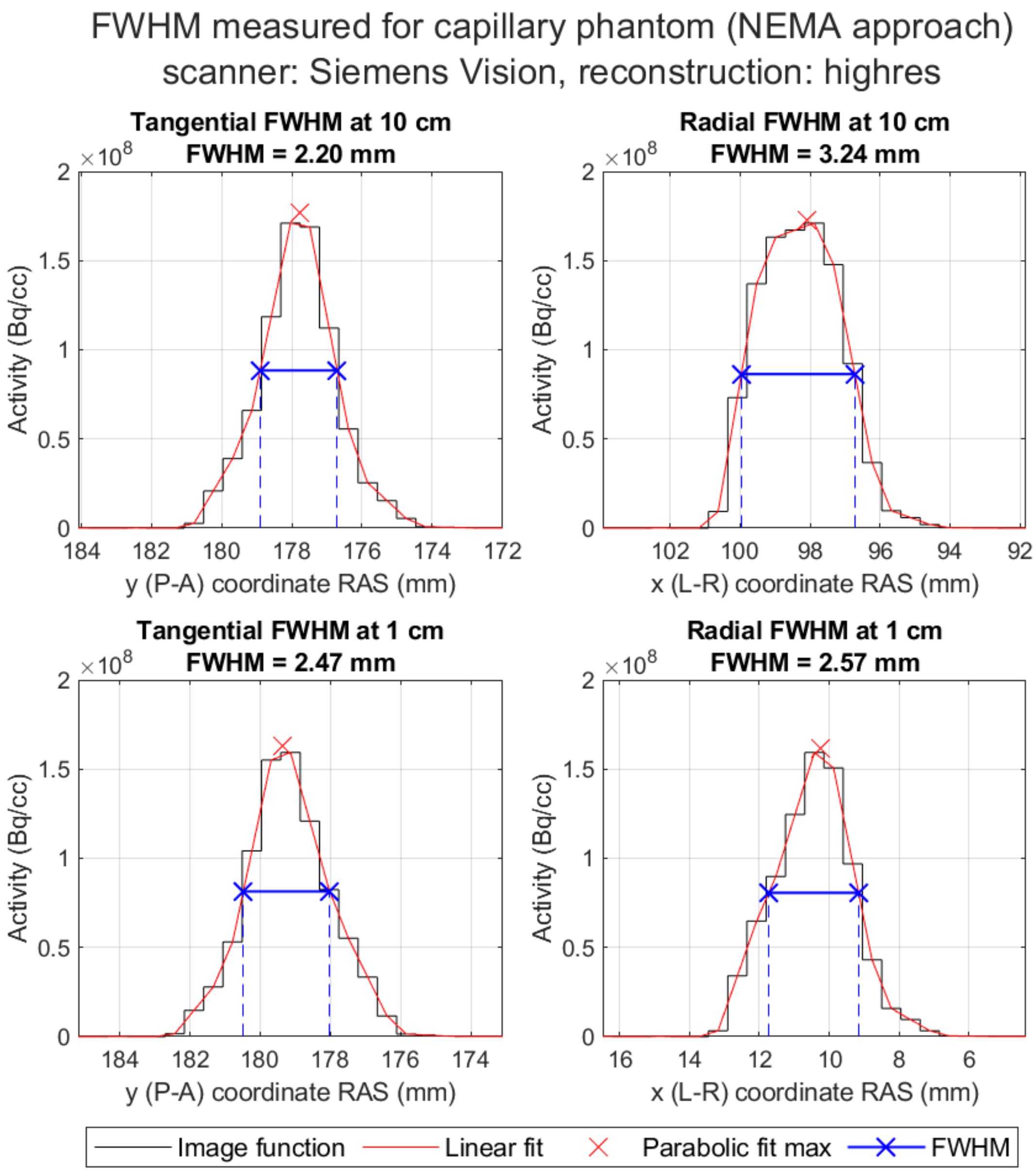

**Figure A.3:** Reference FWHM measured on the Siemens Biograph Vision scanner under "highres" reconstruction protocol.

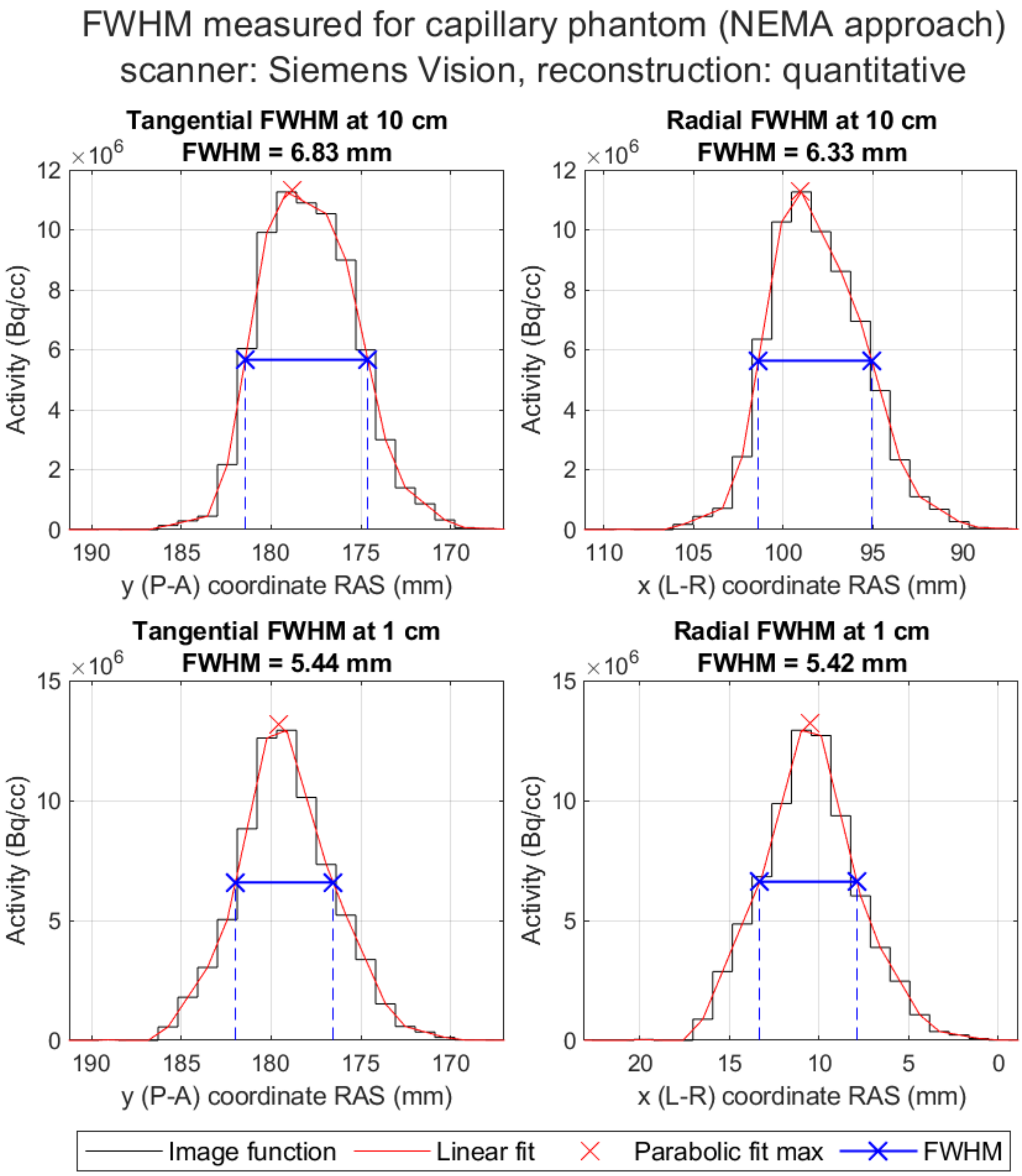

**Figure A.4:** Reference FWHM measured on the Siemens Biograph Vision scanner under "quantitative" reconstruction protocol.